5-2016

In Vitro Multi Scale Models to Study the Early Stage Circulations for Single Ventricle Heart Diseases Palliations

Jian Zhou
Clemson University, jzhou2@g.clemson.edu

IN VITRO MULTI SCALE MODELS TO STUDY THE EARLY STAGE CIRCULATIONS FOR SINGLE VENTRICLE HEART DISEASES PALLIATIONS

A Dissertation
Presented to
the Graduate School of
Clemson University

In Partial Fulfillment
of the Requirements for the Degree
Doctor of Philosophy
Mechanical Engineering

---

by
Jian Zhou
May 2016

Accepted by:
Dr. Richard Figliola, Committee Chair
Dr. Donald Beasley
Dr. Chenning Tong
Dr. Ethan Kung

ABSTRACT

Single ventricle physiology can result from various congenital heart defects in which the patient has only one functional ventricle. Hypoplastic left heart syndrome refers to patients born with an underdeveloped left ventricle. A three stage palliation strategy is applied over the first several years of life to establish a viable circulation path using the one functioning ventricle. Results of the first stage Norwood procedure on neonates with hypoplastic left heart syndrome are unsatisfactory with high morbidities and mortalities primarily due to high ventricle load and other complications. An early second stage Bidirectional Glenn (BDG) procedure is not a suitable option for neonates due to their high pulmonary vascular resistance (PVR), which limits pulmonary blood flow. Realistic experimental models of these circulations are not well established and would be useful for studying the physiological response to surgical decisions on the distribution of flows to the various territories, so as to predict clinical hemodynamics and guide clinical planning. These would serve well to study novel intervention strategies and the effects of known complications at the local and systems-level. This study proved the hypothesis that it is possible to model accurately the first and second stage palliation circulations using multi-scale *in vitro* circulation models and to use these models to test novel surgical strategies while including the effects of possible complications.

A multi-scale mock circulatory system (MCS), which couples a lumped parameter network model (LPN) of the neonatal circulation with an anatomically accurate three-dimensional model of the surgical anastomosis site, was built to simulate the hemodynamic performance of both the Stage 1 and Stage 2 circulations. A pediatric

ventricular assist device was used as the single ventricle and a respiration model was applied to the Stage 2 circulation system. Resulting parameters measured were pressure and flow rates within the various territories, and systemic oxygen delivery (OD) were calculated.

The Stage 1 and Stage 2 systems were validated by direct comparisons of time-based and mean pressures and flow rates between the experimental measurements, available clinical recordings and/or CFD simulations. Regression and correlation analyses and unpaired t-tests showed that there was excellent agreement between the clinical and experimental time-based results as measured throughout the circulations ($0.60 < R^2 < 0.99$; $p > 0.05$, $\sigma < 5\%$).

A novel, potentially alternative surgical strategy for the initial palliation, was proposed and was tested, called the assisted bidirectional Glenn (ABG) procedure. The approach taps the higher potential energy of the systemic circulation through a systemic to caval shunt with nozzle to increase pulmonary blood flow and oxygen delivery within a superior cavopulmonary connection. Experimental model was validated against a numerical model ($0.65 < R^2 < 0.97$; $p > 0.05$). The tested results demonstrated the ABG had two main advantages over the Norwood circulation. First, the flow through the ABG shunt is a fraction of the pulmonary flow, reducing the volume overload on the single ventricle and improving systemic and coronary perfusion. Second, the ABG should provide a more stable source of pulmonary flow, which should reduce thrombotic risk or intimal thickening over an mBT shunt.

A study to examine the ejector pump effect was conducted. Two parameters were investigated: (1) the superior vena cava (SVC) and pulmonary artery (PA) pressure difference; and (2) the SVC and PA pressure difference relative to PA flow rate. Results validated the hypothesis that an ejector pump advantage can be adopted in a superior cavo-pulmonary circulation, where the low-energy pulmonary blood flow can be assisted by an additional source of high energy flow from the systemic circulation. But the ejector pump effect produced by the current nozzle designs was not strong.

Parametric study includes nozzle size, placement, and nozzle shape was conducted. Results shown that nozzle to shunt diameter ratio β had the most important effects on the ABG performance. As β increased, pulmonary artery flow rate and systemic oxygen delivery increased. A suggested β value falls between 0.48 and 0.72. The study showed that a bigger β produced a smaller resistance value. The shape of the nozzle did not change the resistance value. The effects of shunt angle, nozzle placement and nozzle shape on the ABG circulation were not statistical significant.

The aortic coarctation study showed that the aortic coarctation could have an effect on the ABG circulation. The coarctation index (CoI) around 0.5 was found to be the transition point between no effects (CoI > 0.5) and discernible effects on the ABG circulation. These effects include changes in pulmonary to systemic flow distribution.

In summary, this research verified and validated an *in vitro* mock circulatory system (MCS) for Stage 1 and Stage 2 circulations. The system was used to assess a novel conceptual surgery option named the ABG. Parametric studies were conducted to give guidance on designing the important element for the ABG: the shunt (nozzle)

connecting the SVC and systemic circulation. The performance of the ABG under one unhealthy condition, namely, aortic coarctation was assessed.

ACKNOWLEDGEMENTS

I must acknowledge the Leducq foundation for supporting me during my dissertation research. I would like to also acknowledge the financial support of the Grading Assistant (GA) program in the Department of Mechanical Engineering at Clemson University.

I would like to express my sincere appreciation to my dissertation committee members: Dr. Richard Figliola, Dr. Chenning Tong, Dr. Donald Beasley and Dr. Ethan Kung. Thanks for their suggestions and guidance during my research and study.

I would especially acknowledge my research and life advisor Dr. Figliola. The offer letter with his signature 5 years ago opened my door to pursuing the "American Dream". His rigorous attitude towards research and erudition of solving technical problems demonstrate what an 'academic master' looks like. His famous 'so what' will always haunt in my ears reminding me to think deeper before taking actions. His sense of humor and easy going personality makes a united, harmonious research group possible. His wide roam on history, sports, economics, education and etc makes you have no reason to stop learning.

I would like to acknowledge my group members, especially for Dr. Timothy Conover. He is the 'reference book' not only for my research, but also for my path to knowing American culture. I would never forget the friendship built with my colleagues' families. The beautiful time spent with Mr. Ross Gorman and Mr. William Becker's family at Thanksgiving Day or Christmas Day almost every year makes me feel I have a

family in USA. Thanks Dr. Chad Smith and Lauren Carter for reading my proposal and dissertation.

I would like to express my gratitude to my cooperative group: Cardiovascular Biomechanics Computation Lab at Stanford University. It was a happy experience to work with Dr. Alison L. Marsden and Dr. Mahdi Esmaily Moghadam. I am impressed by this productive group with huge achievements in the computational cardiovascular field.

I would also like to acknowledge staff members of Mechanical Engineering department, travel/purchasing staff Ms. Gwen Dockins, workshop staff members Mr. Michael Justice, Mr. Stephen Bass, and Mr. Jamie Cole for their assistance.

I would like to thank my dear family for standing by me since I was born. This was a common and poor family in a small country of south China. More than 90% of the children at my hometown of my age did not have the chance to go to universities, let alone top universities in China. But my hardworking parents, with an average 200$ monthly income, cultivated two students graduated from the top 10 universities in China. And both of us pursued graduate study in USA after undergraduate graduation. My parents do not understand too much about high technologies, including my research. But they supported for every decision I made. My older sister, the first one of my hometown to study abroad, always listens to me and gives suggestions in need.

Finally, I would like to thank my dear girlfriend, Miss. Qi Zheng, for her accompanying, understanding, encouragement and support. Her calmness facing difficulties, optimism towards future, and merit of pursing dreams are good examples for me to learn.

Four and a half year in Clemson is a precious experience for me. I met people with different background. I broadened my eyesight by working with the world advanced Leducq Transatlantic Network Modeling of Congenital Heart Alliance (MOCHA) group. I got to know better about myself, including inner desire, weaknesses and advantages. Everything is so good here. But I have to start my next journey. ‘Life is like a box of chocolates, you never know what you are gonna to get.’ I look forward to my next box of chocolates.

TABLE OF CONTENTS

Page

Table of Contents (Continued)

Page

Table of Contents (Continued) Page

LIST OF FIGURES

Figure Page

List of Figures (Continued)

Figure Page

List of Figures (Continued)

Figure Page

List of Figures (Continued)

Figure Page

List of Figures (Continued)

Figure Page

List of Figures (Continued)

Figure Page

LIST OF TABLES

Table Page

NOMENCLATURE

Variables and Parameters

3D	Three Dimensional
AA	Aortic Arch
AAO	Aortic Arch Obstruction
ABG	Assisted Bidirectional Glenn
AO	Aorta
AR	Amplitude of Respiration
BA	Brachiocephalic Artery
BCPA	Bidirectional Cava-Pulmonary Anostomosis
BDG	Bidirectional Glenn
BSA	Body Surface Area
CA	Coronary Arteries
CFD	Computational Fluid Dynamics
CI	Coarctation Index
CO	Cardiac Output
CS	Central Shunt
CT	Computed Tomography
DTF	Diastolic Time Fraction
HB	Heart Beat
HLHS	Hypoplastic Left Heart Syndrome
IVC	Inferior Vena Cava

LB	Lower body
LPA	Left Pulmonary Artery
LPM	Liter Per Minute
LPN	Lumped Parameter Network
mBT	Modified Blalock Taussig
MCS	Mock Circulatory System
MR	Magnetic Resonance
NSE	Navier-Stokes Equation
OD	Oxygen Delivery
PA	Pulmonary Artery
PIV	Particle Image Velocimetry
PVR	Pulmonary Vascular Resistance
R	Resistance
RCCA	Right Common Carotid Artery
RPA	Right Pulmonary Artery
RV	Right Ventricle
RV-PA	Right Ventricle-Pulmonary Artery
SP	Systemic-pulmonary
SV	Single Ventricle
SVC	Superior Vena Cava
TCPC	Total Cava Pulmonary Connection
TV	Tricuspid Valve

UB	Upper body
VAD	Ventricular Assisted Device

Single alphabet

A	Cross Sectional Area
C	Compliance
c	Oxygen Concentration
g	Gravity Constant
L	Inertance Value
l	Length of Tube
N	Number of Capillary Glass
r	Lower Body to Total Oxygen Consumption Ratio
r	Inner Radius of Capillary Glass
R^2	Coefficient of Determination
V	Oxygen Consumption

Greek Letters

μ	Dynamic Viscosity of Fluid
$\forall$	Volume
ρ	Density of Fluid
β	Nozzle-to-Shunt Hydraulic Diameter Ratio
θ	Shunt-SVC Angle
σ	Root mean square (r.m.s) error

CHAPTER ONE

INTRODUCTION

Hypoplastic Left Heart Syndrome

Background of HLHS

Hypoplastic left heart syndrome (HLHS) refers to a congenital heart condition in which the left ventricle is underdeveloped and unable to perform its function. It was initially termed hypoplasia of the aortic tract complex by Lev in 1952 [1]. HLHS is reported to occur in about 4 of every 10,000 live births [1]. The main syndrome of HLHS patients includes a not fully developed left ventricle, aorta, and aortic arch, as well as mitral atresia or stenosis. The physiology structure is depicted in Figure 1.1. The left ventricle is unable to support the systemic circulation [2] and the remaining single functioning ventricle must become the work pump for both the systemic circulation and pulmonary circulation. At birth, a patent ductus arteriosus is often the only pathway through which blood can reach the body from the heart. Over the first days of life, the ductus arteriosus normally closes and the blood supply to the body diminishes. This single ventricle condition is universally fatal without intervention.

Currently, there are two options for treating HLHS: primary cardiac transplantation or a series of staged palliations using a single ventricle strategy [3, 4]. The surgical choice is dependent on the preference of the institution and its experience [3] and a patient's physiological status. The transplant option is highly limited by the few newborn organs available, the need for continued anti-rejection therapy, and the limited lifespan of the transplanted organ. The more common functional single ventricular

palliation strategy typically consists of three stages of operations. The first stage (Stage 1) of palliation, referred to as the Norwood operation, is performed shortly after birth. The second stage (Stage 2), either a bidirectional Glenn operation or a hemi-Fontan operation, is usually undertaken at 6 to 8 months of age. The third stage (Stage 3) is the Fontan operation, which is usually performed between the ages of 18 months and 4 years. The three stages collectively are referred to as the Fontan conversion.

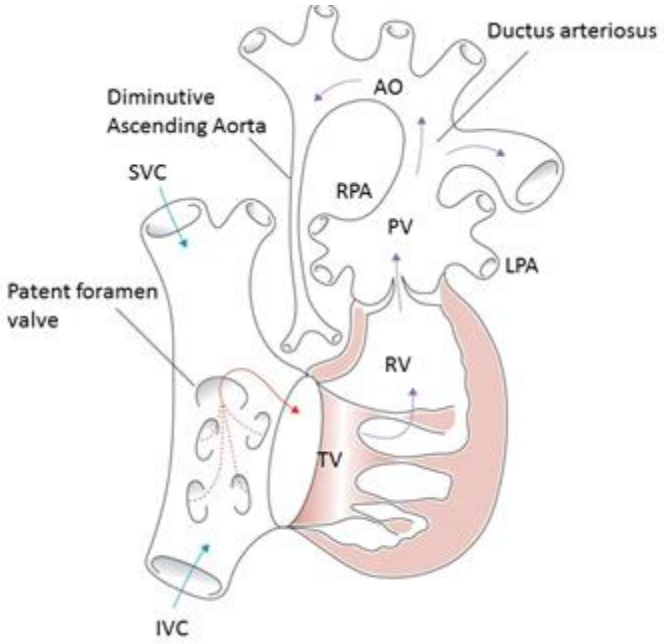

Figure 1.1: Schematic of HLHS physiology. Blue arrows represent systemic venous (deoxygenated) blood, the red arrow oxygenated blood returning from the lungs, and purple arrows mixed blood. Ao, aorta; IVC, inferior vena cava; LPA, left pulmonary artery; PV, pulmonary valve; RPA, right pulmonary artery; RV, right ventricle; SVC, superior vena cava; TV, tricuspid valve[2].

Early Treatment Options for HLHS

Surgical Stage 1 Procedures

The Norwood operation is named after William Norwood who first proposed the surgery option in 1980 [5]. The goals of the Norwood operation include (1) to provide unobstructed systemic blood flow through a reconstructed neoaortic arch; (2) to control pulmonary blood flow with a shunt so that the pulmonary arterial bed will develop normally; and (3) to reproduce communication between the atria by a complete atrial septectomy [6, 7]. The first shunt, named the classic Blalock Taussig (BT) shunt, was introduced by Blalock and Taussig in 1945 for patients with tetralogy of Fallot [8]. The classic BT shunt is a direct connection between the transected subclavian artery or the innominate artery and the pulmonary artery. It does not require the use of prosthetic material but requires the sacrifice of the subclavian or innominate artery [9]. The main disadvantages of BT shunts include long operative dissection time, phrenic nerve injury, technical difficulties during takedown and possible arm ischaemia [10]. Based on the understanding of BT shunt, a modified BT shunt (mBTS) is a man-made graft inserted between the subclavian or innominate artery and pulmonary arteries (Figure 1.2, left figure). The mBTS circulation is characterized by high pulse pressure and diastolic runoff. Coronary flow is produced mainly during diastole and diastolic runoff to the shunt reduces coronary circulation perfusion. This ‘coronary steal’ can result in myocardial ischemia and circulatory instability, which may lead to deaths for Norwood patients [11]. The man-made shunt is prone to thrombosis, a life-threatening situation.

There are surgical alternatives to the mBTS. One surgical variation consists of inserting a conduit between the right ventricle and a pulmonary artery and known as the

Sano shunt or ‘right ventricle-pulmonary artery shunt (RVPA)’ as proposed by Sano and colleagues [7]. Figure 1.2 illustrates the two most common used types of Norwood procedures. The left figure shows an mBTS connected to the aorta (AO) and pulmonary artery (PA), while the right figure shows a Sano shunt. Other available Stage 1 surgery options include a Central Shunt (CS, which is a shunt between the ascending aorta and main pulmonary artery), Waterston and Potts shunt and a hybrid Norwood surgery [12].

Studies found that hemodynamic performances of different surgery options were different. Lagana and colleagues did a comparison study of coronary and pulmonary blood flow between mBTS and CS based Norwood circulations using a multi-scale CFD model [13]. The results demonstrated that CS had higher cardiac output (CO) and shunt flow rate. Also, the CS favored fusion to the right lung while the mBTS favored the left lung. Migliavacca et al. compared multi-scale computational simulation results and clinical data of Norwood operation (CS and mBTS based) and Sano operation to validate the functionality of a multi-scale method [14] and found that the Sano shunt based circulation would produce the minimum back flow in the shunt. Bove et al. applied the same model and investigated how the Norwood circulation reacted to the mBTS and the Sano shunts[15]. The results demonstrated that the key advantage of the Sano shunt compared with mBTS was that the Sano shunt could reduce the diastolic run-off of the systemic circulation and was able to achieve greater hemodynamic stability. The main disadvantage of the Sano shunt was that it required a ventriculotomy, a medical procedure in which a portion of a patient's one healthy ventricle was resected. This could introduce negative effects on right ventricular function, arrhythmias or aneurysm

formation related to the ventriculotomy. Other disadvantages included extra volume load produced by regurgitation from the nonvalved Sano shunt, impairment growth of the pulmonary artery and demand for an earlier Stage 2 palliation [16]. Hsia et al. developed a mathematical model to explore the advantages of a hybrid Stage 1 surgery, which combined bilateral pulmonary artery banding with arterial duct stenting, compared with Norwood surgery with an mBTS or a right Sano shunt. The simulation showed that a hybrid Stage 1 palliation might provide lower systemic and cerebral oxygen deliveries [17]. Other advantages of this hybrid Stage 1 surgery included postponing the complicated reconstruction to an older age when patient is stronger and more tolerant to the operative insults, such as circulatory arrest [18].

For all the Stage 1 palliation options, the shunt must be sized both to regulate the amount of pulmonary to systemic blood flow and to reduce pressure between circulations. Several questions should be answered for the shunt design.

First, what is the relationship between the shunt flow and shunt pressure. Migliavacca et al. investigated the shunt flow and pressure relationship using a finite element method under pulsatile and steady conditions [13]. The relationship could be used to help design the shunt inserted. The same model was used to explore the technique of extracting shunt flow rate from Doppler measurements [19]. In 2001, Pennati et al. evaluated how the anastomotic distensibility and restrictions due to suture presence affect the shunt pressure-flow relationship of the anastomoses using a steady flow *in vitro* circuit [20]. An early *in vitro* study involved the determination of the relationship

between Doppler-based pressure gradient and directly measured pressure gradient in the mBTS by Tacy and colleagues [21].

Second, what is the best design of the shunt, including the shunt diameter and the shunt angle. Difficulties in sizing the shunt to achieve an acceptable Qp/Qs (pulmonary flow to systemic flow) balance and the lack of growth potential leading to changes in the physiological balance with time, and risk of thrombosis with catastrophic consequences all must be considered. Song and colleagues found the 5-mm shunt produced the least energy loss, but higher wall shear stress compared with 4-mm and 3-mm shunts [22]. Sant'Anna and colleagues computed shunt diameter and anastomosis angle effect on a Norwood circulation using patient specific shunts [23] and found that the shunt diameter played the most important role and an angle between 60 to 90 degrees yield a favorable pulmonary blood flow distribution. Waniewski et al. investigated how shear stress and wall shear stress on the inserted shunt effect on graft clotting and pulmonary stenosis formation using a computational fluid model [24]. Kitagawa and the colleagues conducted hydrodynamic experiments (*in vitro*) to optimize the size and the construction of a SP arterial shunt to get suitable pulmonary flow in the Norwood circulation [25]. He suggested the suitable diameter of the shunt lie between 3.0 to 3.5 mm. In 2001, Migliavacca et al. developed an LPN mathematical model of the Norwood circulation to study how the global hemodynamic properties respond to shunt size, vascular resistance and heart rate for Stage 1 circulation [26]. In this shunt performance assessment study, main findings included that a larger shunt size will harvest a greater pulmonary perfusion proportion of the cardiac output. In 2012, Moghadam et al. evaluated the effect of shunt

choice of the Norwood circulation on pulmonary and cerebral perfusion and found that the shunt size and position could both influence the systemic and coronary oxygen deliveries [27].

Third, what is the best ratio of Qp/Qs for the Norwood circulation. The Qp/Qs is an important parameter to influence the performance of the Norwood circulation. Its value is related to the systemic oxygen delivery (OD). In 1994, Barnea et al. reported the first mathematical model to simulate the Norwood circulation [28] and investigated the relationship between Qp/Qs and the arterial oxygen delivery (OD) for different values of cardiac output (CO) and pulmonary venous oxygen saturation. The main finding of the study was that systemic oxygen value moved initially to a maximum value, then decreased as Qp/Qs ratio increased. The group used the same model to explore the oxygen delivery relationship with systemic arterial and venous oxygen saturation, arteriovenous oxygen difference and Qp/Qs [29]. This study implied that an appropriate Qp/Qs was important. Migliavacca et al. found that a pulmonary to systemic flow ratio close to unity produced better systemic oxygen delivery in all physiological states (vascular resistance and heart rate) and shunts [26]. But the model had several limitations. First, the model was analytical in nature and did not simulate a model of the local fluid dynamics. Second, the heart model applied was a steady state approximation, which could not represent realistic pulsatile heart properties.

In summary, the studies have provided useful information on answering the three questions. But different studies may draw different conclusions. A reliable mock circulatory system to study this complex physiology is in need.

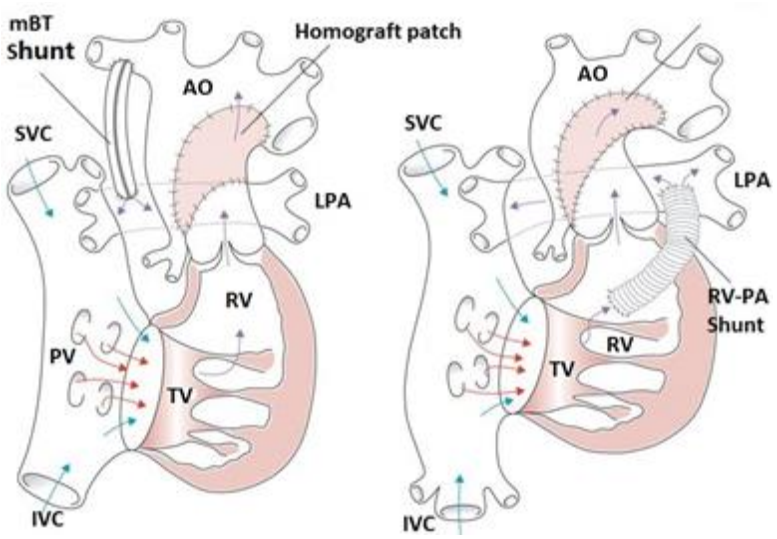

Figure 1.2: The Norwood procedure for HLHS, two types of surgeries based on the way the pulmonary arteries are connected. Left: The classical procedure with a systemic pulmonary artery shunt. Right: Modification of a RV-PA shunt. Ao, aorta; IVC, inferior vena cava; LPA, left pulmonary artery; PV, pulmonary valve; PA, pulmonary artery; RPA, right pulmonary artery; RV, right ventricle; SVC, superior vena cava; TV, tricuspid valve[2].

Due to complexities with this delicate physiology, the heterogenous nature of the patient pool and the challenges with patient management, outcomes following the Norwood procedure remain unsatisfactory with high morbidity and mortality rates. Ventricular work load is high as the healthy single ventricle must simultaneously provide blood flow to the systemic and pulmonary circulations. According to the clinical record, approximately 97% of neonates reached a subsequent state by 18 months after the Norwood operation, consisting of death (37%), cavopulmonary shunt conversion or Stage 2 operation (58%), or some other state (2%, cardiac transplantation, biventricular repair, or conversion by a Stage 3 Fontan operation) [30].

Surgical Stage 2 Procedures

In the Stage 2 operation, as shown in Figure 1.3, the previously implanted shunt in Stage 1 is removed and the superior vena cava (SVC) is connected to the pulmonary artery. The Stage 2 surgery is a transitional procedure in multistage palliation of HLHS. The fundamental purpose of Stage 2 surgery is to relieve the volume load on the single ventricle and provide a controlled source of low-pressure pulmonary blood flow. It may reduce the deleterious sequence of chronic hypoxemia, which shows an abnormally low oxygen in the blood, and long-term ventricular overload, thus yielding a more suitable Fontan candidate [31].

There are two options of Stage 2 operation, the bidirectional Glenn procedure (BDG) and the hemi-Fontan procedure (HFP). In the BDG procedure, the SVC is connected with the undivided pulmonary arteries and the cardiac end of the SVC is closed. BDG is normally straightforward and commonly does not involve augmentation of the central pulmonary arteries. Moreover, it does not offer an established connection for the inferior vena cava (IVC) at the time of the Fontan operation. In the HFP procedure, the central pulmonary arteries are augmented without dividing the SVC. The blood from IVC will not be allowed to flow into pulmonary arteries by means of a temporary intra-atrial patch [32]. The anastomosis part connecting SVC and pulmonary simplifies the subsequent lateral tunnel Fontan surgery by avoiding the need for extra dissection that would otherwise be required to reconnect the right atrium to the pulmonary artery (PA).

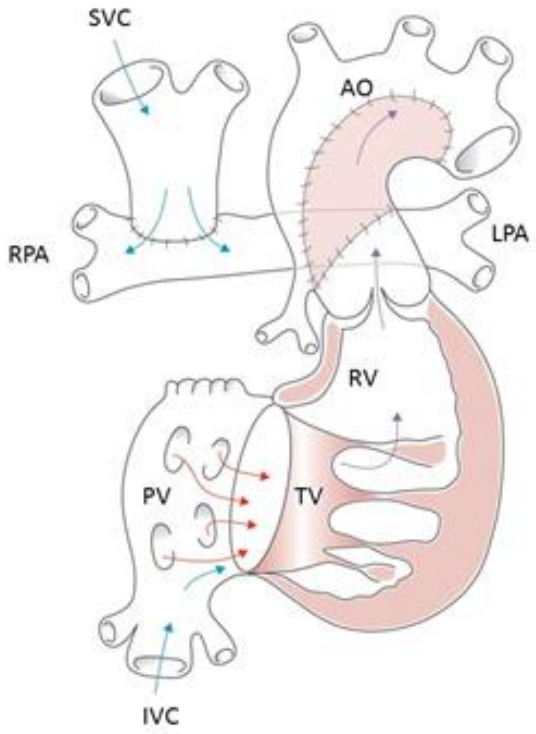

Figure 1.3: Bidirectional Glenn surgery: the cavopulmonary shunt. Ao, aorta; IVC, inferior vena cava; LPA, left pulmonary artery; PV, pulmonary valve; RPA, right pulmonary artery; RV, right ventricle; SVC, superior vena cava; TV, tricuspid valve[2].

In a numerical study, Bove et al. showed that there was no significant hemodynamic differences between the BDG and hemi-Fontan [33]. Troianowski et al. simulated five BDG circulations, each with patient specific 3D BCPA models and boundary conditions derived from direct clinical measurement data. The results demonstrated differences among patients, especially in the 3D flow distributions, strengthening the importance of patient-specific simulations [34]. Kung et al. developed a multi-scale numerical model to simulate a virtual Stage 2 (hemi-Fontan) surgery based on preoperative clinical data and demonstrated that the same surgery performed on different patients can lead to different hemodynamic properties due to physiological differences

[35]. Pekkan et al. used the Particle Image Velocimetry (PIV) technique in an in vitro model to investigate the local hemodynamic differences as compared with CFD results between the hemi-Fontan and Glenn [36]. The study found that the Glenn was hemodynamically more efficient with a lower power loss as compared with hemi-Fontan. The results were contradictive to the conclusions given by Bove et al.[33] and suggested that a more reliable tool was needed to study the complex Stage 2 circulation.

The outcomes of the Stage 2 procedure compared with the Stage 1 procedure are far better. Current results of Stage 2 palliation are satisfactory with mortality rates ranging from 0% to 8% among different institution reports [37, 38]. Median arterial oxygen saturation is also improved from 79% to 84% [38]. But past experiences with neonatal or early Glenn procedures were unsatisfactory. Hence, the current use of Stage 1 procedures. In an initial report of outcomes following the BDG surgery in 537 patients, the highest mortality (over 90%) occurred when the SVC-PA circulation was placed in patients less than one month of age [39]. The main causes of death were primarily due to inadequate pulmonary blood flow and in some cases, SVC syndrome [39], an obstruction of blood flow through the superior vena cava (SVC). Other anecdotal attempts with early BDG surgery have also reported similar unsatisfying outcomes [40-42]. The high pulmonary vascular resistance (PVR) in neonates is the main cause for the unsatisfying results. As its name implies, PVR is a measure of the resistance to blood flow through the pulmonary vasculature and it generally decreases as the infant grows. Pennati et al. developed a mathematical model to investigate how the local bidirectional cava pulmonary anastomosis (BCPA) hemodynamics responding to different PVR values. The

results showed that left pulmonary artery (LPA) and right pulmonary artery (RPA) pressures were sensitive to PVR values [43]. Guadagni et al. used the LPN model coupled with a 3D hemi-Fontan anastomosis model to find that both flow distribution into the lungs and energy dissipation after the hemi-Fontan procedure are only slightly influenced by the pulmonary arteriolar resistance [44]. Appropriate pulmonary artery size and architecture, PVR value, and the function of the atrioventricular valves and systemic ventricle determine whether and when the second stage palliation is feasible. The Stage 2 performance is highly related to the patient's PVR value. In light of clinical experiences, a patient value of PVR indexed to body surface area (BSA) of iPVR < 2 to 3 WU-m2 is considered to be suitable for Stage 2 palliation, where 1 WU = 1 mm Hg/Lpm (Liter per minute). A typical value of iPVR in neonates may be 7.0 to 12.0 WU-m^2 [26].

Aortic Coarctation

Clinical studies demonstrate that a high number of patients after Norwood surgery need reintervention of the neoaorta due to recurrence of an aortic coarctation (CoA) [45]. CoA is defined as the narrowing of the aortic isthmus and HLHS is always related with CoA in juxtaposition with the arterial duct [46]. CoA incidence after the Norwood surgery is between 11% and 37% [47, 48].

Due to the most left-sided obstructive lesions, CoA occurs more in males than in females with a male to female ratio varying from 1.27-1.74 [49]. Machii et al. suggests that CoA in the preductal position in HLHS is caused by the extension of the ductal tissue [50]. Sheikh et al. conclude that: (1) a genetic component of CoA has been found in the

Turner XO syndrome, in which about 35% of patients are affected; (2) the patient-specific aortic morphology also has influence on CoA formation [49]. Surgically excised specimens of aortic coarctation demonstrate cystic medial necrosis of varying degrees with frequent extension beyond the level of the coarctation. A drawing of CoA is shown in Figure 1.4 providing an idea of the position and shape of CoA within the aortic.

Detection and accurate estimation of coarctation severity are of importance to successfully predict long-term outcomes and make suitable treatment options. Clinical techniques currently used include measurement of systolic blood pressure gradient across the coarctation, chest radiography, Doppler echocardiography and catheter angiography [51-53]. These techniques have several limitations and may not provide accurate information of coarctation [54]. Figliola et al. developed an *in vitro* system to assess the accuracy of clinical Doppler predictions of coarctation of variable degrees in the Norwood circulation [55]. The system was also applied to measurements of Giardini and Tacy to study the pressure recovery of CoA to explain Doppler overestimation of invasive pressure gradient across segmental vascular stenosis [81]. They explained that significant segmental stenosis is associated with significant underestimation of the actual pressure gradient due to viscous losses [56]. Keshavarz-Mtamed et al. discussed two flow independent parameters, coarctation Doppler velocity index and coarctation effective orifice area, to describe severity of coarctation [57]. Biglino et al. experimentally validated a computational model of the Norwood circulation with CoA [58]. Itu et al. validated their numerical model by comparing four patient specific multi-scale method

simulation results to *in vivo* measurements. The results showed a mean absolute error of less than 2 mmHg of pressure-drop across the coarctation in the 4 patients [59].

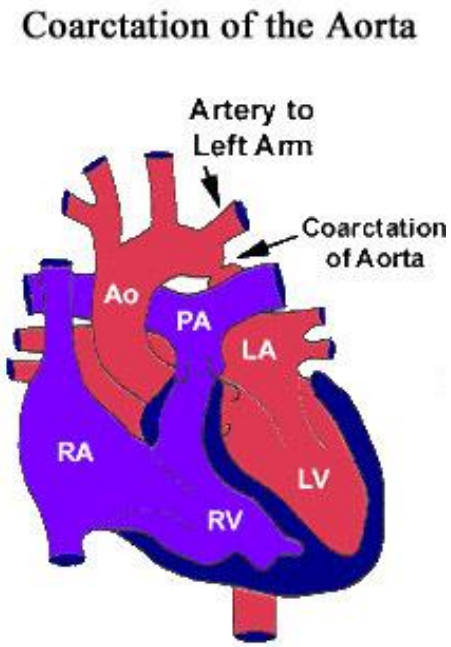

Figure 1.4: Coarctation of the Aorta (Downloaded on 10/15/2015 from http://www.chd-uk.co.uk/)

CoA does not have significant effect on early mortality for Norwood surgery patients [60]. But long-term results demonstrate that CoA is a significant problem after Norwood surgery, despite the modification of the neoaorta by patch augmentation. CoA should be treated seriously, perhaps even for mild coarctation, in order to avoid being developed to high-risk situations but the necessary timing of interventions remains unclear as intervention has its own risks [61]. Using a 3D CFD model, Olivieri et al. revealed that flow in native and surgically repaired aortic arches to correlate respective hemodynamics indices with late morbidity incidence [62]. Wall shear stress (WSS) was found to be located at varying locations in different morphological models. The finding

may transfer a message that varied patterns and locations of WSS in abnormal arch remodeling have an effect on clinical vascular dysfunction.

Severe coarctation can decrease blood flow to the lower body circulation and increase aortic pressure. Menon and collaborators compared in *vivo* (rabbit) test results and numerical results to investigate mechanical contributions to mechanisms of morbidity in CoA and found that CoA could increase diastolic and mean blood pressure [63]. CoA also affects the balance between pulmonary and systemic circulation flow. The main damage brought by CoA is the deterioration of ventricle function. CoA can cause anomalies of other parts, such as: bicuspid aortic valve, tubular hypoplasia, abnormal communication, left ventricle outflow obstruction and positional anomalies [64]. Stenting is an invasive alternative to surgery for coarctation treatment [65]. Concern about this surgery is that the stent-induced aortic stiffness may increase the cardiac workload and blood pressure. But Coogan et al. used a multi-scale model including a patient specific coarctation model to find that coarctation stenting may not affect cardiac work to any significant degree [66]. This might be explained by that the coarctation for this stenting was not strong enough to influence the hemodynamics. It implied that studies, which quantifying the coarctation severity where palpable hemodynamic change happened, were in need.

An understanding of how the Norwood circulation or its alternatives globally and locally respond to the CoA is needed to provide guidance for the appropriate intervention time. Interventional data are difficult to obtain clinically due to the risk to patients. Fortunately, advances in engineering methods are aiding the design of improved in vitro

models to study CoA. For example, rapid prototype technology now can make accurate anatomical reproductions of an altered aortic construction based on clinical imaging data and measurement advances provide the physiological parameters needed for patient-specific studies. Biglino and coworkers built an *in vitro* multi-scale mock circulatory system to reproduce the hemodynamics of post-Norwood surgery and tested patient-specific anatomies aimed at investigating the effect of CoA [67]. The system successfully reproduced physiologic pressures and showed that large pressure drops could be caused by CoA. Arzani and colleagues compared numerical predictions of turbulence intensity with *in vivo* measurement in an CoA [68] and showed reasonable agreement. Other studies have shown the feasibility to investigate CoA effects [69, 70].

In conclusion, current experimental and computational techniques provide reliable and powerful tools to investigate CoA. Information on when interventional treatment is needed for CoA in single ventricle patients.

Modeling Approaches of Cardiovascular Hemodynamics

There are various approaches available in the engineering field to study cardiovascular hemodynamics. Fluid dynamics in large vessels can be represented by non-linear partial differential equations of mass and momentum conservation, such as the Navier-Stokes equations (NSE). Analytical models reduce the Navier-Stokes equations to a form that can be solved analytically for simple cases with boundary conditions properly set [12]. Three-dimensional (3D) computational fluid dynamics (CFD) models solve the NSE numerically and are used to investigate the hemodynamic properties in specific

portions of the cardiovascular system, but it remains impractical to develop a 3D model of the entire circulation. CFD models are limited to the boundary conditions applied to their inflow and outflow surfaces. Traditionally, bio-fluid CFD models impose some flow or pressure waveform at the boundaries of an isolated 3D flow model and solve. Unless some means is provided for the local 3D model to dynamically interact with the rest of the circulation, systems-level response cannot be predicted.

The desire to better understand systems-level circulation behavior lead to the development of zero dimensional (0D) lumped parameter network (LPN) models of the circulation. These provide pressure and flow rate information throughout the circulation (systems-level) but cannot provide local hemodynamics or model accurately surgical particulars. Multi-scale CFD models were later developed to combine the systems-level information of the LPN with the local 3D capabilities of CFD. In multi-scale approaches, 0D LPN models are coupled dynamically to the inflow and outflow boundaries of a 3D CFD model to iteratively provide appropriate time-based boundary condition information.

Lumped Parameter Models Snyder and Rideout [71] gave a comprehensive introduction on how to describe an LPN hydraulic circulation loop. Like an electric circuit, the pressure and flow are analogous to voltage and current, viscous and inertial properties of blood are analogous to resistors and inductors, respectively, and the elasticity of blood vessels are modeled by capacitors. Flow, which is analogous to current, is driven by pressure differences, which are analogous to voltage differences. Time based capacitors and diodes are applied to model heart contraction and unidirectional flow.

These elements translate to a system of ordinary differential equations based on resistance (R), capacitance (C) and inductance (L) as driven by pressure differences. The solution provides the nodal pressures and flows within the whole circuit. LPN is useful to model both the global pulmonary vascular resistance and systemic venous resistance, and the local arteries and veins of the circulation. These models can be tailored to patient specific values using clinical data, when available. The major limitation of an LPN model is that it cannot investigate the local flow dynamics or introduce specific anatomical features. Also, pressure wave propagation effects are lost.

An important part of an LPN models is accurately assigning the elemental (R-C-L) values. Clinical measurements of pressures, flows and velocities lead to assignment of impedance values in each branch. Main measurement techniques include magnetic resonance, cardiac catheterization, and echo-Doppler measurements [72]. Generic population-based values have been arrived at over the years for generalized studies (eg. [73, 74]). Baretta et al. gave several examples on how to use clinical data to calculate LPN parameters [75]. For example, the right pulmonary vascular resistance (PVR) is equal to the measured clinical superior vena cava (SVC) pressure minus the atrium pressure divided by the right pulmonary flow rate.

Because clinical measurements can be invasive, there are many situations in which patient-specific information will be unavailable or information limited. Under this situation, generic values are used wherever clinical information is missing. The effects of patient body surface area (BSA) on the generic LPN elemental values are accounted for by the application of allometric equations as shown in equations 1-1, where LPN

parameters are scaled according to proper powers of the BSA specific for the various vascular comparts or organs [76]

$$x = x_O(\frac{BSA}{BSA_O})^b \qquad (1\text{-}1)$$

Here x and x_O are the vascular and heart parameters (R, C, L) for the patient BSA and for a reference body surface area, BSA_O, respectively. The value x_O corresponds to an adult with BSA of 1.8 m^2, as reported by Snyder and Rideout [77].The exponent b is the 'scaling factor' describing the body surface area effect. The suggested values of b for difference branches are listed by Baretta et al. [75].

Multi-scale Models Formaggia et al. first proposed the approach of coupling a 3D model with an LPN model [78] and Quarteroni and Veneziani conducted a well-posed analysis of this method [60]. Figure 1.5 is an example of a multi-scale model of the Stage 2 circulation [35].The aim of coupling a 3D domain with a 0D model (LPN) is to provide the two sub-domains with accurate boundary conditions. Boundary conditions are essential for properly predicting the hemodynamics inside the targeted investigated system. In particular for patient-specific models, boundary conditions are applied to mimic the valuable available clinical data. In a multiple-inflow/outflow 3D model, the flow distribution is determined solely by the outlet resistance in the branches of the domain if zero or equal pressures are used at all the outlets [79]. In situations such as the Norwood circulation, inlet flows can usually be measured but outlet flows in the pulmonary branches are much more difficult to obtain. Lastly, coupling these kinds of

boundary conditions with a 3D model can be used to predict the global system response for changes in physiological alterations, surgery-based construction, and portions of downstream or upstream of the 3D model. The 0D models cannot provide spatial variables. In contrast, a 0D model coupled with a 3D model can provide the information on local hemodynamics, including spatial and time dependent pressures, flow rates, wall shear stress (WSS) and energy loss. The iterative interaction of the two subsystems is that 3D domain provides the 0D model with flow rates at the interface, while the 0D model imposes pressure boundary conditions at the interfaces of the 3D domain.

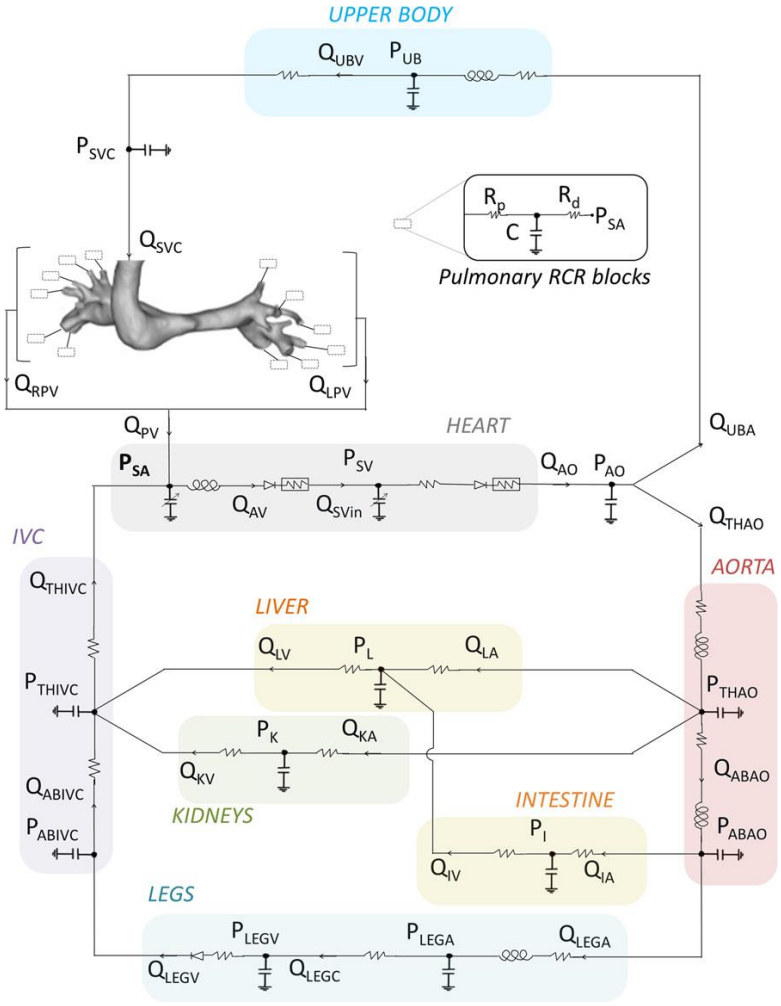

Figure 1.5: Full lumped parameter network model coupled with 3D phantom of Stage 2 [36].

The LPN concept guided the development of *in vitro* mock circulatory systems (MCS) for representing the compliance and resistive properties of the circulation [80]. In a multi-scale in vitro model, a hydraulic analog of the LPN is connected to the inflow/outflow points of a 3D test section to provide appropriate time-dependent boundary conditions.

Compared with a numerical multi-scale model, an *in vitro* multi-scale model is generally contracted to a reduced LPN model having fewer elemental values within each

branch. This is achieved by applying least-squares impedance matching with Thevenin equivalent circuit analysis to the original LPN model. The reasons are that (1) it is practical to adjust only a limited number of physical R-C-L elements, and, (2) the addition of each physical element can add a small artificial inertance beyond the physiological model. For example, a numerical LPN may have over 50 adjustable elements and the experimental model may reduce this to fewer than half or less, usually by combining proximate resistors and capacitors into equivalent values. The reduced number of elements does limit higher order frequency response of the experimental model. However, the reduced model method has been validated through excellent matches both in terms of mean and time-based pressure and flow rate values between experimental results and clinical data as reported in several single ventricle circulation *in vitro* studies [67, 81, 74, 82, 83].

Respiration Modeling In the Univentricular Circulation As there is no explicit indication that respiration impacts any clinical complications in the Stage 1 and the Stage 2 circulations, previous models of Stage 1 and Stage 2 have ignored respiration and thereby have neglected its effects. However, respiration effects on hemodynamics and clinical outcomes on the Stage 3 circulation have been documented by Hsia et al [84]and Vukicevic et al [82, 74] and a few other studies have modeled respiration effects in the Stage 3 Fontan circulation [85, 86, 84]. The function of the respiration system model was validated against clinical data [74, 82]. The experiments recapitulated the clinical observations that respiration increased antegrade flow towards the heart during

inspiration and decreased the flow during expiration, including the possibility of hepatic venous and IVC flow reversal [74]. The validated respiration modeling approach can be used in a Stage 2 system to impose respiration influences.

Current results imply that respiration has a time-based influence on IVC, hepatic vein (HV) and pulmonary artery flows and pressures within the Stage 3 circulation. Respiration effects on Stage 1 and Stage 2 are not clear but respiration is apparent in some clinical flow and pressure signals.

Concept of the Assisted Bidirectional Glenn (ABG)

The Norwood surgery is associated with high mortality and morbidity due to a number of drawbacks. The new circulation, created by the implanted shunt, may not keep the blood flows to the pulmonary circulation and systemic circulation branches balanced. As discussed earlier, outcomes following the Norwood procedure remain unsatisfactory.

The BDG or hemi-Fontan Stage 2 surgery can provide a more stable source of pulmonary blood flow, reduce ventricular workload, and reduce thrombotic risk with excellent survival rates. However, the Stage 2 palliation is unsuitable for neonates because the high pulmonary resistance of the neonatal circulation limits pulmonary blood flow in this circulation. The major causes of death include inadequate pulmonary blood flow, which is a consequence of the high PVR in neonates.

Under this background, Esmaily-Moghadam et al. and Zhou et al. have discussed a novel initial palliation option called the Assisted Bidirectional Glenn (ABG) [83, 84]. Figure 1.6 illustrates the comparison between the Norwood, the BDG and the ABG

circulations. The ABG circulation is a hybrid of the Norwood circulation and the Glenn circulation. In the ABG, a reasonably designed shunt would be inserted between the systemic circulation and the SVC, which would be connected to the pulmonary artery in the manner of a standard Stage 2 Glenn operation. The pulmonary blood flow would be mainly supplied from SVC but partially supplied from the inserted shunt.

Blood within the systemic arteries has high potential energy because of its high pressure. In the standard Norwood circulation with mBTS, the high systemic pressure drives the pulmonary blood flow but this potential energy is partly dissipated through the shunt, which also acts as a resistive conduit to reduce pressure and flow to the level of the pulmonary circulation. In the ABG, however, a goal is to harvest some of this energy to augment pulmonary flow by using an ejector pump concept.

An ejector pump, as illustrated by the conceptual drawing in Figure 1.7, converts high pressure energy into kinetic energy, such as through a nozzle. This high kinetic energy fluid is then used to do work on a secondary fluid that is at a lower pressure. This augments the flow rate of the secondary fluid. Ideally the energy of the high-pressure fluid is not wasted, but imparted to the secondary flow, as the kinetic energy diffuses within the secondary fluid converting back to pressure. In concept, the systemic circulation would serve as the high pressure source and would communicate with the secondary, lower pressure SVC flow through a systemic-to-caval shunt. The momentum of the jet would assist the caval flow to the pulmonary artery while it diffuses within the SVC reverting back to pressure to drive pulmonary blood flow.

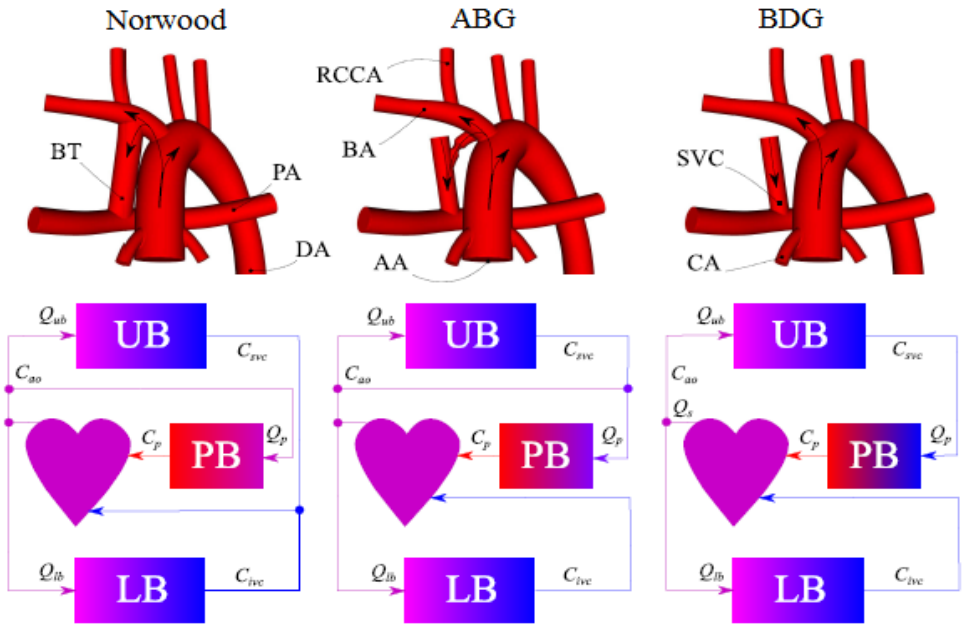

Figure 1.6 : Models illustration for mBTS (left), assisted bidirectional Glenn (middle), and BDG (right). AA, aortic arch including ascending aorta; DA, descending aorta ;CA, coronary arteries; PA, pulmonary arteries; SVC, superior vena-cava; BT, Blalock-Taussig shunt; ; BA, brachiocephalic artery ; RCCA, right common carotid artery. Qp, Qs, Qlb, and Qub denote pulmonary, systemic, lower body, and upper body flow rates. Cs, Cp, Cao denote systemic vein, pulmonary vein, and aortic saturations [84].

In the initial ABG concept [84], a ligaclip (surgical clip) was envisioned as being applied over the exterior of the shunt, near its junction to the SVC, narrowing the shunt and serving as the nozzle to convert high systemic pressure into kinetic energy. In concepts, the increased velocity after the nozzle is directed into the SVC where it adds momentum. This kinetic energy should be recovered as an increased pressure within the distal section of the SVC, which acts as the diffuser. In the ABG circulation, the ejector-shunt is intended to increase pulmonary blood flow while maintaining or reducing the pressure gradient between the SVC and the pulmonary arteries.

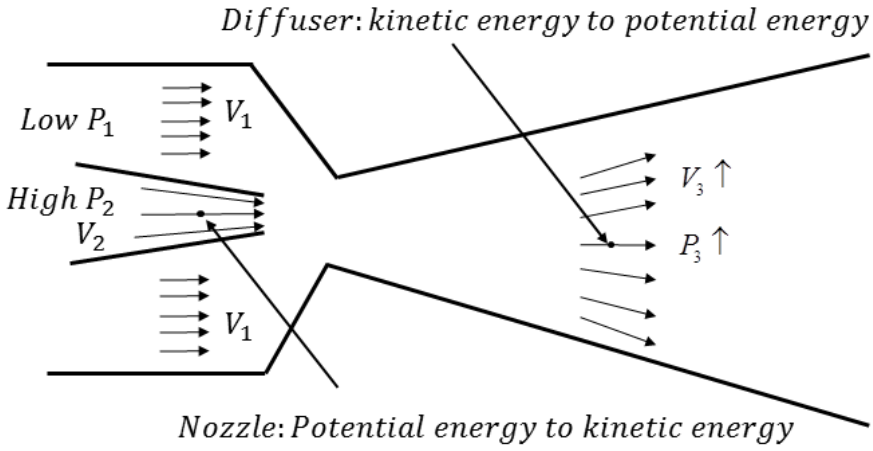

Figure 1.7: Schematic of an ejector pump.

A goal of the ABG is to improve pulmonary blood flow and to do so without a large increase in SVC pressure. If successful, the ABG procedure would reduce the number of surgeries in the palliation strategy from 3 to 2. Later as the patient grows with concomitant reduction in PVR, the shunt could be occluded via a catheter to revert the ABG to a standard BDG. However, there remain questions about whether the concept can be successfully implemented and if so, how the nozzle should be designed, sized, and placed. Without the ejector effect, the ABG concept refers a resistive shunt pathway between the systemic circulation and the SVC.

Research Aims

This study tested the hypotheses that (1) it is possible to model the first and second stage palliation circulations using multi-scale *in vitro* circulation models, and to use these models to test novel surgical strategies, and if so, (2) test whether an ejector

pump advantage can be adopted in a superior cavo-pulmonary circulation, where the low-energy pulmonary blood flow can be assisted by an additional source of high energy flow from the systemic circulation.

The specific aims of this study are:

Aim 1: Construct multi-scale models for Stage 1 circulation and Stage 2 circulation based on patient specific parameters obtained from clinical measurements. The function of these *in vitro* models will be verified and validated as an aid to surgical planning, predict clinical hemodynamics, and guide patient management. Discrepancies between the clinical measurements and experimental acquirement will be used to improve and modify the *in vitro* models.

Aim 2: Use the validated Stage 1 and Stage 2 system to examine a conceptual novel surgery, called the assisted bidirectional Glenn procedure (ABG). Compare the performance of the ABG circulation to the performance of the Norwood circulation and the BDG circulation. Determine if an ejector pump effect can be developed within the proposed circulation.

Aim 3: Assess the performance of the ABG circulation under parametric variations, e.g. varying shunts and nozzles having different shapes, sizes, and position and under adverse physical conditions, such as aortic coarctation and high pulmonary vascular resistance (PVR).

Aim 4: Investigate respiration effects within the Stage 2 circulation as a means to better recapitulate time-based clinical measurements. Determine if there is an effect on the overall hemodynamics.

The following chapter will present the *in vitro* multi-scale models of Stage 1 and Stage 2 circulations. Numerical or clinical data will be used to validate the functionality of the models. In Chapter 3, a hybrid of validated Stage 1 and Stage 2 MCS will be presented to study the ABG circulation. In Chapter 4, parametric studies on SVC-to-aorta shunt will be conducted. In Chapter 5, aortic coarctation effects on the ABG will be investigated. In Chapter 6, the effects of respiration on Stage 2 circulation will be studied and discussed. In Chapter 7, a summary of main conclusions and limitations of this research will be discussed.

CHAPTER TWO

MULTI-SCALE IN VITRO MODELS

This chapter details the *in vitro* Norwood circulation and Stage 2 Glenn circulation mock circulatory system models. Because the two models use similar components in their respective compositions, the elemental components are described together.

Methods

Mock Circulatory System

The mock circulatory system (MCS) of the Norwood circulation is based on the multi-scale concept. A detailed multi-compartment LPN of the Norwood circulation was described by Esmaily-Moghadam et al. [84], and adopted as the reference to design this MCS. In order to design a practical MCS, obtaining sufficient dynamic accuracy with a minimal number of components, a reduced LPN of the Norwood circulation was derived from the full model by applying least-squares impedance matching with Thevenin equivalent circuit analysis. One example of the method to reduce the SVC branch is given in Appendix A.

The reduced LPN model of the Norwood circulation is coupled with an appropriate three-dimensional (3D) model of the aorta, pulmonary artery, and anastomosis sites, as shown in the schematic of Figure 2.1 and the photograph of Figure 2.3. It contains upper body (ub), lower body (lb), and pulmonary circulation branches. The pulmonary and upper body branches each included proximal (p) and distal (d) resistance elements (R), a compliance element (C), and the inertance of the vascular

tubing (L), known as a 4-element windkessel [85, 86]. One resistance element is used to control flow rate in the lower body. The appropriate hydraulic model was connected to its respective 3D model. In the Norwood circulation, a 3.5 mm diameter systemic to pulmonary shunt connected the innominate artery to the RPA.

The circuit was operated between a mean aortic pressure and a mean atrial pressure. A ventricular assist device (VAD) was used to provide the pulsatile aortic pressure. A constant head tank was used to fix the atrial pressure. A saline-glycerin blood analog fluid was used ($1060\,\mathrm{kg}/m^3$, $3.3\times10^{-6}\,m^2/s$ at $22\ ^{o}c$).

The bidirectional Glenn (BDG) circulation MCS, shown in Figure 2.2, is very similar to the Norwood MCS except the test section. The BDG was modeled with a simple SVC to RPA anastomosis.

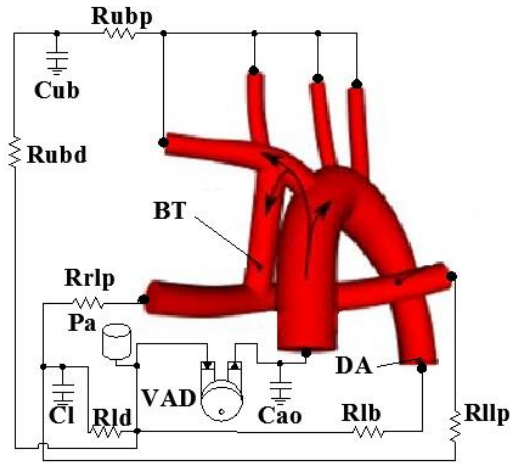

Figure 2.1: The Norwood mock circulatory system lumped parameter network coupled with 3D anastomosis models for the Norwood circulation. C, compliance; ao, aorta; p, lung; up, upper body; R, resistance; lb, lower; ld, lung distal; llp, left lung proximal; rlp, right lung proximal; ubd, upper body distal; ubp, upper body proximal; SVC, superior vena cava

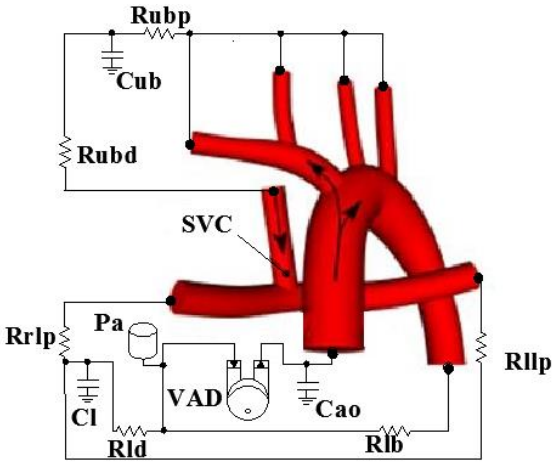

Figure 2.2: The BDG mock circulatory system lumped parameter network coupled with 3D anastomosis models for the BDG circulation. C, compliance; ao, aorta; p, lung; up, upper body; R, resistance; lb, lower; ld, lung distal; llp, left lung proximal; rlp, right lung proximal; ubd, upper body distal; ubp, upper body proximal; SVC, superior vena cava.

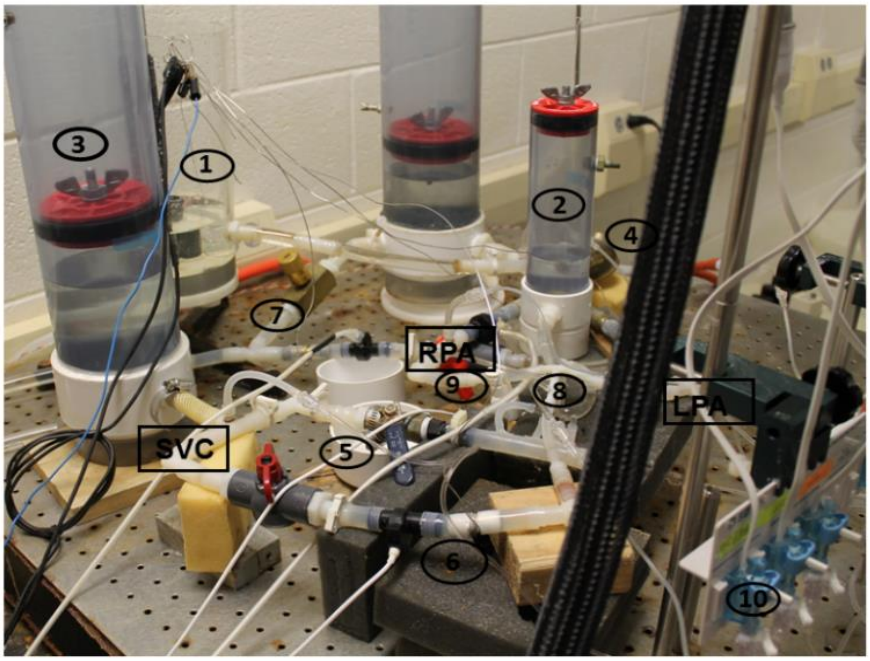

Figure 2.3: Photograph of the MCS: 1, Atrium head tank; 2, Aorta proximal compliance element; 3, SVC compliance element; 4, Berlin Heart VAD; 5, SVC resistance element; 6, flow meter; 7 and 9, RPA and LPA resistance (valve) elements; 8, Test section; 10, pressure transducers. LPA left pulmonary artery; RPA, right pulmonary artery; SVC, superior vena cava.

Ventricular Assist Device and Aortic Pressures

A ventricle assist device (VAD) (Excor®, 25 ml, Berlin Heart, Berlin, Germany) was used to simulate the single ventricle and to achieve a pulsatile ascending aortic pressure. The VAD includes two parts: a liquid filled side and an air filled side, divided by a flexible membrane. The schematic of the system used to operate the VAD is given in Figure 2.4. The VAD was operated pneumatically under computer control by alternating between high pressure applied during systole and venting to vacuum during diastole. Both the high and low pressures were regulated from source values using pressure regulators. The alternating pressure was manipulated using a three-way valve (Model: 225B-111CAAA, MAC Valve, Dundee, MI, USA), which was controlled by an 0-5V DC analog signal provided by a data acquisition computer system (USB-6211 and Labview 8, National Instruments, Austin, Texas). The duration of the high pressure signal over one heartbeat determined the systolic time ratio. The cycling rate of the alternating pressure determined the heart rate. The high pressure and low pressure were tuned to obtain the target mean ascending aorta pressure.

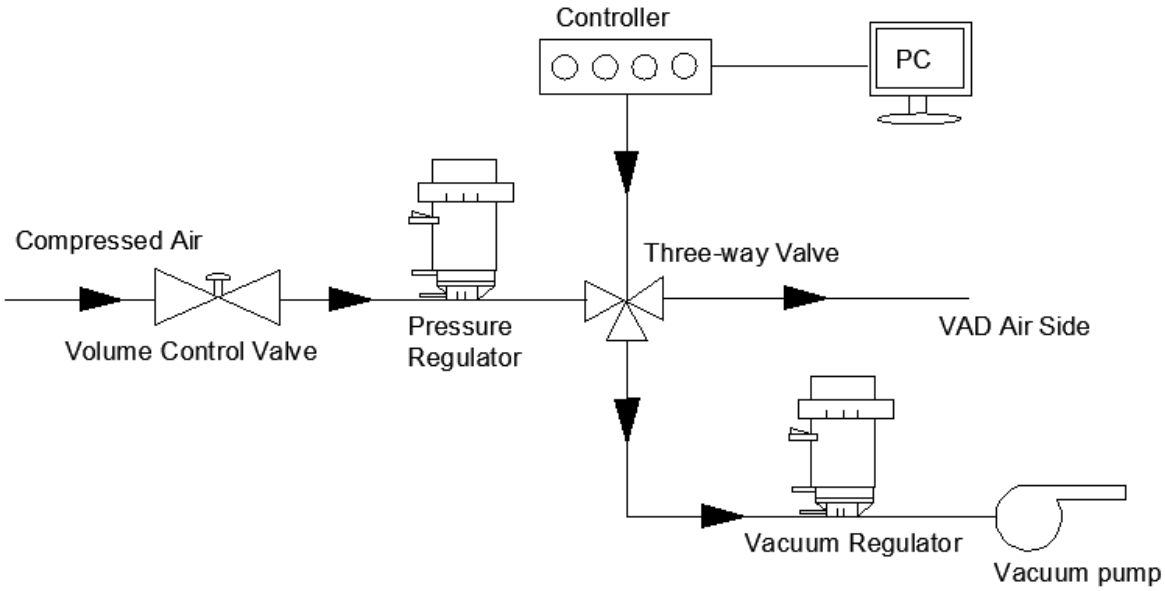

Figure 2.4: Schematic of the VAD driving system. PC, computer; VAD, ventricle assisted device.

Test Sections

Test sections used in the Stage 1 validation were built using anatomical reconstructions of patients from clinical images reported in a formal study of mBTS [27]. In the Stage 2 verification and validation study, patient-specific anatomical details were acquired from real patient clinical imaging as recorded in the Leducq database. In creating the models, the tomographic model was reconstructed from computed tomography (CT) images. A 3D geometric virtual-space model was then built from magnetic resonance image (MR) data volumes by identifying the centerline path along the pulmonary artery from which perpendicular 2-D segmentations of the vessel lumen were created and then merged creating a solid (.stl file) model of the vessel [86]. The solid model was prepared for use as an experiment test section, including adding

extensions for tube fittings. The modifications of the models were done using commercial modeling software (3-Matic®, Materialise, Leuven, Belgium).

The test models used in this study were all created either by high resolution stereolithographic printing either from Watershed 11122® material to a layer resolution of better than 0.05 mm, or by impact jet printing using Verowhite® material (Verowhite®, Stratasys, Minnesota, USA) to a resolution of 0.030 mm - 0.016 mm [67]. Variations of this manufacturing technique have been reported previously [87-90].

Resistance Elements

Flow resistance elements were used to fix the resistance parameters throughout the circuit. Flow resistance is defined as $R = \Delta p^n / Q$, where Δp and Q are the pressure drop and flow rate across the element, respectively [55]. The value of *n* varies from 1 (laminar flow) and ½ (fully turbulent flow). Two main methods were used to achieve specific resistance values, namely, ball valves and laminar resistance elements. Ball valves are convenient for changing the resistance value *in situ*, but this resistance value is not linear with flow rate. Given the low flow rates and the small changes in flow rate used in these circulations and the fact that the resistance was set individually for each test case, nonlinearity was not an issue. A laminar resistance element was created by packing a tube with bundles of capillary tubes. These laminar elements provided a resistance that was linear with flow rate and used where resistance values were small. The residual tubing and connectors also added a resistance to flow. The stated elemental resistance value *R* was determined *in situ* by measuring the pressure drop and mean flow rate

between sections or nodes of each branch of the system under a steady flow condition. The method used to develop laminar resistance element and resistance element calibration is described in Appendix B, and consisted of measuring the pressure drop across an element at a known steady flow rate consistent with the intended position of the element within the MCS.

Compliance Elements

Compliance is used to simulate the elastic volume change of a vessel during pressure variation. The compliance value was determined by $C = \Delta\forall / \Delta p$, where $\Delta\forall$ is the change of volume according to pressure change Δp.

The upper body and aorta compliances were developed by using air chambers (also called "windkessels"), each consisting of a vertical cylinder made of clear polyvinylchloride (PVC), capped at one end and partially filled with water and air, and sealed at the top with a moveable plumber test plug (Oatey Corp, Cleveland, OH). Compliance is obtained by compression of the trapped air as more water enters the chamber from the MCS. The plug is set to trap a desired volume of air, in order to attain the desired compliance value. One of the air chambers is shown in Figure 2.5. Another type of compliance element used elastic tubes to simulate respiratory dynamics in the MCS, and is discussed in Chapter 6. The method used for compliance element calibration is described in Appendix C, and consisted of measuring volume change for an applied pressure change. The elements were found to be essentially linear over the pressure changes occurring within a cardiac or respiration cycle.

Figure 2.5: Photograph of an air chamber compliance element.

Inertance Elements

Inertance refers to the pressure gradient required to accelerate a mass of fluid. Fluid inertance mimics the electrical property of an inductor. The inertance in a fluid system creates a pressure drop while a flow accelerates. The relationship can be described as: $\Delta p = L(dQ/dt)$, where L is the inertance value. The formula for L is: $L = \rho l / A$, in which ρ is the fluid density , l and is the conduit length and A is cross sectional area.

Inertance is real in a physiological system but tends to be small in infants. In order to keep the inertance effect realistic within an *in vitro* system, inertance is controlled by minimizing the tube length between system elements while avoiding smaller diameter tubes, so as to provide for a compact bench system. Excess inertance manifests itself as

accentuating the pressure amplitude and increased time-lag in the time-based signals. Efforts were taken to minimize extraneous inertance in the MCS.

Measurement Systems

Flow rate was measured at various points throughout the MCS, including the lower body branch, SVC, LPA and RPA. Each flow rate was measured by an in-line square wave electromagnetic flow probe with control box (P600 series probe, FM501 Control unit, Carolina Medical Electronics, East Bend, NC). The photographs of the flow meter and flow probe are shown in Figure 2.6 (Upper). Pressures are measured either by catheter or wall tap and by blood pressure transducers (DTX-Plus; BD Medical, Austin, TX) driven by bridge amplifiers (Model 2300, Micromeasurement Group, Raleigh, NC) as shown in Figure 2.6 (Lower). All transducer signals were operated and recorded using a computer-based data acquisition system controlled by Labview.

Figure 2.6: FM501 Electromagnetic flow meter (Upper left) and EP640 flow probe (Upper right); blood pressure transducers (lower left) and bridge amplifiers (lower right).

LPN Parameters

The Stage 1 Norwood circulation MCS used has been validated in previous studies [48, 67]. A verification of the MCS flow and pressure results against those predicted by a numerical model was presented for the Stage 1 MCS verification study. The multi-scale numerical model is described by Esmaily-Moghadam [84] and used a higher order LPN than the experimental model but with identical 3D models.

The elemental LPN component values of Stage 1 were obtained from a prior study that incorporated clinical catheterization and angiographic data from 28 Norwood patients [26]. These values were the same used in the numerical model [84]. For the experimental model, the number of elements in the LPN was reduced using Thevenin

equivalency, as previously described. Values with uncertainty (details in Appendix D) for the impedance elements used in the MCS are given in Table 2.1 for the two cases of indexed PVR tested: 2.3 and 7.0 WU-m^2 [1.0 WU = 1 mm Hg/Liter per minute (LPM)]. This range addresses patient growth from the neonatal (high PVR) to the larger infant size (low PVR) more common at the time of the Glenn surgery.

Table 2.1: Stage 1 study elemental values for experimental lumped parameter network model

Parameters	**Experimental values**	
	Low PVR case	High PVR case
Rlb	**5.48±0.16**	**5.48±0.16**
Rupd	**4.91±0.15**	**4.91±0.15**
Rupp	**0.56±0.02**	**0.56±0.02**
Rrlp	**0.31±0.03**	**0.26±0.03**
Rllp	**0.31±0.03**	**0.27±0.03**
Rld	**0.29±0.02**	**1.02±0.03**
Cao	**0.29±0.03**	**0.29±0.03**
Cup	**0.45±0.05**	**0.45±0.05**
Cl	**0.64±0.03**	**0.64±0.03**

R, Resistance [mmHg.s/ml]; C, Compliance [ml/mm Hg]. Subscripts: lb, Lower body; upd, Upper body distal; upp, Upper body proximal; rlp, Right lung proximal; llp, Left lung proximal; ld, Lung distal; ao, aorta; up, Upper body; l, lung. Set value± uncertainty (95% confidence level)

The LPN elemental values used for the Stage 2 circulation were calculated directly from clinical measurements of catheter pressures and MR flow rates. The specific parametric values with uncertainty used are listed in Table 2.2. One patient case occurs at surgical time point 5, which corresponds to just before the Stage 3 Fontan surgery. In order to maintain confidentiality, the patient is designated here as UM2_TP5 (UM, University of Michigan), where the acronym refers to the patient's clinical center and the numerical value identifies the patient's record.

Table 2.2: LP elemental values for Stage 2 validation study

Parameters	Unit	UM2_TP5
Pao	mmHg	73±0.5
Pat	mmHg	6±0.1
Rlb	mmHg.s/ml	5.01±0.12
Rubd	mmHg.s/ml	3.73±0.09
Rubp	mmHg.s/ml	0.12±0.01
Cup	ml/mmHg	0.45±0.02
Rrlp	mmHg.s/ml	0.13±0.01
Rrld	mmHg.s/ml	0.37±0.02
Crl	ml/mmHg	NA
Rllp	mmHg.s/ml	0.67±0.03
Rlld	mmHg.s/ml	0.22±0.01
Cll	ml/mmHg	NA
Cao	ml/mmHg	0.25±0.02
HB	times/min	84

C, Compliance; LB, Lower body; LL, Left lung; LLD, Left lung distal; LLP, Left Lung Proximal; LP, Lumped parameter; LPN, Lumped parameter network; R, Resistance; RL, Right lung; RLD，Right lung distal; RLP, Right lung proximal; RR, Respiration rate; UP, Upper body; UPD, Upper body distal; UPP, Upper body proximal. TP4, Time point 4, just post Glenn surgery; TP5, Time point 5, pre Fontan surgery. Set value± uncertainty (95% confidence level)

Data Analysis

Time-based experimental signals used in the comparisons were ensemble-averaged over 20 consecutive heartbeats. Pressure and flow rate signals from the numerical and/or experimental models were compared point-to-point at corresponding times using linear regression (y = x) from which a coefficient of determination (R^2 value) was calculated (details in Appendix E). An unpaired Student's *t*-test (details in Appendix F) was used to compare the mean values, such as a numerical or clinical mean value to an experimentally measured mean value. A *p*-value (details in Appendix F) of 0.05 or less was considered to indicate that a statistically significant difference existed between the two tested mean values. A point-by-point root-mean-square error (rms error) was calculated between two time-based signals to compare the experimental measurements with the corresponding numerical or clinical signals. The rms error was normalized by

the mean value, and is reported as σ = rms error/mean (details in Appendix G). A value of 10% or less than was considered to indicate a good fit of the experimental model to the data (clinical data or numerical data in this study).

Results

Verification Results for Stage 1 MCS

The time-based signal comparisons between numerical and experimental Stage 1 Norwood with mBTS models are shown in Fig. 2.7 for both values of PVR. The signals are plotted over a single heartbeat and have been ensemble averaged over 20 continuous heart beats. Both experimental and numerical predictions [84] of pressures within the pulmonary arteries are higher at the higher PVR, as expected, and the pulsatility of the flow rate corresponding to the heart beat cycle is seen. LPA and RPA flows and pressures are well-reproduced between the models ($0.62 < R^2 < 0.74$). The numerical model predictions of flows and pressures show higher frequency content than the experimental model measurements but the mean values compared very well and showed no statistically significant differences ($p > 0.05$) between the two models, verifying the capability of the experimental setup. The numerical signals for RPA and LPA pressures show more pulsatility compared with the experimental model measurements, which was likely a pulmonary compliance mismatch between the two models. The calculated σ was < 5% for both the flow predictions and pressure predictions, demonstrating acceptable comparisons.

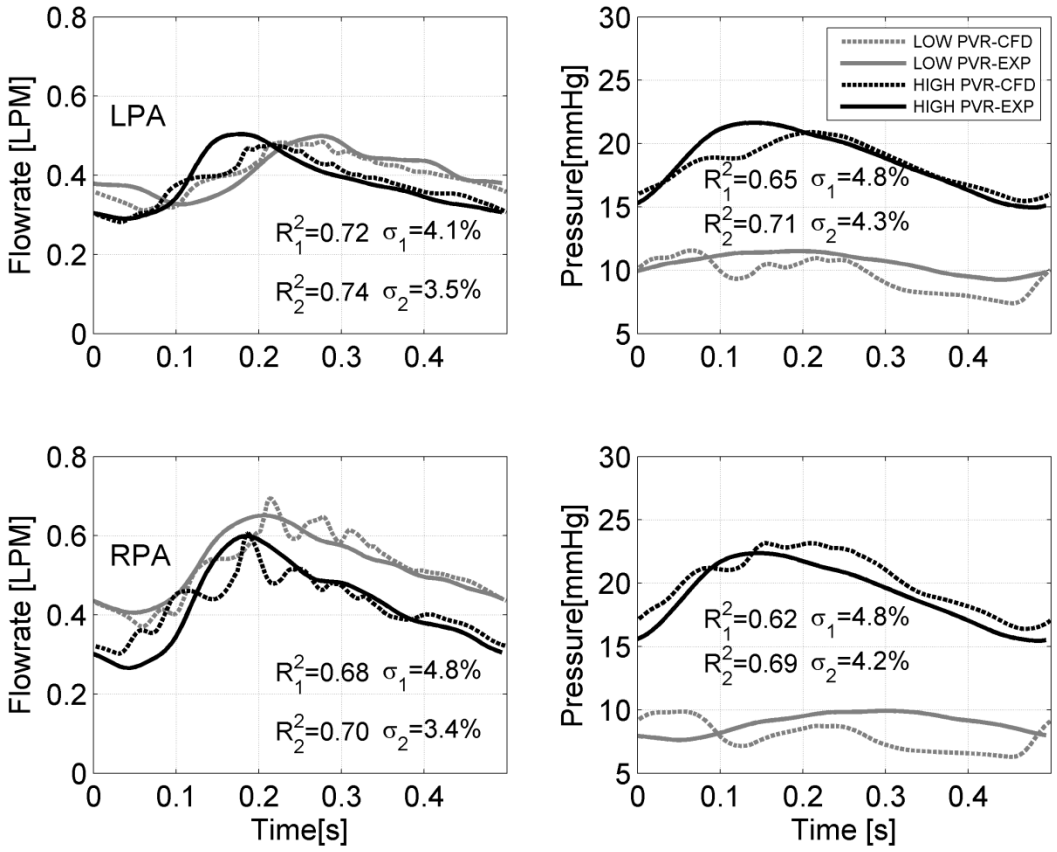

Figure 2.7: Time-based experimental (solid) and numerical (dashed) flow rate and pressure signal comparisons for the mBTS circulation under low and high values of pulmonary vascular resistance (PVR). Subscript: 1, low PVR (2.3 WU-m^2); 2, high PVR (7.0 WU-m^2).

Verification and Validation Results for Stage 2 MCS

In order to test and verify the Stage 2 MCS, a validation test against clinical data was performed. The time-based experimental and clinical ascending aorta pressures are shown in Figure 2.8, respectively for the patient UM2, using TP 5. The ascending aorta pressure was used as an input waveform to drive the MCS; the comparison verifies that the model was set up with the correct combination of VAD drive, Aortal compliance, and system impedance.

The experimentally measured flow rates, and corresponding clinical data from the Leducq database, are shown in Figures 2.9 - 2.11. The measured SVC flow rate signal matched well with the clinical flow rate with satisfactory amplitude and phase matching (R^2 =0.84, p > 0.05). The calculated relative root mean square error σ was < 5%, demonstrating the model followed and predicted the clinical data.

The experimental RPA flow rate signal matched well with the clinical measurement with satisfactory amplitude and phase matching (R^2 = 0.78, p > 0.05). The calculated σ < 6% and considered acceptable.

The tested LPA flow rate matched well with the clinical measurement with satisfactory amplitude and phase matching (R^2 = 0.92, p > 0.05). The calculated σ < 3%, provided a good prediction of the clinical data.

In summary, the agreement between experimental and clinical pressure and flow rates were reasonable with satisfactory amplitude and phase matching ($0.6 < R^2 < 0.97$, p > 0.05). The close agreement validates the ability of the experimental model to recapitulate certain clinical measurements of an individual patient. Such a level of validation has never before been shown in a Stage 2 circulation model.

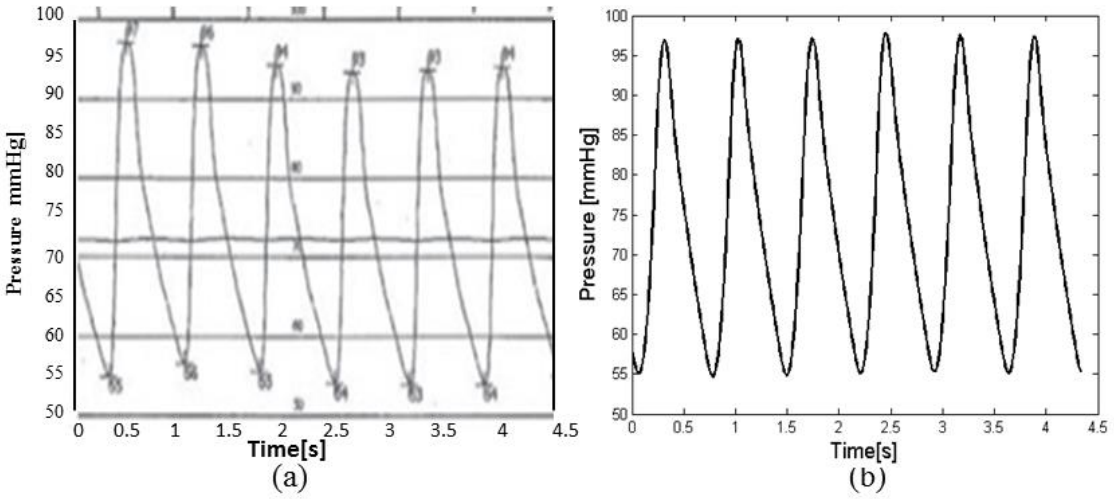

Figure 2.8: Comparison between clinical and experimental results of ascending aorta pressure with UM2, time point 5. (a): Clinical data. (b): Experimental measurement.

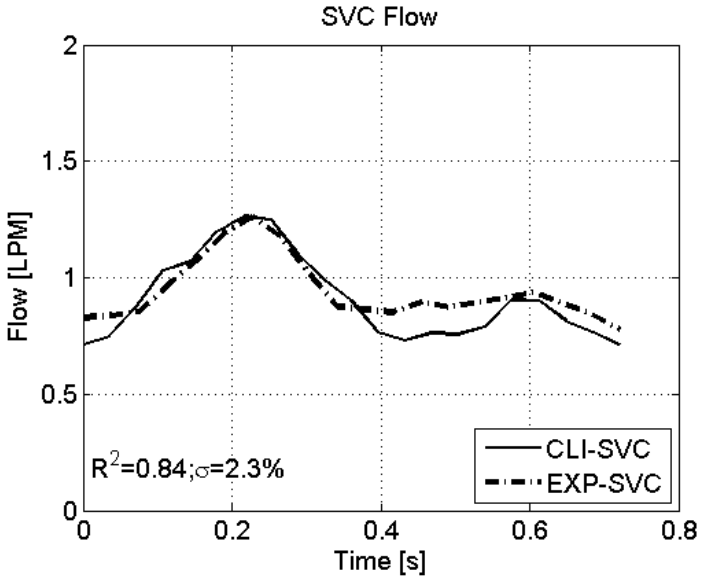

Figure 2.9: Comparison between clinical and experimental SVC flow rate for UM2, time point 5. CLI, clinical; SVC, Super vena cava.

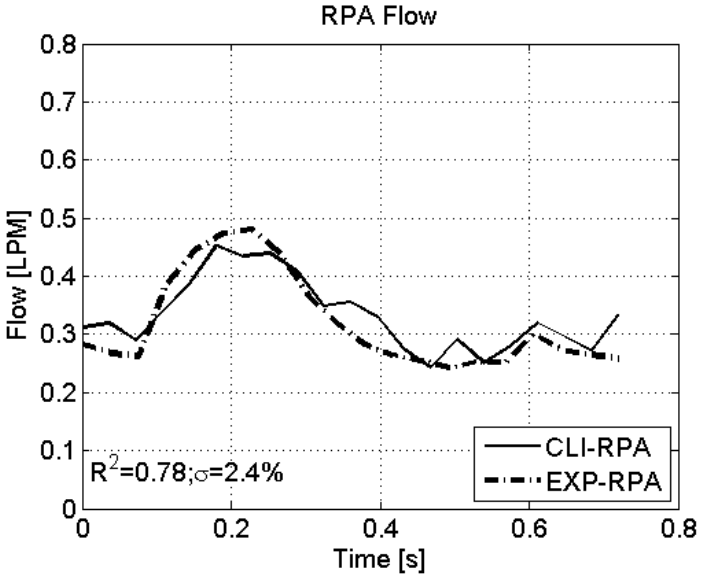

Figure 2.10: Comparison between clinical and experimental RPA flow rate for UM2, time point 5. CLI, clinical; RPA, right pulmonary artery.

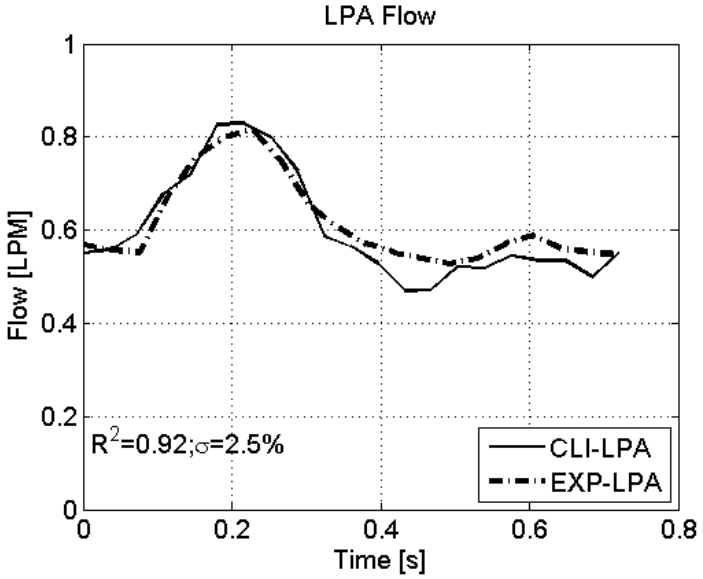

Figure 2.11: Comparison between clinical and experimental LPA flow rate for UM2, time point 5. CLI, clinical; LPA, left pulmonary artery.

Discussion

In this chapter, two *in vitro* multi scale mock circulatory systems capable of simulating either the Stage 1 Norwood with mBTS or the Stage 2 bidirectional Glenn circulation were verified and validated by comparing experimental measurements with numerical or clinical data. The *in vitro* MCS demonstrated the following capabilities: (1) The MCS can capture both the global and local response of the system, (2) the system can be tuned to match patient specific LPN parameters and use accurate 3D models of the anastomosis.

The VAD used in the open-loop MCS was not intended to be a consistent model of ventricle dynamics, nor would that be appropriate, but rather it provided a sufficiently realistic source of flow and pulsatility for the experimental system. As the VAD does not match the preload and afterload sensitivity of a natural heart, the VAD was adjusted in the MCS to maintain a predetermined mean aortic pressure, with HR and atrial pressures fixed. This approach mimics long-term baroregulation of the heart. In order to simplify the experimental setup, the coronary circulation is not modeled.

Although we have developed and used compliant 3D test sections in the MCS in the past [82, 55], the models used here were rigid. However, by using a lumped proximal aortic compliance we do not anticipate significant differences in the hemodynamic data presented. Vukicevic et al. [74] showed that in practice, a lumped compliance element proximal to a rigid three dimensional test section in a multiscale MCS can accommodate the noncompliant test section to produce clinically realistic pressure waveforms.

The data required for tuning of the circuit sometimes must rely on generic information taken from literature, because clinical measurements were limited by the Leducq protocol. Gravitational variation was not part of this experimental program. The test design assumed the patient to be in the supine position under resting conditions, as small children typically are in cardiological testing. The MCS can be tuned for exercise conditions and adjusted to represent upright stature, but these were not tested here.

CHAPTER THREE

THE ASSISTED BIDIRECTIONAL GLENN STUDY

In this section, a mock circulatory system of the conceptual ABG circulation is presented and based on the previously described Stage 1 and Stage 2 mock circulatory systems. The performance of the conceptual ABG circulation was tested and assessed by comparing directly with the performance of the Stage 1 Norwood circulation and the Stage 2 bidirectional Glenn (BDG) circulation for hypothetical patients. The experimental results are also compared to those of a multi-scale numerical model [84] and previously published [83].

Methods

Mock Circulatory System

The physical system of the ABG circulation is built from the Stage 1 and Stage 2 MCS discussed in Chapter 2. The schematic of the ABG circulation is depicted in Figure 3.1. In the ABG, a 2.5 mm diameter shunt with a nozzle was connected between the innominate artery and the SVC just above the SVC-PA junction, while the remaining circulation resembled the BDG. The performance of the ABG is tested using the LPN parameters listed in Table 2.1. To model the ejector effect, a surgical ligaclip was placed over the shunt as proposed by Esmaily-Mghadem [84]. Tests were run using two patients cases of iPVR = 2.3 WU/m^2 and iPVR =7.0 WU/m^2.

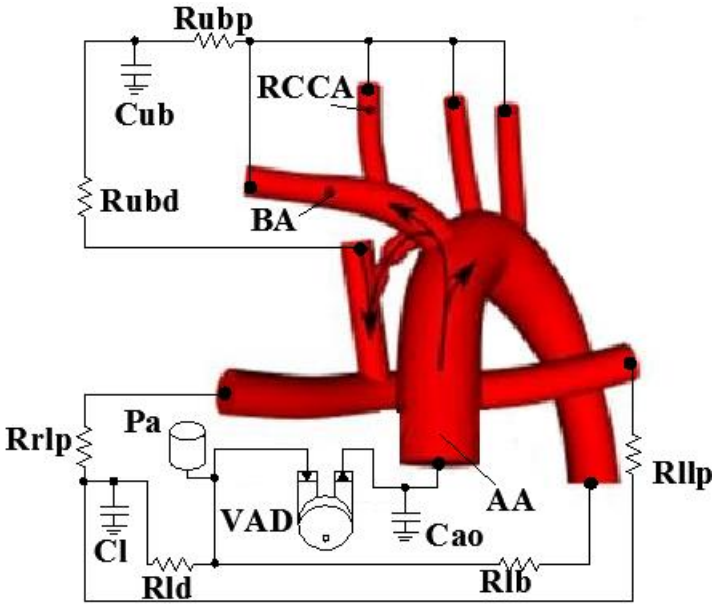

Figure 3.1: The ABG Mock circulatory system lumped parameter network coupled with the ABG three dimensional anastomosis. Cao, aorta compliance; Cl, lung compliance; Cup, upper body compliance; Rlb, lower body resistance; Rld, lung distal resistance; Rllp, left lung proximal resistance.

Results

Experimental results were compared directly to the multi-scale numerical results reported by Esmaily-Moghadam [84]. In the experimental model, the nozzle diameter d to shunt diameter D (or β= d/D) was modeled exactly as in the numerical study. Because the nozzle was created by a clip, a hydraulic diameter for the nozzle was used. The resulting β = 0.57. The measured input conditions of time-based ascending aortic pressure are given in Figure 3.2 with mean values in Table 3.1 and compared directly to the numerically applied waveforms. The time-based agreement between experimental and numerical was quite good ($0.64 < R^2 < 0.86$, $p > 0.05$) and mean aortic pressures were well within 1.0 mmHg difference. The calculated rms error ranged from 3.0% to 7.0%.

The good matching between the time-based aortic pressures indicates that the input waveform used were the same in both cases.

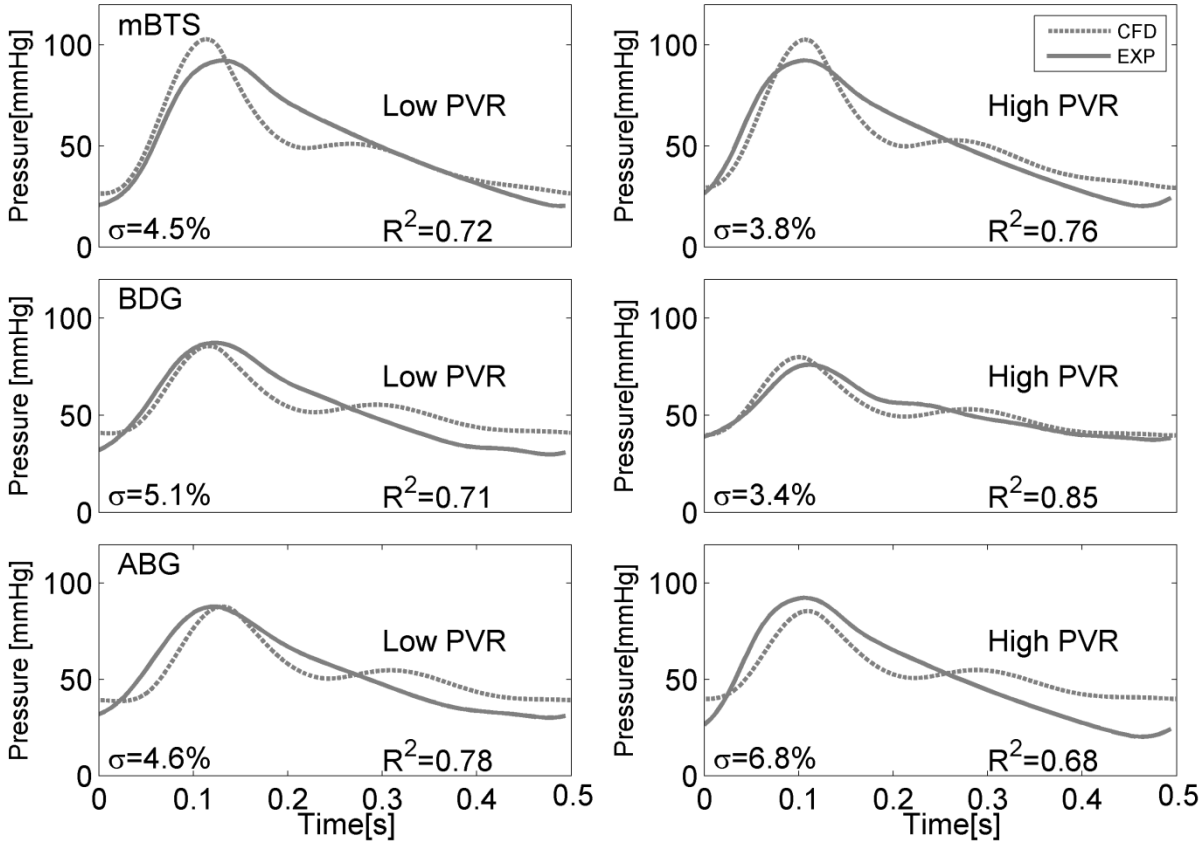

Figure 3.2: Time-based ascending aortic pressures applied in the experimental and numerical studies R^2 , coefficient of determination; σ , rms error.

Mean flow comparisons, given in Figure 3.3 with mean values in Table 3.1 were nearly identical between the numerical and experimental results ($p > 0.05$). Pulmonary blood flow is highest for the mBTS circulation, while the ABG circulation provides a 30% to 38% improvement in pulmonary blood flow over the BDG circulation. SVC flows are comparable between circulations at normal PVR ($p > 0.05$). SVC flow increases with PVR in the mBTS circulation, where SVC competes with the shunt, but decreases for the

ABG and BDG circulations. Pulmonary pressures are highest for the mBTS circulation and lowest with the BDG circulation.

Table 3.1: Mean pressure (P), flow rate (Q), and oxygen delivery (OD) comparisons between experimental and numerical models [84].

Case PVR			MBTS L	BDG L	ABG L	MBTS H	BDG H	ABG H
		Unit						
Pao	**CFD**	***mmHg***	52.1	54.6	55.2	53.7	51.8	54.9
	EXP	***mmHg***	52.0±0.2	54.5±0.2	55.1±0.2	54.1±0.4	51.6±0.4	54.2±0.4
Psvc	**CFD**	***mmHg***	2.51	6.01	7.91	2.41	11.13	14.94
	EXP	***mmHg***	2.4±0.1	6.1±0.1	8.1±0.1	2.5±0.1	11.0±0.1	14.7±0.1
Plpa	**CFD**	***mmHg***	9.55	4.89	6.11	18.28	10.20	13.51
	EXP	***mmHg***	10.6±0.1	5.0±0.1	6.7±0.1	18.5±0.1	9.9±0.1	13.8±0.1
Prpa	**CFD**	***mmHg***	7.85	4.86	6.11	20.12	10.18	13.51
	EXP	***mmHg***	9.0±0.1	4.8±0.1	6.8±0.1	19.2±0.1	10.1±0.1	14.1±0.1
Qsvc	**CFD**	***L/min***	0.48	0.50	0.47	0.50	0.42	0.40
	EXP	***L/min***	0.47±0.01	0.48±0.01	0.46±0.01	0.51±0.01	0.42±0.01	0.40±0.01
Qlpa	**CFD**	***L/min***	0.40	0.25	0.32	0.38	0.21	0.29
	EXP	***L/min***	0.41±0.01	0.25±0.01	0.32±0.01	0.38±0.01	0.21±0.01	0.29±0.01
Qrpa	**CFD**	***L/min***	0.52	0.25	0.32	0.42	0.21	0.28
	EXP	***L/min***	0.52±0.01	0.25±0.01	0.32±0.01	0.42±0.01	0.21±0.01	0.29±0.01
Qlb	**CFD**	***L/min***	0.61	0.67	0.66	0.63	0.64	0.66
	EXP	***L/min***	0.61±0.01	0.67±0.01	0.66±0.01	0.63±0.01	0.63±0.01	0.66±0.01
Qshunt	**CFD**	***L/min***	NA	NA	0.17±0.03	NA	NA	0.17±0.03
	EXP	***L/min***	NA	NA	0.18±0.03	NA	NA	0.18±0.03
Qs	**CFD**	***L/min***	1.09	1.17	1.13	1.13	1.06	1.06
	EXP	***L/min***	1.08±0.02	1.15±0.02	1.12±0.02	1.14±0.02	1.05±0.02	1.06±0.02
Qp/Qs	**CFD**	**-**	0.85	0.43	0.58	0.71	0.40	0.54
	EXP	**-**	0.86±0.01	0.43±0.01	0.57±0.01	0.70±0.01	0.40±0.01	0.55±0.01
CO	**CFD**	***L/min***	2.01	1.17	1.31	1.93	1.06	1.23
	EXP	***L/min***	2.01±0.01	1.17±0.01	1.30±0.01	1.94±0.01	1.05±0.01	1.24±0.01
OD r = 0.5	**CFD**	$\boldsymbol{mL_{O2}/s}$	2.96	3.25	3.38	2.92	2.79	3.07
	EXP	$\boldsymbol{mL_{O2}/s}$	2.95±0.27	3.21±0.27	3.34±0.27	2.93±0.27	2.76±0.27	3.09±0.27
OD r = 0.4	**CFD**	$\boldsymbol{mL_{O2}/s}$	2.96	3.48	3.54	2.92	3.01	3.24
	EXP	$\boldsymbol{mL_{O2}/s}$	2.95±0.27	3.40±0.27	3.49±0.27	2.93±0.27	2.98±0.27	3.25±0.27
OD r =0.7	**CFD**	$\boldsymbol{mL_{O2}/s}$	2.96	2.87	3.09	2.92	2.36	2.76
	EXP	$\boldsymbol{mL_{O2}/s}$	2.95±0.27	2.79±0.27	3.03±0.27	2.93±0.27	2.32±0.27	2.77±0.27

L: normal PVR; H: high PVR; ao, aorta; svc, superior vena cava; lpa, left pulmonary artery; rpa, right pulmonary artery; lb, lower body; s, systemic; p, pulmonary; CO, cardiac output. Mean value± standard error

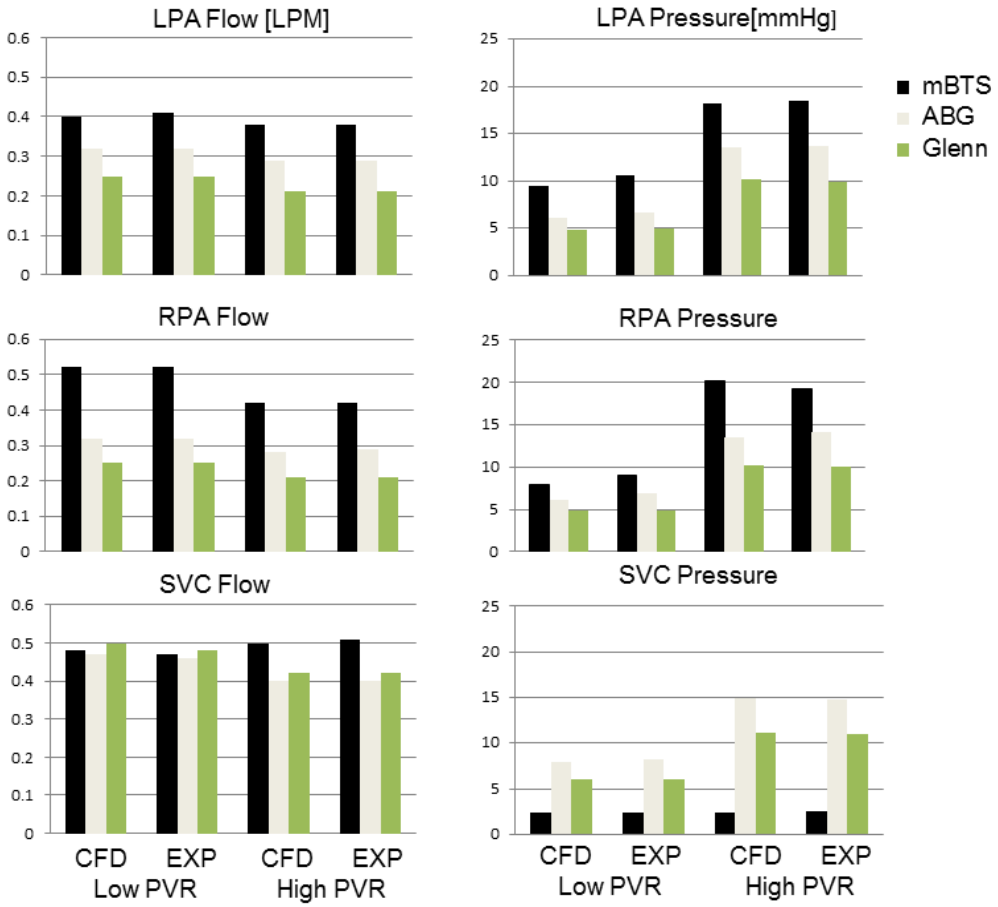

Figure 3.3: Numerical and experimental value comparisons of mean flow rate and pressure for the three circulations. CFD, numerical; EXP, experimental; LPA, left pulmonary artery; RPA, right pulmonary artery; SVC, super vena cava; PVR, pulmonary vascular resistance

Oxygen delivery (OD) was calculated using the method detailed in Appendix H using measurements of flow rates to the various circulation branches. As indicated in Figure 3.4 and Table 3.1, the ABG circulation provided the highest systemic OD of the three circulations regardless of PVR ($p > 0.05$). Differences between experimental and numerically predicted mean values for each circulation showed no significant difference ($p > 0.05$). When the oxygen consumption ratio was varied from $r = 0.4$ to $r = 0.7$ (Table

3.1), the ABG circulation also provided the highest OD. Notably, as the value of r was increased in the ABG.

Time-based signal comparisons between numerical and experimental mBTS, BDG and ABG models are given in Figure 2.7, Figure 3.5 and Figure 3.6, respectively. Time-based LPA and RPA flows and pressures are well reproduced between the models ($0.74 < R^2 < 0.91$). Mean values were nearly identical ($p > 0.05$). The calculated root mean square error σ ranged from 1.0% to 5.0% for both flow rate predictions and pressure predictions. In the ABG model, the numerical prediction of SVC flow shows somewhat more pulsatility during systole than the experiment ($R^2 = 0.61$); however, the maximum, minimum and mean values compare very well and the time-based SVC pressures are nearly identical between the models.

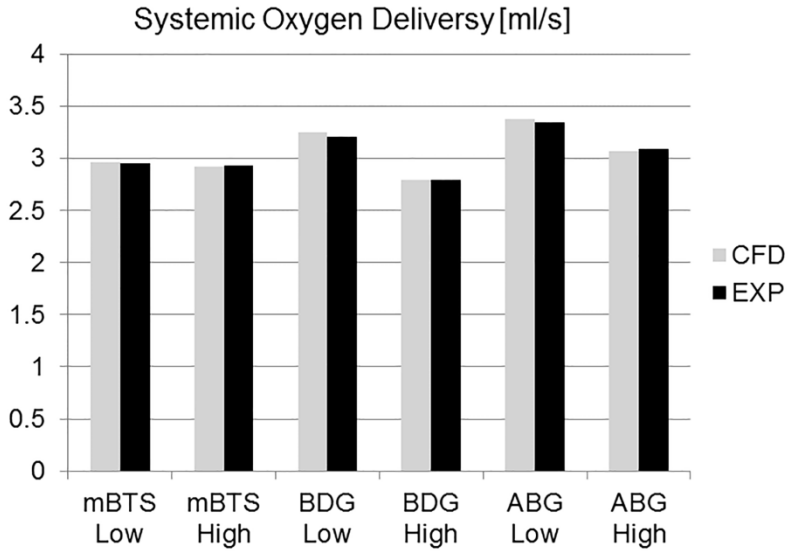

Figure 3.4: Comparison of experimental estimations of systemic oxygen delivery among BT-shunt Norwood circulation, ABG circulation and bidirectional Glenn (BDG) circulation.

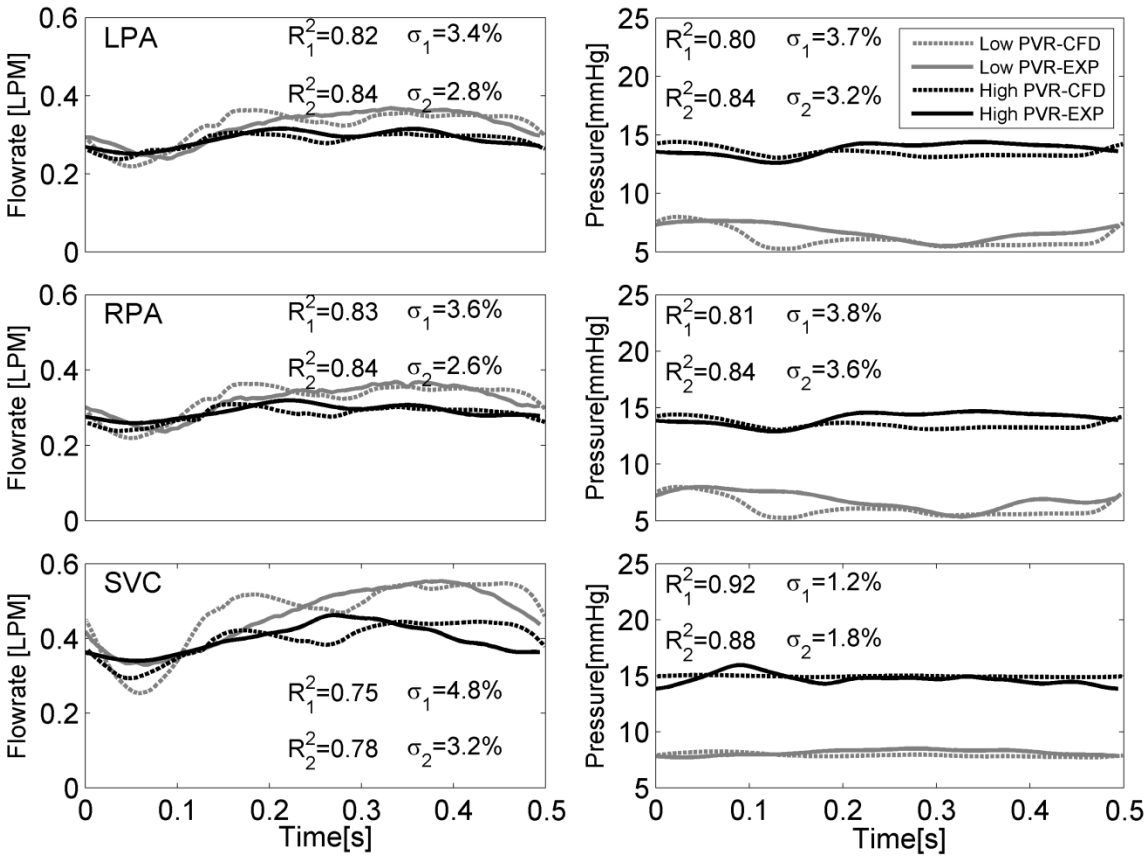

Figure 3.5: Time-based experimental (solid) and numerical (dashed) flow rate and pressure signals for the ABG circulation under low and high PVR. Subscript: 1, low PVR; 2, high PVR.

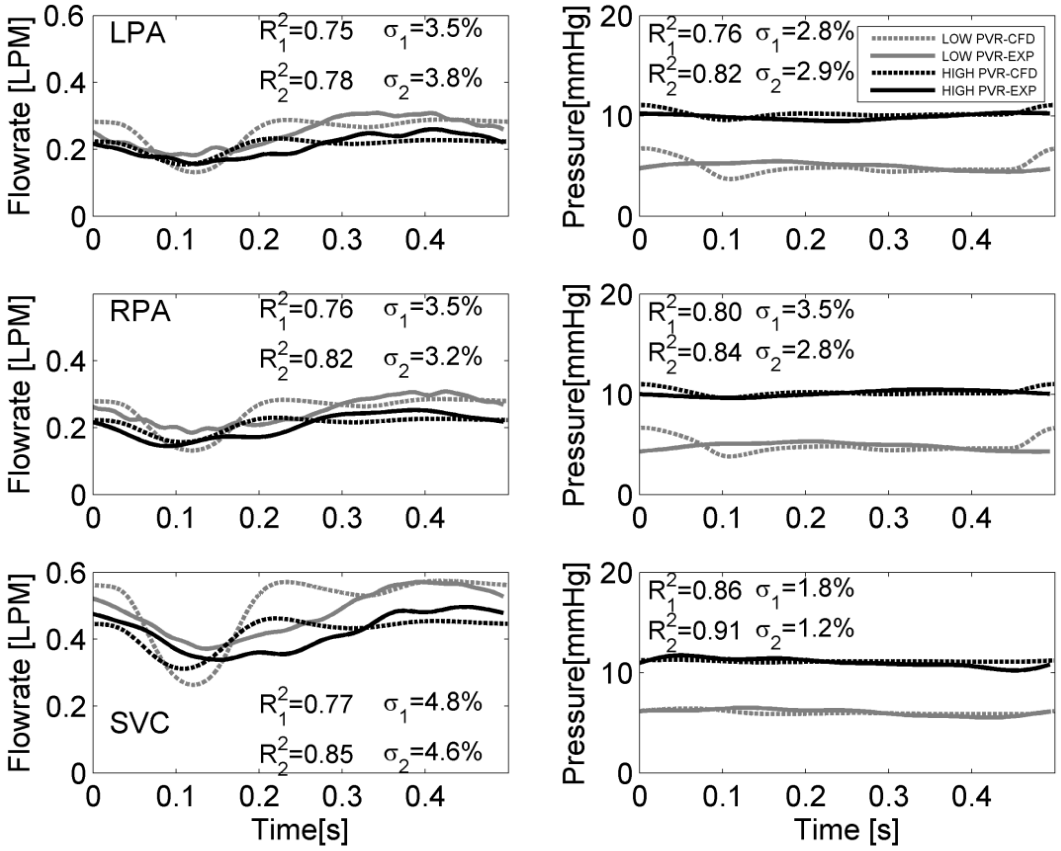

Figure 3.6: Time-based experimental (solid) and numerical (dashed) flow rate and pressure signals for the BDG circulation under low and high PVR. Subscript: 1, low PVR; 2, high PVR.

Discussion

This chapter presents an *in vitro* multi-scale model of the Norwood with mBTS and Glenn (BDG) circulations and used it to explore a novel approach for a first stage palliation of univentricular physiology called the ABG circulation.

The ABG circulation augmented pulmonary blood flow in a superior cavopulmonary connection using a shunt ending in a nozzle so as to supply high-energy flow from the systemic circulation. Based on ejector pump concepts, the approach improved systemic OD and achieved balanced systemic and mixed venous saturation

while maintaining clinically acceptable SVC pressures [83]. Also, increasing pulmonary arterial blood flow should offer several benefits including higher pulmonary arterial pressure and improved saturation over the Glenn [91]. McElhinney et al. [92] suggest that these would allow for improved exercise tolerance and reduce baseline cyanosis. The ABG adds a component of pulsatility to the pulmonary blood flow, which could potentially improve pulmonary vascular development and exercise tolerance [92, 93].

Ejector Pump Effect Analysis

The hypothesis that an ejector pump advantage can be adopted in a superior cavo-pulmonary circulation, where the low-energy pulmonary blood flow can be assisted by an additional source of high energy flow from the systemic circulation was investigated. But there is no prior approach to calculate the magnitude of ejector pump effect. In Zhou et al.[83], the effect of the ejector-shunt was quantified by comparing the pressure difference between the SVC and pulmonary artery (PA) relative to the total pulmonary blood flow. From Table 3.1, while this pressure gradient ($P_{SVC} - P_{PA}$) remains about the same between the BDG and the ABG circulations, the corresponding pulmonary blood flow ($Q_{LPA} + Q_{RPA}$) is increased in the ABG over the BDG. So the pulmonary blood flow is increased 30 – 38% for the two conditions studied for the same pressure gradient. In effect, the ejector-shunt effect reduces the local flow resistance at the SVC-PA junction.

This method gave a general idea on how to access the ABG improvement over the BDG in neonates. But in essence, the BDG and ABG have different physiological structures. The increased pulmonary blood flow in the ABG compared with the BDG

arises from the shunt. But does the nozzle present an "ejector offset" as proposed or is the ABG performance a result of the resistant shunt only or something in between?

An idea naturally came out was to compare the ABG performance with an "ABG" which had no ejector effect. This could be achieved by removing the nozzle far away from the shunt-SVC junction, close to the aorta side of the shunt. In order to examine if the nozzle produced the ejector effect, a test was done to compare the hemodynamics with three different nozzle placements as shown in Figure 3.7: one 2.5 mm diameter shunt was coupled with a tapered nozzle having a β of 0.60 at the positions of (A) 0 mm; (B) 3 mm; and (C) 6 mm away from the SVC-shunt junction.

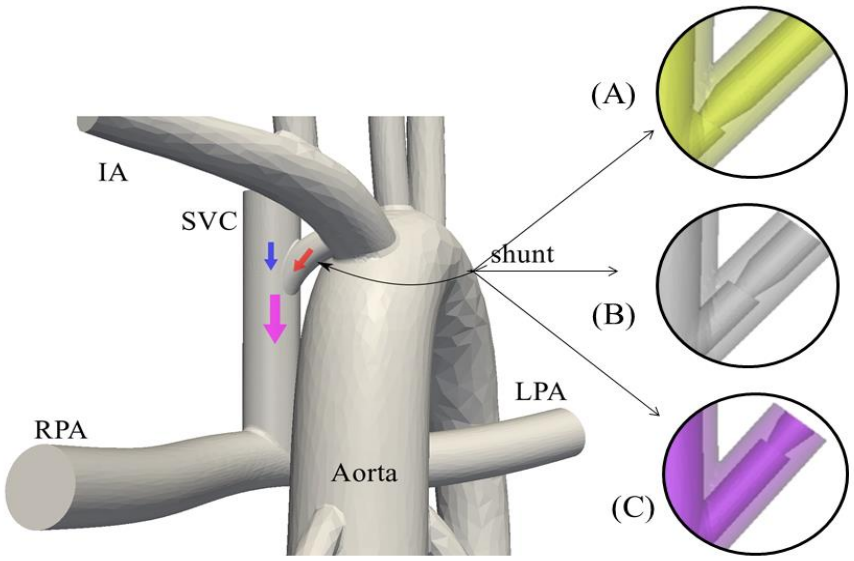

Figure 3.7: Schematic of the shunts tested to examine the ejector pump effect. L is the distance from the nozzle to the Shunt-SVC junction.

In theory, the resistance of the three shunts should be equivalent. If the ejector effect exists, the C type shunt should produce the weakest ejector pump effect, since the long distance would allow the flow to recover the pressure and attenuate any ejector

effect. The tested results, including the pressure and flow signals of the SVC, LPA, and RPA branches are given in Figure 3.8. As the nozzle was moved from L = 0mm to 6mm, the SVC pressure increased about 0.6 mmHg and the pulmonary pressure declined about 0.3 mmHg. The SVC flow decreased 0.01LPM as the nozzle was moved away from the SVC. To clearly demonstrate the nozzle effect, two parameters were calculated. The first one was the SVC and pulmonary artery (PA) pressure difference. The second was the SVC and PA pressure difference relative to the PA flow rate, which was defined previous as the ejector resistance [83]. The final calculated results were given in Figure 3.9. Shunt A demonstrated the lowest SVC and pulmonary artery pressure difference and the least ejector resistance between the three shunts for either value of PVR. This result demonstrates the existence of an ejector effect. Also from Figure 3.9, the ejector effect weakened as PVR increased, as expected. Future work may explore more advanced nozzle designs with stronger ejector effects.

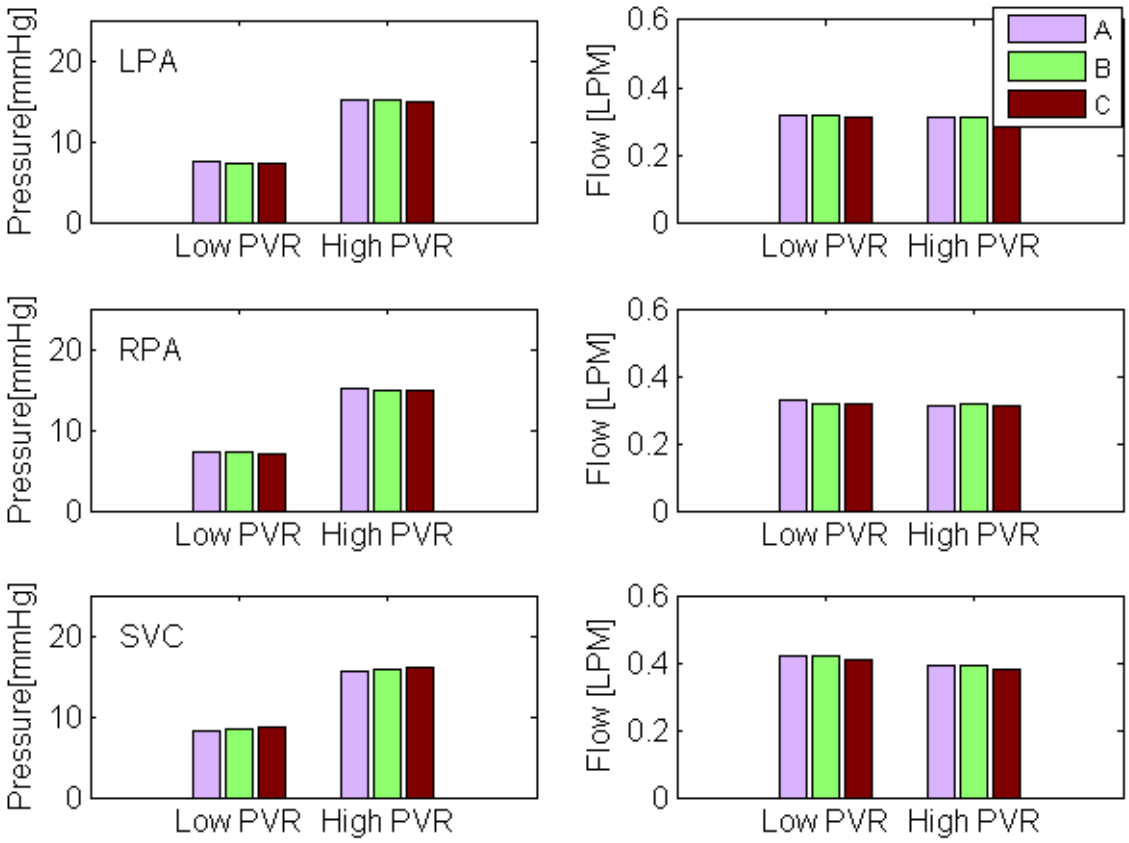

Figure 3.8: Tested pressures and flows between three different shunts. A: 2.5mm shunt; B, 1.5mm shunt; C, 2.5mm shunt attached a tapered nozzle with a β of 0.6; LPA, left pulmonary artery; PVR, pulmonary vascular resistance; RPA, right pulmonary artery; SVC, superior vena cava.

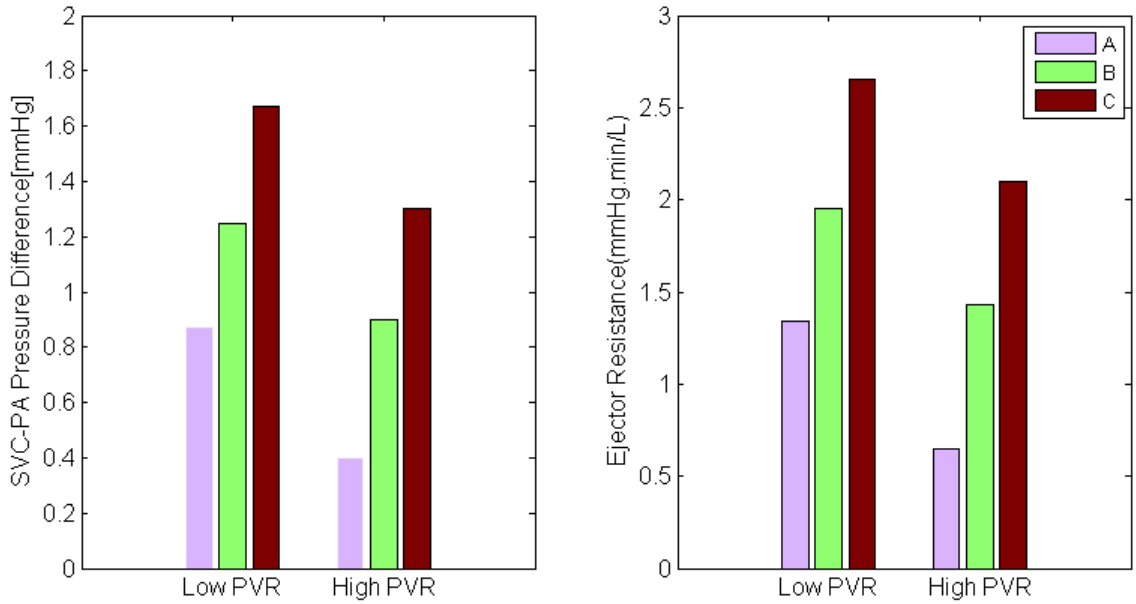

Figure 3.9: Tested SVC to pulmonary artery pressure difference and ejector resistance between three shunts. PA, pulmonary artery; PVR, pulmonary vascular resistance; SVC, superior vena cava.

Summary

In summary, the hypothesis that an ejector pump advantage can be adopted in a superior cavo-pulmonary circulation, where the low-energy pulmonary blood flow can be assisted by an additional source of high energy flow from the systemic circulation was validated. The ABG could be used as a Stage 1 palliation option for single ventricle heart disease patients. It could provide more stable pulmonary blood flow source and relieve the ventricle load compared with the Norwood circulation.

CHAPTER FOUR

THE ABG NOZZLE PARAMETRIC STUDY

In the previous study of the ABG circulation, the shunt and geometries were fixed to compare to a numerical study. In this chapter, parametric studies are presented of the shunt and nozzle used in the ABG connecting the SVC and systemic circulation. Results are presented and suggestions on parameters design are given.

Method

Parameters

The shunt orientation and nozzle characteristics are investigated. Investigated parameters include: nozzle hydraulic diameter to shunt hydraulic diameter ratio β, nozzle angle θ^{o}, nozzle position L relative to the SVC-shunt junction, and nozzle shape. The studies are made using PVR values of 2.3 $WU-m^2$ and 7 $WU-m^2$ within the ABG circulation MCS model.

Nozzle Designs

Four nozzle designs were used and these are shown in Figure 4.1. These include: a concentric nozzle, a tapered shunt, a protruding nozzle extending into the SVC, and an external banded shunt (surgical ligaclip design of [84]). Location of the nozzle within the

shunt is designated as L, with L= 0 placing the nozzle at the shunt-SVC junction (Figure 4.1). Shunt angle is measured relative to the SVC. Nozzle diameter d is varied relative the shunt diameter D, where $\beta = d/D$ as before. Shunt diameter is fixed at D = 2.5mm for all tests.

The concentric nozzle (Fig 4.1) allows for variations of β (nozzle diameter to shunt diameter) in a controlled manner over a range of $0.24 < \beta < 0.84$. The nozzle was situated within the shunt at the SVC-shunt junction (L = 0mm) and shunt angle θ was held constant at 40 degrees (Figure 4.1) in these tests.

The effect of the SVC-shunt angle (θ) on the ABG performance was also investigated. Five angle configurations (20^o, 30^o, 40^o, 50^o, 60^o) were tested in this study with β set to 0.6 and L set to 0 mm (Figure 4.1, subfigure D, details of the parameters are shown in subfigure E) using the concentric nozzle. In order to study the nozzle position effects, four different positions were tested: L = -1.5mm, 0mm, 1.5mm and 3.0mm. A positive value means that the nozzle was located within the SVC branch; a negative value represents that the nozzle was located within the shunt towards the aorta, relative to L = 0, the SVC-shunt intersection.

Nozzle shape may have an effect on the ABG performance, so a convergent tapered nozzle, shown in Figure 4.1 (subfigure C), was tested and the results were compared to the previously introduced concentric divergent nozzle sharing the same L, β and θ.

One idea is to move the high energy blood flow from systemic circulation closer to the pulmonary artery. To study this, a nozzle that protrudes into the SVC (Figure 4.1,

subfigure D) was used. Nozzle protrusion into the SVC could produce a sizable blockage effect, which may unfavorably increase SVC pressure upstream of where the nozzle protruding into the SVC. So a curved nozzle was designed to reduce the blockage area. The STL model and photograph of the inside view of the nozzle are shown in Figure 4.1 (subfigure A).

Overall, the tests used 16 different nozzle designs of nozzle shape, nozzle-to-shunt hydraulic diameter ratio β, position L and angle θ in the ABG circulation. The parameters of the 16 designs are presented in Table 4.1. The design with case number 4 (concentric nozzle, $\beta = 0.60$, $L = 0$, $\theta = 40^0$) was compared in all the 4 study categories.

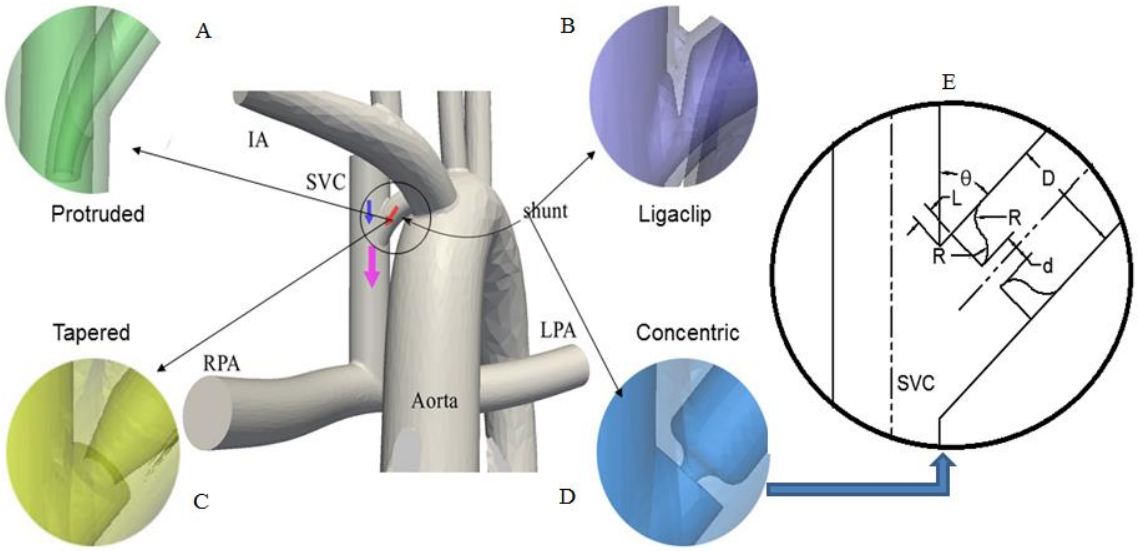

Figure 4.1: The Assisted Bidirectional Glenn shunt location. Ligaclip nozzle/shunt geometry is used in simulation [84].

Table 4.1: Design parameters matrix of the nozzle tested.

Study Category	Case	Shape	d	D	β	θ	L	Curved
Diameter ratio (β)	1	Concentric	0.60	2.5	0.24	40	0	NO
	2	Concentric	0.90	2.5	0.36	40	0	NO
	3	Concentric	1.20	2.5	0.48	40	0	NO
	4	Concentric	1.50	2.5	0.60	40	0	NO
	5	Concentric	1.80	2.5	0.72	40	0	NO
	6	Concentric	2.10	2.5	0.84	40	0	NO
Angle (θ)	7	Concentric	1.50	2.5	0.60	20	0	NO
	8	Concentric	1.50	2.5	0.60	30	0	NO
	4	Concentric	1.50	2.5	0.60	40	0	NO
	9	Concentric	1.50	2.5	0.60	50	0	NO
	10	Concentric	1.50	2.5	0.60	60	0	NO
Shape (S)	11	Tapered	1.50	2.5	0.60	40	0	NO
	4	Concentric	1.50	2.5	0.60	40	0	NO
	12	Protruded	1.50	2.5	0.60	40	0	YES
	13	Ligaclip	1.47	2.5	0.57	40	0	NO
L	14	Concentric	1.50	2.5	0.60	40	-0.15	NO
	4	Concentric	1.50	2.5	0.60	40	0	NO
	15	Concentric	1.50	2.5	0.60	40	0.15	NO
	16	Concentric	1.50	2.5	0.60	40	0.30	NO

d, nozzle minimum diameter; D, shunt diameter; L, Distance between nozzle and SVC-Shunt junction; β, nozzle diameter to shunt diameter ratio; θ, shunt angle.

Results

Results of the nozzle parametric tests are given in Figure 4.2 to Figure 4.6 and Table 4.2 and Table 4.3. The parametric effects are discussed below.

Diameter effects

In studies using the concentric nozzle, Figure 4.2 shows the resulting time based flow and pressure traces as functions of diameter ratio β. Table 4.2, Table 4.3 and Figure 4.3 summarize the mean results. The standard error for each measurement was also included in Table 4.2 and Table 4.3. The experimental results for the original ligaclip design geometry (β = 0.57) are also provided for comparison. As shown in Figure 4.2, all

pressures and flows became more pulsatile with the increasing β values, as more arterial pulsatility was communicated through the shunt. Mean RPA and LPA pressures and flows increased, as expected, as β increased. The LPA pressure increased from 5.0 mmHg to 11.0 mmHg as PVR increased from 2.3 WU-m^2 to 7.0 WU-m^2. The similar trend was seen in the RPA and SVC pressures. The value of Qp / Qs was sensitive to β but not to PVR; it varied from 0.44 to 0.74 as β increased from 0.24 to 0.84. For PVR value of 2.3 WU-m^2, as β increased from 0.24 to 0.84, the shunt flow increased from 0.04 LPM to 0.36 LPM, and the cardiac output increased from 1.16 LPM to 1.43 LPM. This was due to a larger β, which yielded a smaller flow resistance. For β = 0.72 and above, SVC pressure rose above 18.0 mmHg, and SVC flow dropped noticeably as the increasing shunt flow competed with increasing SVC pressure. Geometries using a β between 0.48 and 0.60 showed high systemic oxygen delivery (OD) (Fig 4.3) with calculated values above 3.00 ml_{O_2} / s. Inspection of OD and measured pressure and pulmonary flow suggests that a good value for β falls between 0.48 and 0.60.

Angle effects

The concentric nozzle was used as SVC-shunt angle was varied between $20^o \le \theta \le 60^o$. For these tests, the β value was kept constant at 0.60 and L = 0. Details of the parameters are listed in Table 4.1 (case 7 to 11). The input aortic pressure kept constant at 50.5 mmHg for all the cases. The mean values of the measured and calculated parameters are given in Figure 4.4 and Table 4.2 to 4.3.

The SVC pressure remained constant between 8.2mmHg to 8.7mmHg for PVR at 2.3WU-m^2 and 15.2mmHg to 15.6mmHg for PVR at 7.0 WU-m^2 as angle varied. This variation is well within clinical significance, indicating that SVC pressure was not very sensitive to shunt angle. The tendency was repeated in the LPA and RPA pressures.

The pulmonary artery flow rate decreased about 0.01-0.02 LPM as pulmonary vascular resistance (PVR) increased from 2.3 to 7.0 WU-m^2 for all the tested angles. For all angles, the lower body flow rate remained constant between 0.64 ~ 0.65 LPM with PVR.

The LPA and RPA flow rates reached a maximum (0.33 LPM for 2.3 WU-m^2 and 0.32 LPM for 7.0 WU-m^2) at an angle of 30^o and then decreased as angle increased for either PVR values. But the difference among different angles was small (maximum difference 0.02 LPM, 6% absolute).

The SVC flow rate reached a maximum of 0.44 LPM at an angle of 30^o for 2.3 WU-m^2 case and a maximum of 0.42 LPM at an angle of 40^o for 7.0 WU-m^2 case and then decreased as angle increased. But the difference among different angles was small (maximum difference 0.04LPM, 10% absolute). The cardiac output (CO) showed a similar trend and reached a maximum at an angle of 30^o.

The shunt flow reached a maximum at the angle of 30^o and then deceased as the angle θ decreased for either PVR values. It should be noted that the shunt flow was not measured directly. It was calculated with mass continuity and the uncertainty was 0.03 LPM (details in Appendix D). Accordingly, differences between the shunt flows between angles were not statistically significant.

The oxygen delivery (OD) attained its highest value at an angle of 30^o and 40^o for either value of PVR. The range of OD varied 9.5% (3.35 mlO_2 / ml compared with 3.06 mlO_2 / ml) between the best and the worst cases.

In summary, the influence of angle θ on the ABG performance was not significant. Shunt angle of 30^o to 40^o showed a slight improvement on pulmonary blood flow and oxygen delivery over other angles. A recommended angle was between 30^o and 40^o.

Shape Effects

Four different shapes, including the initial proposed ligaclip nozzle, a concentric internal nozzle, a tapered nozzle and a protruding tapered nozzle, were tested to examine the nozzle shape effects on the ABG circulation. For these tests, the β was kept constant at 0.6, θ was set at 40^o and the location L was set at 0 mm.

The mean values of the measured and calculated parameters are given in Figure 4.5 and Table 4.2 to 4.3. For these tests, the aortic pressure was kept constant at 50.5 mmHg for either value of PVR and each shape design.

The SVC pressure remained constant around 8.2 mmHg for PVR at 2.3 WU-m^2 and around 15.6 mmHg for PVR at 7.0 WU-m^2 with variation in nozzle shape, except for ligaclip due to its smaller β value (0.57 compared with 0.60). This suggested that the shapes tested did not influence the SVC pressure. The similar trend was shown in the LPA and RPA pressures.

The pulmonary artery flow decreased by about 0.01~0.02 LPM as pulmonary vascular resistance (PVR) increased for all the tested shapes. For either shape, the lower body flow rate remained nearly constant between 0.64 ~ 0.65 LPM for either value of PVR.

The LPA flow rate remained constant at 0.32 LPM with nozzle shape variation, suggesting the LPA flow rate was not sensitive to the nozzle shapes tested. As the LPN values were set the same in the two pulmonary branches, the same trend was seen in the RPA.

The SVC flow rate stayed constant at 0.42 LPM for 2.3 WU-m^2 and 0.39 LPM for 7.0 WU-m^2 for the different nozzle shapes, showing the SVC flow was slightly sensitive to PVR but was not sensitive to the nozzle shapes tested.

The differences between the shunt flows of each shape were not statistically significant and remained constant for nozzles having the same β value. A similar trend was found in the systemic oxygen delivery.

In summary, there were no statistical differences between the ABG performances with the 4 different nozzle shapes presented in the study.

Location effects

The concentric nozzle was placed at four different locations (L= -1.5mm, 0mm, 1.5mm and 3mm, details in Figure 4.1, subfigure E) to investigate the effects of nozzle location. The β value was kept constant at 0.6 and θ was set at 30^o.

The mean values of the measured and calculated parameters are given in Figure 4.6 and Table 4.2 to 4.3. From Figure 4.6, for the high PVR case with an L value of 3mm (positive value means the nozzle was protruding within the SVC), the SVC pressure increased from 15.0mmHg to 26.0mmHg, a dangerous level for single ventricle patients.

For a PVR of 2.3 WU-m^2, the SVC flow rate signal drop from 0.42 LPM to 0.26 LPM. This suggested a blockage within the SVC branch. The pulmonary blood flow showed a similar trend as the SVC flow. The pulmonary blood flow dropped from 0.32 LPM to 0.26 LPM for a PVR of 2.3 WU-m^2. Oxygen delivery (OD) dropped from 3.19 to 2.59 ml_{o_2} / s for a PVR of 2.3 WU-m^2.

For a PVR of 2.3 WU-m^2, the cardiac output decreased from 1.29 LPM to 1.18 LPM as L changed from -1.5mm to 3.0mm, due to the extra systemic resistance caused by the SVC blockage. The shunt flow showed an inverse decline and increased from 0.22 LPM to 0.27 LPM for a PVR of 2.3 WU-m^2.

In summary, a large protruding shunt (L=3.0mm here) into the SVC will partially block the SVC branch and cause a dangerous situation for single ventricle patients.

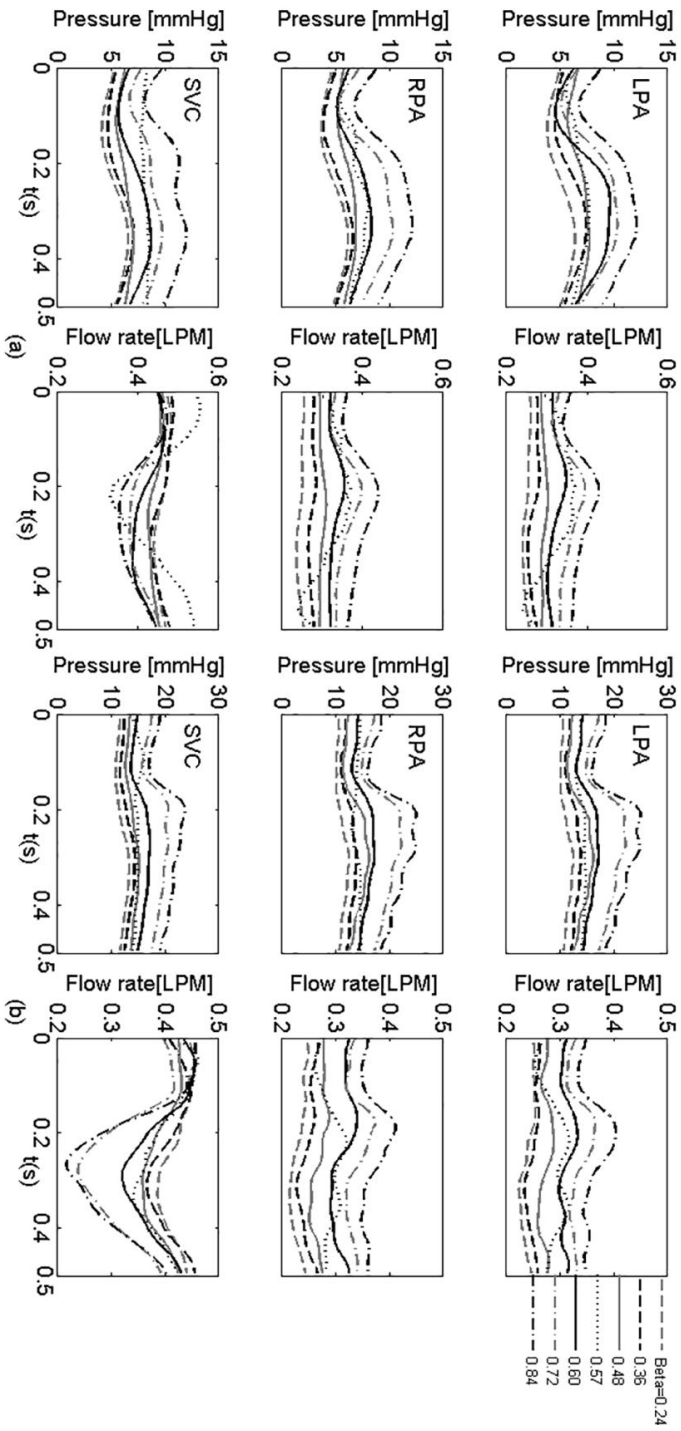

Figure 4.2: Time dependent flow and pressure signals comparison within ABG circulation under (a) low PVR and (b) high PVR for different nozzle to shunt diameter ratios (β). Values for β = 0.57 use the ligaclip geometry of Ref. 84

Table 4.2: Comparison of pressures between different nozzle designs for lower PVR (L) and High PVR (H) case

Case		Study Goal		Pao	Psvc	Plpa	Prpa
1	**L**	β	0.24	55.6±0.3	5.3±0.1	4.8±0.1	4.8±0.1
	H			50.3±0.2	11.9±0.1	11.0±0.1	11.0±0.1
2	**L**		0.36	55.7±0.3	5.7±0.1	5.2±0.1	5.2±0.1
	H			50.9±0.3	12.9±0.1	12.4±.0.1	12.5±0.1
3	**L**		0.48	56.0±0.3	6.3±0.1	6.0±0.1	6.1±0.1
	H			50.8±0.2	13.9±0.1	13.7±0.1	13.7±0.1
4	**L**		0.60	55.6±0.4	8.2±0.1	7.4±0.1	6.9±0.1
	H			50.6±0.3	15.6±0.1	15.2±0.1	15.2±0.1
5	**L**		0.72	55.6±0.4	8.4±0.1	8.5±0.2	8.2±0.1
	H			50.3±0.2	18.5±0.2	18.6±0.2	18.7±0.1
6	**L**		0.84	55.8±0.3	10.5±0.1	9.9±0.1	9.9±0.1
	H			50.8±0.3	20.4±0.1	20.5±0.3	20.5±0.2
7	**L**	θ	20°	55.4±0.3	8.5±0.1	7.3±0.1	7.1±0.1
	H			50.8±0.3	15.4±0.1	14.1±0.1	14.0±0.2
8	**L**		30°	55.6±0.3	8.1±0.1	7.3±0.1	7.0±0.1
	H			50.3±0.3	15.5±0.1	15.5±0.2	15.4±0.1
4	**L**		40°	55.6±0.4	8.2±0.1	7.4±0.1	6.9±0.1
	H			50.6±0.3	15.6±0.1	15.2±0.1	15.2±0.1
9	**L**		50°	55.7±0.3	8.5±0.1	7.6±0.1	7.7±0.1
	H			50.5±0.3	15.2±0.1	15.4±0.1	15.4±0.1
10	**L**		60°	55.4±0.3	8.7±0.1	7.7±0.1	7.7±0.1
	H			50.5±0.3	15.2±0.1	14.8±0.1	14.8±0.1
11	**L**	S	T	55.4±0.3	8.1±0.1	7.1±0.1	7.0±0.1
	H			50.7±0.3	15.4±0.1	15.3±0.1	15.4±0.1
4	**L**		C	55.6±0.4	8.2±0.1	7.4±0.1	6.9±0.1
	H			50.6±0.3	15.6±0.1	15.2±0.1	15.2±0.1
12	**L**		P	55.8±0.3	8.0±0.1	6.8±0.1	6.8±0.1
	H			50.4±0.3	15.7±0.1	15.4±0.1	15.4±0.1
13	**L**		Ligaclip	55.2±0.3	8.1±0.1	6.7±0.1	6.8±0.1
	H			50.9±0.3	14.7±0.1	14.1±0.1	14.1±0.1
14	**L**	L	-0.15	55.7±0.4	8.0±0.1	7.2±0.1	6.8±0.1
	H			50.5±0.3	15.4±0.1	14.7±0.1	14.7±0.1
4	**L**		0	55.6±0.4	8.2±0.1	7.4±0.1	6.9±0.1
	H			50.6±0.3	15.6±0.1	15.2±0.1	15.2±0.1
15	**L**		0.15	55.8±0.3	8.5±0.1	7.2±0.1	7.3±0.1
	H			50.4±0.3	15.8±0.1	14.9±0.1	15.0±0.1
16	**L**		0.30	55.6±0.3	14.3±0.1	5.8±0.1	5.7±0.1
	H			50.6±0.3	26.2±0.2	10.6±0.1	10.6±0.1

Unit: mmHg; C, concentric; S, shape; L, location; T, tapered; P, protruding; Mean ± Standard Error

Table 4.3: Comparison of flow rates between different nozzle designs

Case				Qlb	Qlpa	Qrpa	Qsvc	Qsh	CO	OD
1	**L**	β	0.24	0.66±0.01	0.26±0.01	0.26±0.01	0.48±0.01	0.04±0.03	1.16±0.02	3.11±0.27
	H			0.66±0.01	0.24±0.01	0.23±0.01	0.42±0.01	0.05±0.03	1.13±0.01	2.96±0.27
2	**L**		0.36	0.65±0.01	0.27±0.01	0.28±0.01	0.47±0.01	0.08±0.03	1.19±0.01	3.17±0.27
	H			0.65±0.01	0.25±0.01	0.25±0.01	0.42±0.01	0.08±0.03	1.15±0.01	2.99±0.27
3	**L**		0.48	0.65±0.01	0.30±0.01	0.30±0.01	0.46±0.01	0.14±0.03	1.23±0.01	3.20±0.27
	H			0.65±0.01	0.27±0.01	0.27±0.01	0.40±0.01	0.14±0.03	1.19±0.01	3.00±0.27
4	**L**		0.60	0.65±0.01	0.32±0.01	0.33±0.01	0.42±0.01	0.23±0.03	1.31±0.01	3.32±0.27
	H			0.64±0.01	0.31±0.01	0.31±0.01	0.39±0.01	0.23±0.03	1.26±0.01	3.05±0.27
5	**L**		0.72	0.65±0.01	0.35±0.01	0.35±0.01	0.42±0.01	0.28±0.03	1.35±0.01	3.35±0.27
	H			0.64±0.01	0.33±0.01	0.34±0.01	0.33±0.01	0.34±0.03	1.31±0.01	2.92±0.27
6	**L**		0.84	0.67±0.01	0.38±0.01	0.39±0.01	0.40±0.01	0.36±0.03	1.43±0.02	3.31±0.27
	H			0.66±0.01	0.36±0.01	0.37±0.01	0.33±0.01	0.40±0.03	1.39±0.01	3.04±0.27
7	**L**	θ	20°	0.64±0.01	0.31±0.01	0.32±0.01	0.42±0.01	0.21±0.03	1.27±0.01	3.15±0.27
	H			0.64±0.01	0.30±0.01	0.31±0.01	0.40±0.01	0.21±0.03	1.25±0.01	3.07±0.27
8	**L**		30°	0.67±0.01	0.33±0.01	0.34±0.01	0.44±0.01	0.23±0.03	1.34±0.01	3.35±0.27
	H			0.66±0.01	0.32±0.01	0.33±0.01	0.41±0.01	0.24±0.03	1.31±0.01	3.20±0.27
4	**L**		40°	0.65±0.01	0.32±0.01	0.33±0.01	0.42±0.01	0.23±0.03	1.31±0.01	3.32±0.27
	H			0.64±0.01	0.31±0.01	0.31±0.01	0.39±0.01	0.23±0.03	1.26±0.01	3.05±0.27
9	**L**		50°	0.65±0.01	0.31±0.01	0.31±001	0.41±0.01	0.21±0.03	1.27±0.01	3.14±0.27
	H			0.65±0.01	0.30±0.01	0.30±0.01	0.38±0.01	0.22±0.03	1.25±0.01	3.03±0.27
10	**L**		60°	0.64±0.01	0.30±0.01	0.30±0.01	0.40±0.01	0.20±0.03	1.24±0.01	3.06±0.27
	H			0.65±0.01	0.29±0.01	0.29±0.01	0.38±0.01	0.20±0.03	1.23±0.01	3.00±0.27
11	**L**	S	T	0.64±0.01	0.32±0.01	0.32±0.01	0.42±0.01	0.22±0.03	1.28±0.01	3.16±0.27
	H			0.65±0.01	0.31±0.01	0.30±0.01	0.39±0.01	0.22±0.03	1.26±0.01	3.07±0.27
4	**L**		C	0.65±0.01	0.32±0.01	0.33±0.01	0.42±0.01	0.23±0.03	1.31±0.01	3.32±0.27
	H			0.64±0.01	0.31±0.01	0.31±0.01	0.39±0.01	0.23±0.03	1.26±0.01	3.05±0.27
12	**L**		P	0.64±0.01	0.33±0.01	0.32±0.01	0.41±0.01	0.24±0.03	1.29±0.01	3.14±0.27
	H			0.65±0.01	0.32±0.01	0.30±0.01	0.39±0.01	0.23±0.03	1.27±0.01	3.08±0.27
13	**L**		Li	0.66±0.01	0.32±0.01	0.32±0.01	0.46±0.01	0.18±0.03	1.30±0.01	3.34±0.27
	H			0.67±0.01	0.28±0.01	0.29±0.01	0.40±0.01	0.18±0.03	1.25±0.01	3.12±0.27
14	**L**	L	-0.15	0.65±0.01	0.32±0.01	0.32±0.01	0.42±0.01	0.22±0.03	1.29±0.01	3.19±0.27
	H			0.65±0.01	0.31±0.01	0.30±0.01	0.39±0.01	0.22±0.03	1.26±0.01	3.07±0.27
4	**L**		0	0.65±0.01	0.32±0.01	0.33±0.01	0.42±0.01	0.23±0.03	1.31±0.01	3.32±0.27
	H			0.64±0.01	0.31±0.01	0.31±0.01	0.39±0.01	0.23±0.03	1.26±0.01	3.05±0.27
15	**L**		15	0.65±0.01	0.33±0.01	0.33±0.01	0.42±0.01	0.24±0.03	1.31±0.01	3.21±0.27
	H			0.66±0.01	0.32±0.01	0.31±0.01	0.39±0.01	0.24±0.03	1.29±0.01	3.12±0.27
16	**L**		30	0.65±0.01	0.26±0.01	0.27±0.01	0.26±0.01	0.27±0.03	1.18±0.01	2.59±0.27
	H			0.66±0.01	0.25±0.01	0.26±0.01	0.24±0.01	0.27±0.03	1.17±0.01	2.53±0.27

Unit: LPM; C, concentric; S, shape; L, location; Li, ligaclip; T, tapered; P, protruding; Mean ± Standard Error.

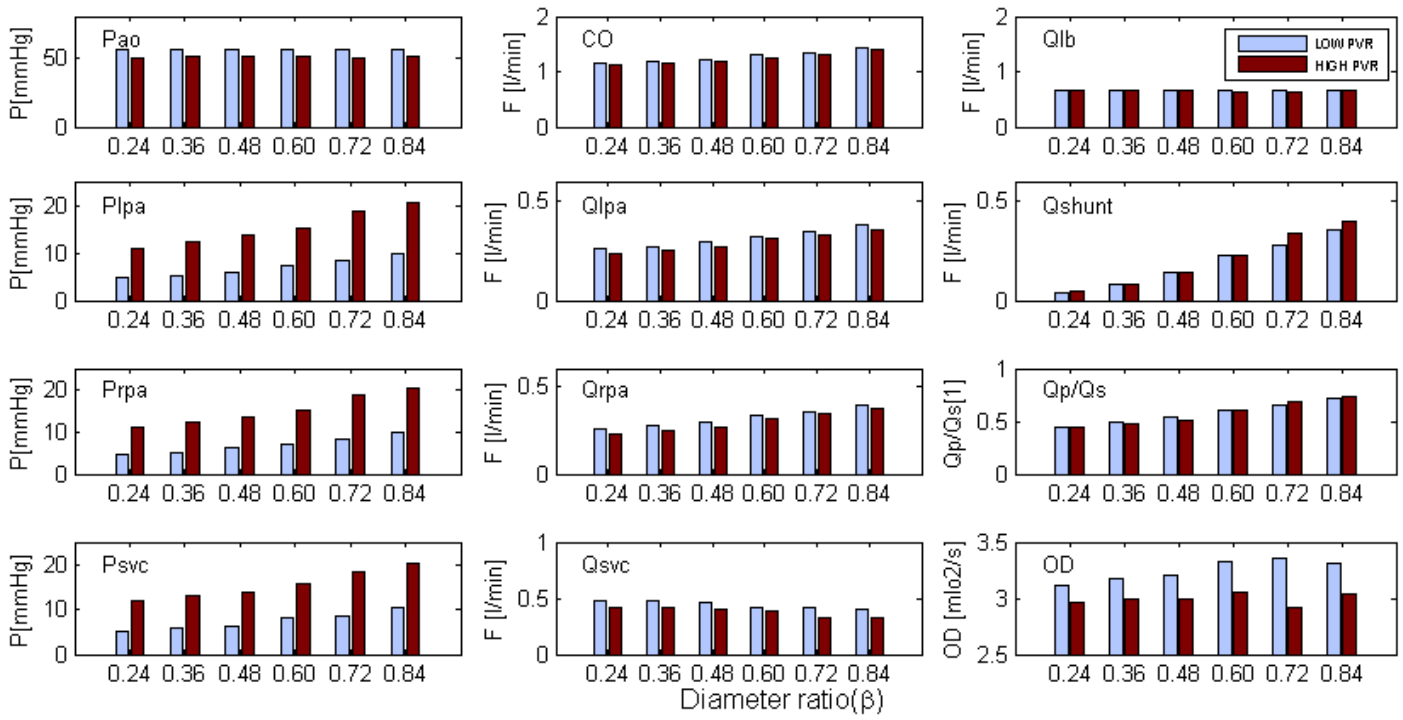

Figure 4.3: Experimental value comparisons of mean flow and pressure for the ABG circulation at PVR=2.3 WU (Low) and PVR=7.0WU (High) with different β; F, Flow; lb, lower body; lpa, left pulmonary artery; rpa, right pulmonary artery; SVC, super vena cava; OD, oxygen delivery; P, pressure, PVR, pulmonary vascular resistance

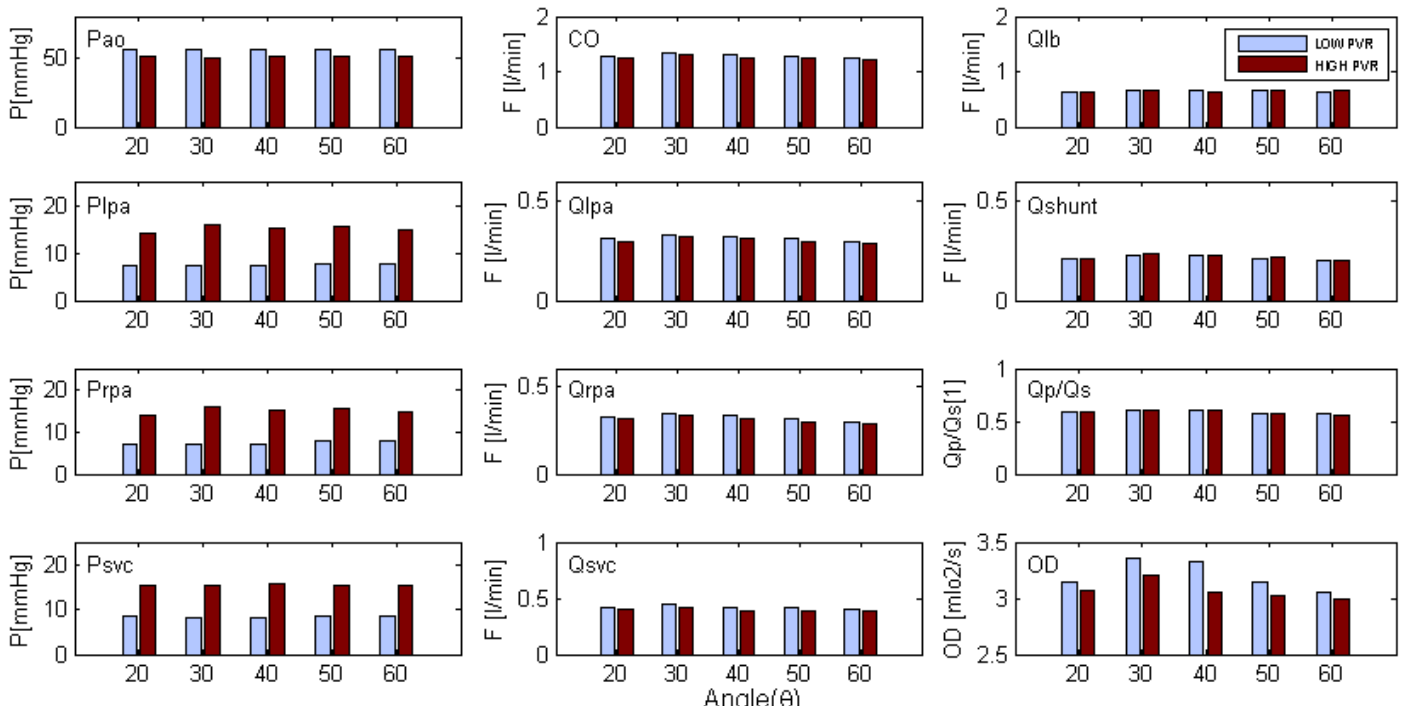

Figure 4.4: Experimental value comparisons of mean flow and pressure for the ABG circulation at PVR=2.3WU-m^2 WU (Low) and PVR=7.0 WU-m^2 (High) with different angle θ; F, Flow; lb, lower body; lpa, left pulmonary artery; rpa, right pulmonary artery; SVC, super vena cava; OD, oxygen delivery; P, pressure, PVR, pulmonary vascular resistance.

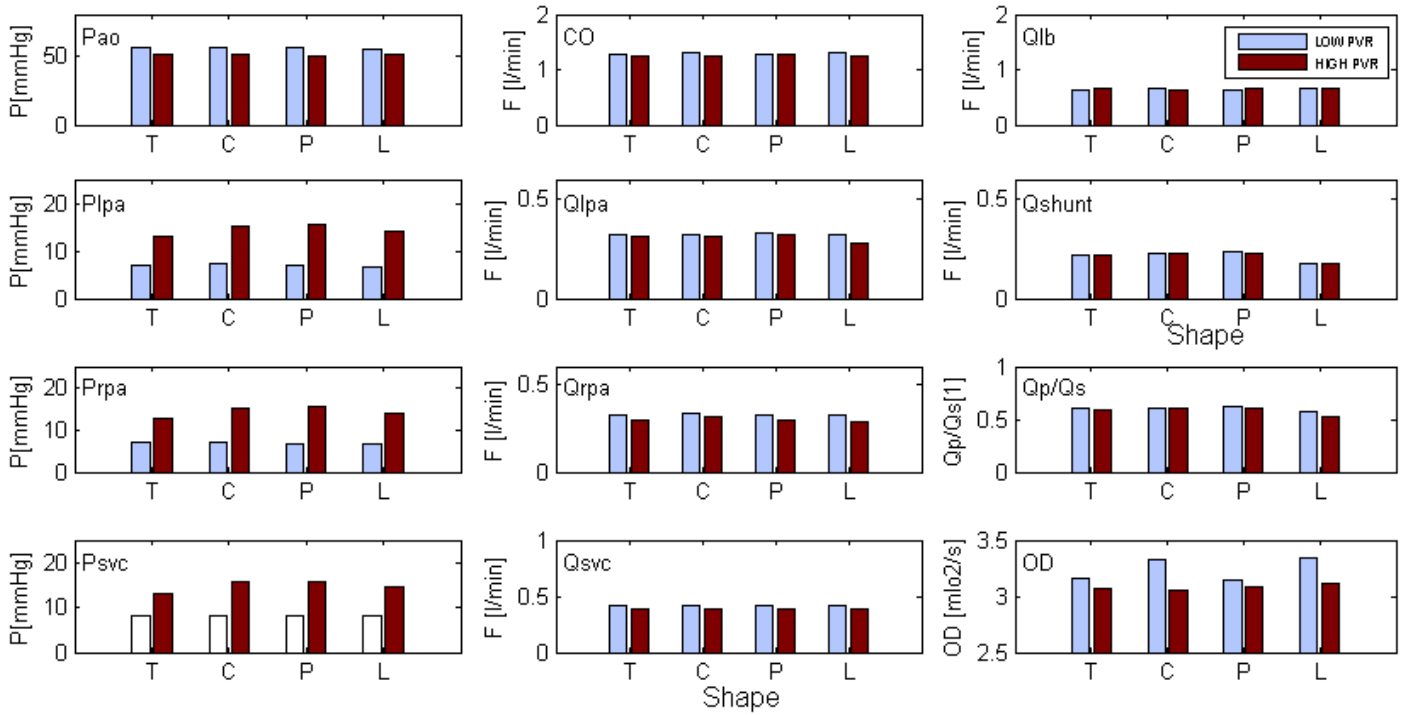

Figure 4.5: Experimental value comparisons of mean flow and pressure for the ABG circulation at low PVR and high PVR with different shapes; C, Concentric; F, Flow; L, ligaclip; lb, lower body; lpa, left pulmonary artery; rpa, right pulmonary artery; SVC, super vena cava; OD, oxygen delivery; P(y axis), pressure; P, protruded; PVR, pulmonary vascular resistance; T, tapered.

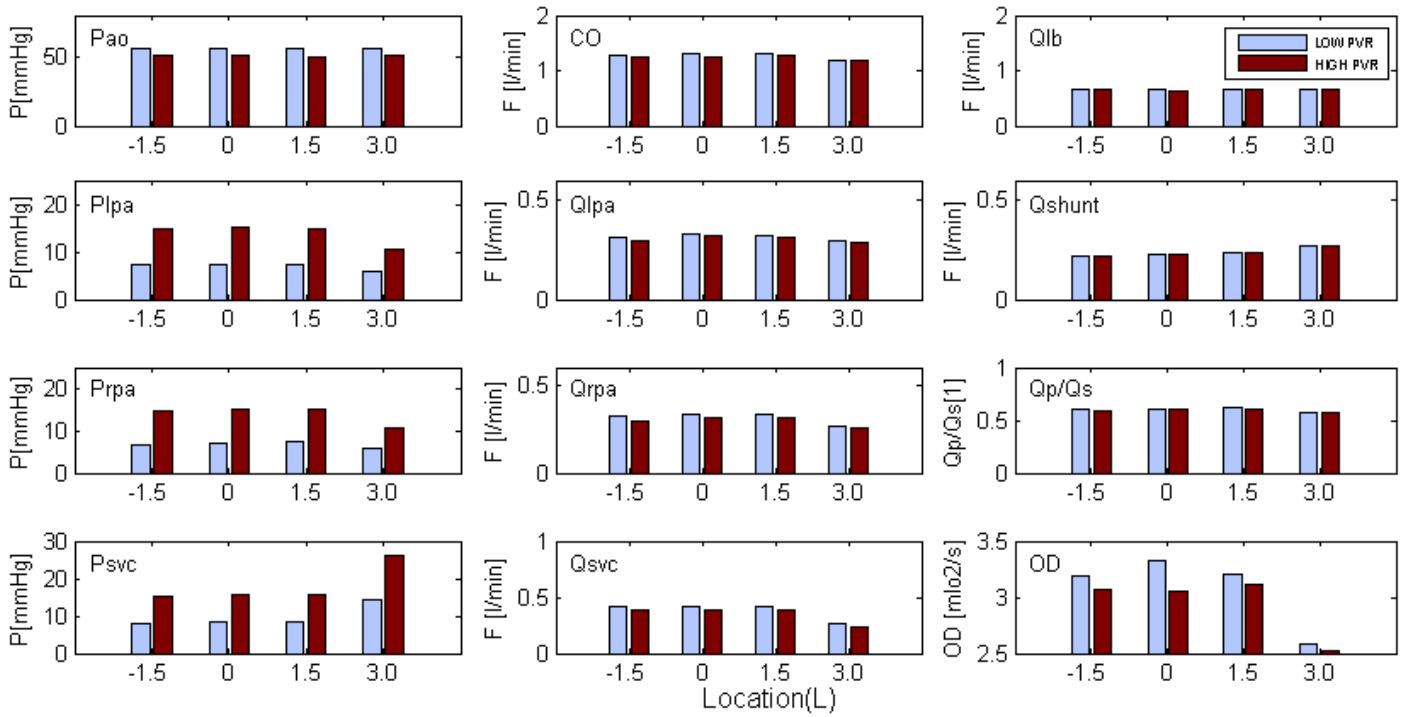

Figure 4.6: Experimental value comparisons of mean flow and pressure for the ABG circulation at PVR=2.3 WU-m^2 (Low) and PVR=7WU-m^2 (High) with different L (location); F, Flow; lb, lower body; lpa, left pulmonary artery; rpa, right pulmonary artery; SVC, super vena cava; OD, oxygen delivery; P, pressure, PVR, pulmonary vascular resistance.

Discussion

As discussed in the previous chapter, an ejector pump effect can be created within the ABG circulation but the effect is mild.

In this study, there was no nozzle that produced a better ejector than another. The study provided useful information on the nozzle design. A nozzle to shunt diameter ratio around 0.60 and L = 0 seems to provide the best balance of improved pulmonary blood flow, oxygen delivery, and SVC pressure. A shunt angle between 30^o and 40^o is recommended. A nozzle design protruding into the SVC and aligned with tis axis showed no improvement over a nozzle contained internal to the shunt and actually increased SVC pressure due to the blockage by its pressure in the SVC flow path. A future goal must be to reduce this SVC pressure increase, if possible.

CHAPTER FIVE

THE ABG AORTIC COARCTATION STUDY

The ABG circulation has been assessed numerically and experimentally as a surgical option for Stage 1 single ventricle heart disease palliation under normal conditions (normal PVR and no coarctation). In this section, the ABG circulation performance and feasibility in the presence of aortic coarctation is studied.

The goal of this chapter is to study the effects of aortic coarctation on the global hemodynamics of the Assisted Bidirectional Glenn circulation.

Methods

The *in vitro* multi-scale system of the ABG circulation was used to study coarctation effects on the ABG circulation. The tests use the same generic patient LPN parameters and 3D anastomosis models of ABG circulation presented in the previous studies. Coarctation, defined as the narrowing of the aortic isthmus, was introduced as a narrowing of the aorta just distal to the isthmus. Severity of coarctation (details in the test sections) was progressively increased to assess effects.

Experimental Setup

In these tests, the mean aortic pressure was adjusted in order to maintain a constant cardiac output at the same baseline value while coarctation was varied. Tests

were run using a PVR set to a value of 2.3 WU-m^2 and against at 7.0 WU-m^2. The parametric values of the LPN model were set to the same values as reported in Table 2.1.

Test Sections

The 3-D test section of the aortic arch as used with the ABG circulation (Ligaclip shaped nozzle, β=0.7, $\theta = 40^o$) was used as the base geometry in these tests. The choice was based on the fact that the ligaclip nozzle design produced high systemic oxygen delivery. A coarctation was introduced at the arch isthmus (see Figure 5.1, coarctation location is the region within the circle). This consisted of a smooth circular notch creating a local minimum in the aortic diameter, as shown in Figure 5.1. Coarctation severity was adjusted by manipulating the local minimum diameter. Severity is measured through the coarctation index (CoI), which is defined as the ratio of the local minimum (coarctation) diameter to the diameter of the descending aorta at diaphragm [94]. In the previous section, the aortic arch tested was free of coarctation. For the coarctation study, CoI was varied between 0.3 (very severe) to 0.9 (very mild), as indicated in Figure 5.1. A CoI = 1.0 indicates no coarctation.

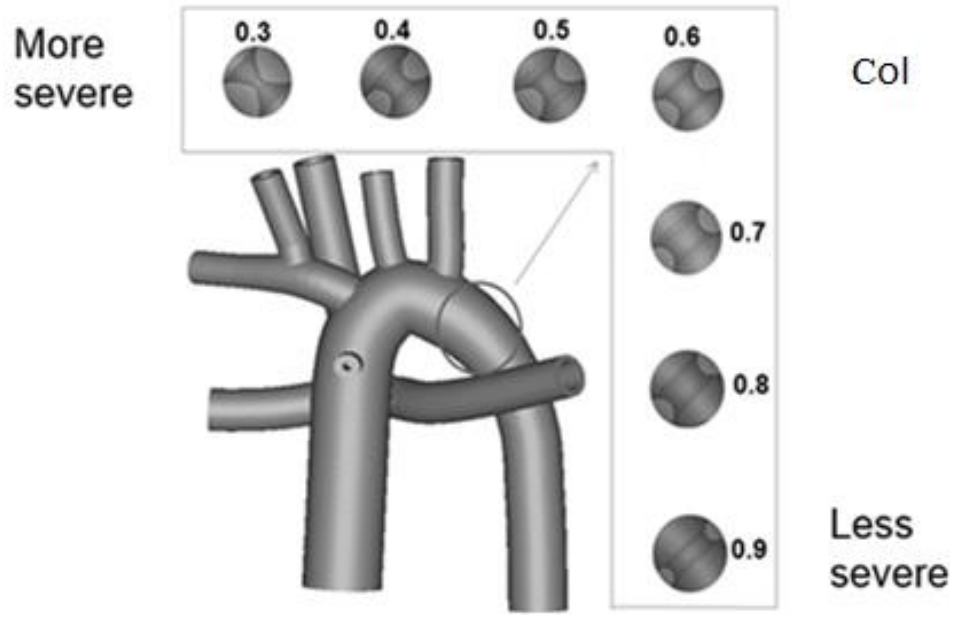

Figure 5.1: The 3D geometrical model used showing different coarctation indices (CoI).

Global measurements

Cardiact output was held constant across these tests. Parameters measured were: pressure and flow rate at left/right pulmonary artery (LPA/RPA) and superior vena cava (SVC), lower body flow rate, and ascending aorta pressure. For the aortic coarctation study, the pressure differential across the coarctation was also measured by wall pressure measurements. Systemic oxygen delivery, lower body and upper body oxygen delivery were calculated. The details of the oxygen delivery calculation are given in Appendix H.

Results

The test results of the systems-level mean pressures and flow rates as functions of CoI and for two values of PVR are given in Figure 5.2 and Figure 5.3 along with regression lines, respectively. For either value of PVR, mean aortic pressure (MAP)

remained bounded between 55.0 to 60.0 mmHg for $0.4 \leq \text{CoI} \leq 0.9$, a range that is not clinically significant (a noticeable effect on daily life). For CoI < 0.4, MAP increased rapidly with CoI.

For a PVR value of 7.0 WU-m^2, the left pulmonary artery pressures (upper right, Figure 5.2) remained nearly constant (14.5 mmHg) for $0.5 \leq \text{CoI} \leq 0.9$. For CoI < 0.4, the pressure values increased rapidly towards 18.0 mmHg as CoI decreased to 0.3. For PVR value of 2.3 WU-m^2, the left pulmonary artery pressures (upper right, Figure 5.2) remained nearly constant (7.5 mmHg) for $0.5 \leq \text{CoI} \leq 0.9$. For CoI < 0.5, the pressure values increased rapidly towards 10.0 mmHg as CoI decreased to 0.3. As the LPN values for right and left pulmonary arteries were the same, both RPA and LPA showed the same trend.

The pressure within the SVC branch behaved much the same as the pressure within the pulmonary arteries did. For a PVR value of 7.0 WU-m^2, the SVC pressures (lower right, Figure 5.2) remained nearly constant (15.0 mmHg) for $0.5 \leq \text{CoI} \leq 0.9$. For CoI < 0.5, the SVC pressure value increased rapidly towards 20.0 mmHg as CoI decreased to 0.3. For a PVR value of 2.3 WU-m^2, the SVC pressure (lower right, Figure 5.2) remained nearly constant (9.0 mmHg) for $0.5 \leq \text{CoI} \leq 0.9$. For CoI < 0.5, the pressure values increased rapidly towards 11.0 mmHg.

The LPA and RPA flow rates (Figure 5.3) responded similarly. For a PVR value of 2.3 WU-m^2, the left (or right) pulmonary artery flow was nearly constant between 0.31 LPM and 0.32 LPM for $0.5 \leq \text{CoI} \leq 0.9$. For $\text{CoI} \leq 0.5$, the pulmonary flow increased rapidly with CoI. For a PVR value of 7.0 WU-m^2, the pulmonary artery flow

was nearly constant at 0.28 LPM and 0.29 LPM for $0.5 \leq \text{CoI} \leq 0.9$. For $\text{CoI} \leq 0.5$, pulmonary flow increased rapidly.

For a PVR value of 2.3 WU-m^2, the SVC flow rate (middle right, Figure 5.3) was nearly constant between 0.45 LPM and 0.46 LPM for $0.5 \leq \text{CoI} \leq 0.9$. For $\text{CoI} < 0.5$, SVC flow rate increased rapidly with CoI, at CoI = 0.3, reaching a 38% percent increase compared with the value for $0.5 \leq \text{CoI} \leq 0.9$. For a PVR value of 7.0 WU-m^2, the SVC flow rate (middle right, Figure 5.3) was nearly constant between 0.40 LPM and 0.41 LPM for $0.5 \leq \text{CoI} \leq 0.9$. Again, for $\text{CoI} < 0.5$, the SVC flow rate increased rapidly towards 0.58 LPM at CoI =0.3, a 45% percent increase.

For either value of PVR, the lower body flow rate (lower right, Figure 5.3) remained nearly constant between 0.61 ~ 0.63 LPM for $0.5 \leq \text{CoI} \leq 0.9$. Lower body flow rate decreased rapidly with $\text{CoI} < 0.5$, due to the extra resistance introduced by the coarctation. For CoI = 0.3, the lower body flow rate dropped to 0.40 LPM, a 34% percent decrease.

Due to limitation of the measuring, the shunt flow rate could not be measured directly. Its value was calculated by the law of mass conservation (Assuming incompressible flow), then

$$Q_{shunt} = Q_{SVC} - Q_{LPA} - Q_{RPA} \qquad (5\text{–}1)$$

The calculated results are shown in Figure 5.3, lower left. For either value of PVR, the shunt flow remained nearly constant at 0.20 LPM for $0.5 \leq \text{CoI} \leq 0.9$ and increased to 0.28 LPM as CoI decreased to 0.3.

Based on these measurements, aortic coarctation did not produce clinically significant changes on the hemodynamics of the ABG circulation for $0.5 \leq \text{CoI} \leq 0.9$. For CoI < 0.5, shunt flow rate increased and pulmonary and caval blood flows and pressures all increased. The systemic oxygen delivery (OD) calculation results are shown in Figure 5.4. The OD value was remained nearly constant at around 3.3 ml_{o_2} / s and 3.0 ml_{o_2} / s for PVR values of 2.3 WU-m^2 and 7.0 WU-m^2, respectively. There were no significant changes in the systemic oxygen delivery as CoI became severe.

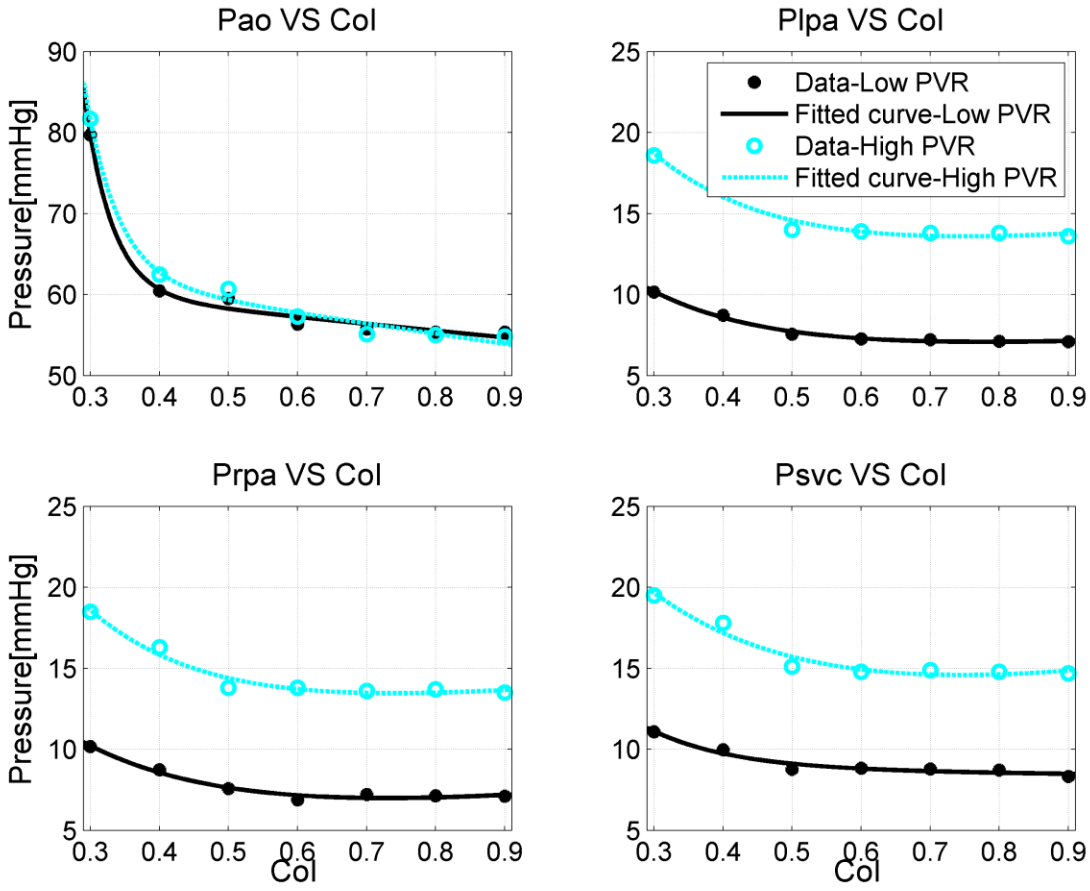

Figure 5.2: Measured systemic mean pressure values versus CoI. ao, aorta; CoI, index of coarctation. lpa, left pulmonary artery; rpa, right pulmonary artery, P, pressure; svc, superior vena cava. PVR, pulmonary vascular resistance. Low PVR, 2.3WU-m^2 ; high PVR, 7.0 WU-m^2

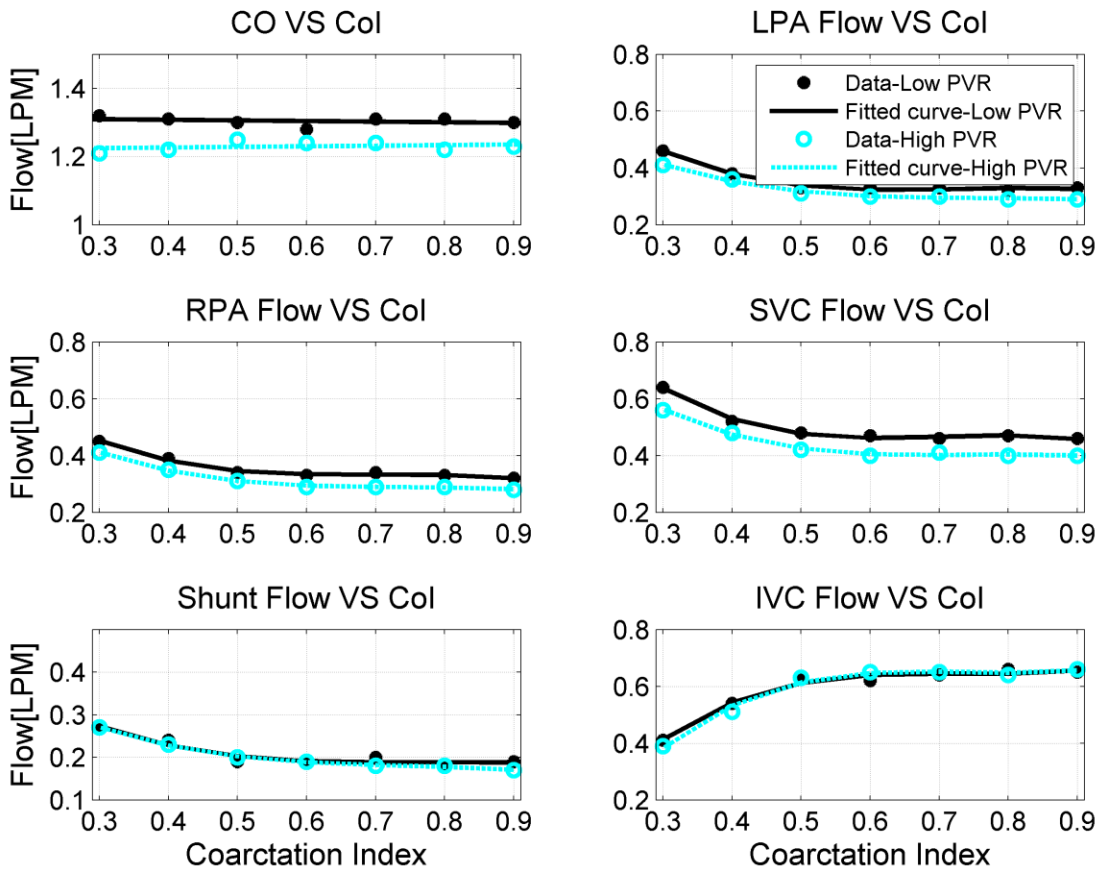

Figure 5.3: Systemic mean flow values versus CoI. CO, Cardiac output; CoI, index of coarctation; IVC, inferior vena cava; LPA, left pulmonary artery, RPA, right pulmonary artery; right pulmonary artery, SVC, superior vena cava. Low PVR = 2.3 WU-m^2 , High PVR = 7.0 WU-m^2

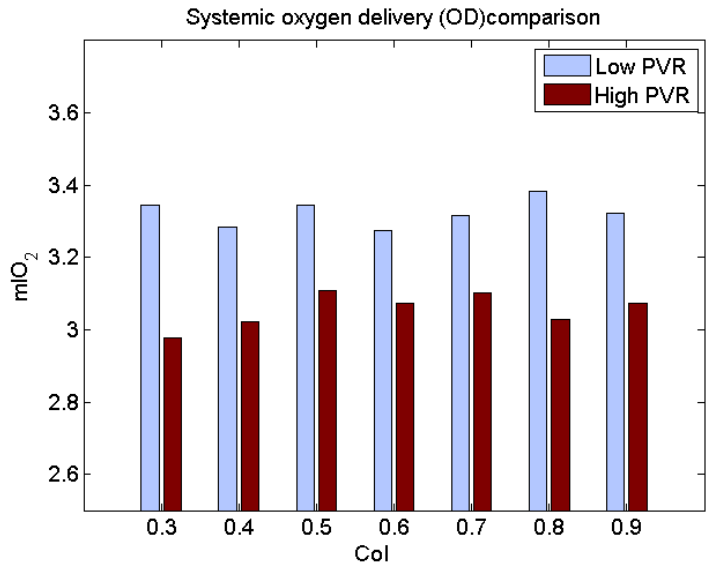

Figure 5.4: Systemic OD values versus CoI. CoI, index of coarctation; OD, oxygen delivery; PVR, pulmonary vascular resistance. Low PVR = 2.3 WU-m^2 , High PVR = 7.0 WU-m^2

Discussion

This study examined the systems-level effects of coarctation on the ABG circulation. Aortic anatomies with mild to severe aortic coarctation were examined. For all measured parameters except OD, the effects of coarctation were not noticeable above CoI > 0.5. For CoI less than 0.5, the changes in parameter values were rapid, suggesting a potential need for clinical intervention.

With constant cardiac output (CO), an increase in coarctation did not produce a decrease in the systemic oxygen delivery, as shown in Figure 5.4. To better understand the aortic coarctation effect on oxygen delivery distribution in the ABG circulation, consider that the upper body oxygen delivery OD_{SVC} and lower body oxygen delivery (see Appendix H for derivations) were calculated by:

$$OD_{LB} = Q_{LB} \cdot C_p - r\frac{Q_{LB}}{Q_P}V_{o_2} \qquad (5\text{-}2)$$

$$OD_{SVC} = Q_{SVC} \cdot C_p - r\frac{Q_{SVC}}{Q_P}V_{o_2} \qquad (5\text{-}3)$$

where C_P and V_{O_2} are the pulmonary oxygen concentration and oxygen consumption rate, respectively. The calculated oxygen delivery for the upper body and the lower body are given in Figure 5.5 and Figure 5.6, respectively. Under severe coarctation (CoI = 0.3), the upper body oxygen delivery (OD_{SVC}) increased towards 2.0 ml_{O_2} / ml due to the increased SVC blood flow rate. However the lower body oxygen delivery (OD_{LB}) decreased towards 1.3 ml_{O_2} / ml due to a large decrease in the lower body flow rate. This presented a problematic situation in the distribution of oxygen. Low OD_{LB} will lead to insufficient oxygen content in the lower body, which could lead to ulceration and other oxygen insufficiency related diseases. So which systemic OD did not appear affected by severe CoI (Fig 5.4), a closer look at the distribution of systemic OD shows measureable changes as CoI < 0.5, consistent with other measured parameters. The ability to examine systems-level effects in detail is an advantage of a multi-scale model.

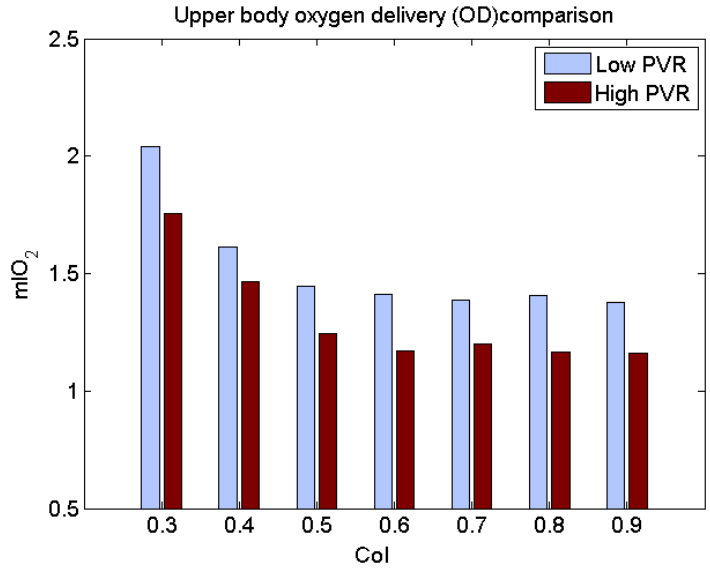

Figure 5.5: Calculated upper body oxygen delivery values versus CoI. CoI, index of coarctation; OD, oxygen delivery; PVR, pulmonary vascular resistance.

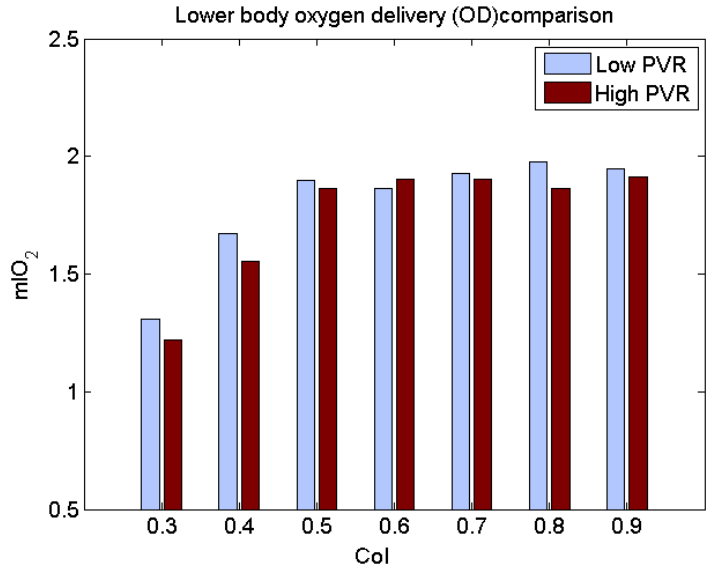

Figure 5.6: Calculated lower body oxygen delivery values versus CoI. CoI, index of coarctation; OD, oxygen delivery; PVR, pulmonary vascular resistance.

Pressure Drop Analysis

The pressure drop across the coarctation is an important parameter. The measured pressure drop across the coarctation of the ABG circulation for the PVR value of 2.3 WU-m^2 and 7.0 WU-m^2 is presented in Figure 5.7. The pressure drop increased as the CoI decreased. The pressure drop increased measurably for CoI < 0.5. The resulting Figure 5.7 matched well to the results reported by Hang [48] in an aortic coarctation study of the Norwood circulation using an similar *in vitro* test loop. Similar results of pressure drop across the coarctation of a real Norwood patient were also reported by Biglino et al. [67]. Although the ABG circulation has a different physiology structure compared with the Norwood circulation, the structural difference does not have an influence on the lower body branch. Clinically, a final pressure drop across the aortic arc coarctation of less than 10.0 mmHg is considered a success [47] in a coarctation intervention. From this study, at CoI = 0.5, the pressure drop across the coarctation was around 10.0 mmHg. Accordingly, a CoI = 0.5 suggests a need for clinical intervention.

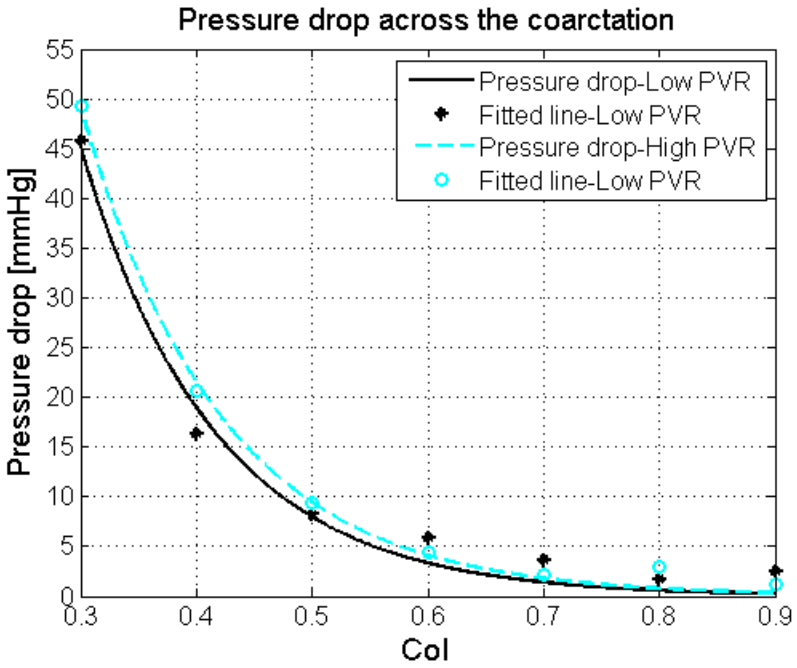

Figure 5.7: Measured wall pressure drop across coarctation versus CoI. CoI, index of coarctation.

Measured results of the flow distribution showed that the inferior vena cava flow (Q_{IVC}) was highly sensitive to coarctation. This finding matches well with the observations made by Biglino et al.[67]. The variation of lower body flow rate influenced another important parameter: the ratio of pulmonary flow rate to systemic flow rate ratio (Qp/Qs). The measured Qp/Qs as a function of CoI is shown in Figure 5.8 for either value of PVR. As CoI decreased from 0.9 to 0.3, Qp/Qs increased from 0.58 to 0.88. The reason was that the coarctation decreased the lower body flow rate and increased the pulmonary flow rate.

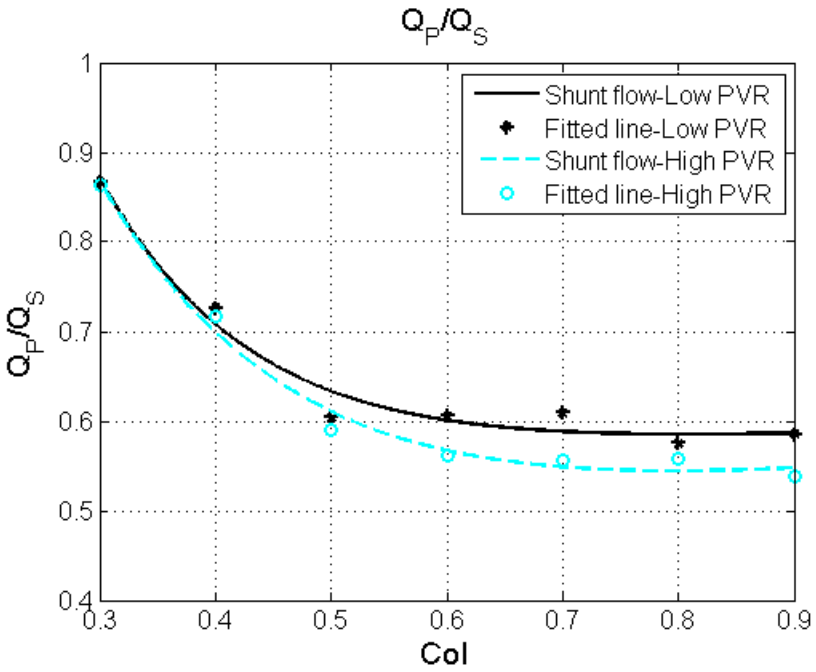

Figure 5.8: Calculated Qp/Qs ratio versus CoI. CoI, index of coarctation; Qp, pulmonary flow rate; Qs, systemic flow rate.

The CO was held constant in this coarctation study. Biglino et al. [67] and Hang [48] used the constant cardiac output as the control input parameter, while Corsini et al. [95] used body surface area (BSA), PVR and SVR as the control input parameters for a CFD coarctation study. Several observations in Corsini et al. [95] are different from the findings in this study. For example, they reported that the CO and systemic oxygen delivery decreased (almost constant in this study) as CoI decreased. However, this current study found OD to be nearly constant with varying CoI. The question of how to choose the control input for a single ventricular circulation modeling to simulate the natural adaption of single ventricular circulation to physiological variations needs more investigation.

One limitation of this study is that only one simple aortic coarctation morphology was tested. Previous studies found that coarcation morphologies had effects on the hemodynamics of the Norwood circulations [95, 67, 48]. Future studies should investigate CoA effects on patients with different coarctation morphologies.

CHAPTER SIX

RESPIRATION EFFECTS ON STAGE 2 CIRCULATION

In this chapter, a respiration model is added to the *in vitro* Stage 2 circulation model previous described. The system is verified and validated by comparing the measured hemodynamic parameters with clinical data or analytical predictions. The influence of respiration on Stage 2 circulation hemodynamics is discussed.

Method

Experimental Setup

A respiration model previously validated by Vukicevic [74] is utilized in the Stage 2 MCS system. The schematic of the system and the photograph of the experimental setup used are shown in Figure 6.1 and Figure 6.2, respectively.

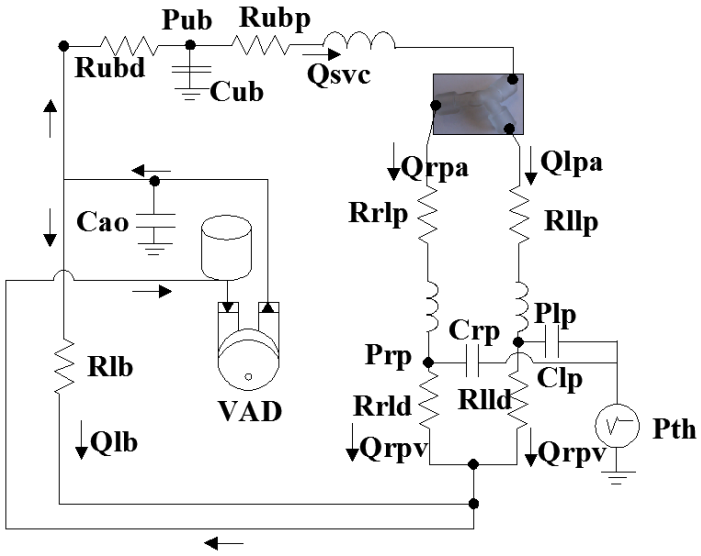

Figure 6.1: Reduced lumped domain network model used for the Stage 2 mock circulatory system with respiration. BCPA, Bidirectional Cavopulmonary Anastomosis; C, compliance; lb, lower body; lld, left lung distal; llp, left lung proximal; lp, left lung; lpa, , left pulmonary artery; lpv, left pulmonary vein; P, pressure; Q, flow rate; R, resistance; rld, right lung distal; rlp, right lung proximal; rp, right pulmonary; rpa, right pulmonary artery; rpv, right pulmonary vein; svc, superior vena cava; ub, upper body; ubd, upper body distal; ubp, upper body proximal; VAD, ventricle assisted device.

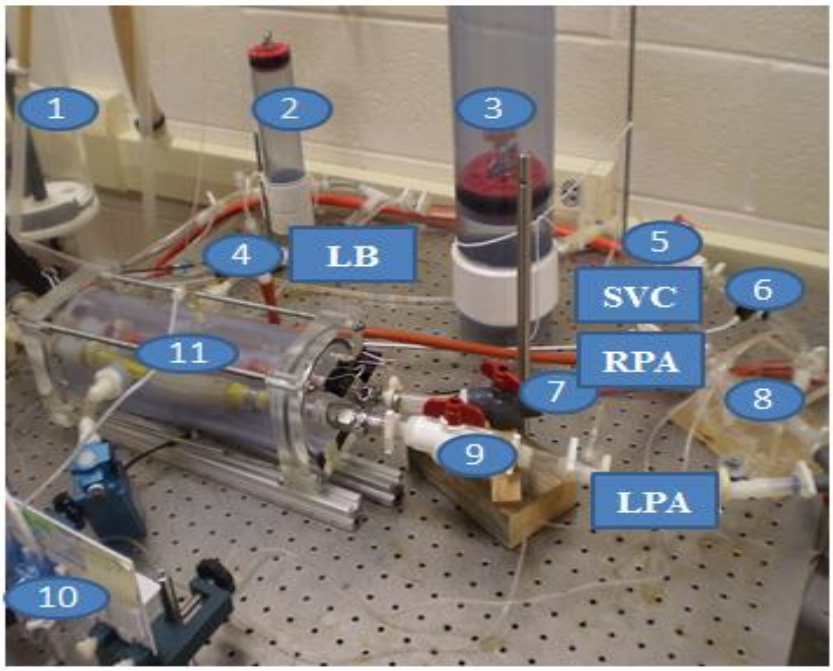

Figure 6.2: Photograph of Glenn circulation MCS: 1, Head tank; 2, Aorta compliance element; 3, SVC compliance element; 4, Berlin heart VAD; 5, SVC resistance element; 6, SVC flow meter; 7 and 9, RPA and LPA resistance elements; 8, Test section; 10, pressure transducers; 11, pulmonary compliance element. LB, lower body; LPA, left pulmonary artery; RPA, right pulmonary artery; SVC, superior vena cava.

Pulmonary Compliance Elements

The pulmonary compliance elements were made of two elastic tubes; each tube was attached inline to a separate pulmonary artery branch, and both housed within a single sealed air chamber, acting as the thoracic cavity. The elastic tubes were adapted from pediatric respiration balloons. A rigid tube placed over each elastic tube restricts expansion and was the means to adjust its compliance. Figure 6.3 shows another pulmonary compliance chamber similar to the one used here. The method to tune and calibrate the compliance value of the pulmonary compliance is given in Appendix C.

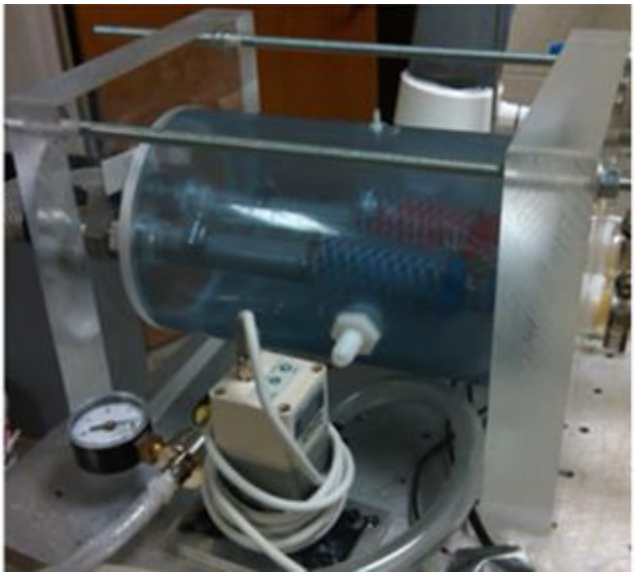

Figure 6.3: Photograph of the pulmonary compliance used in the lab.

The Respiration Model

The act of breathing creates a vacuum pressure in the thoracic cavity during inspiration, relaxing to slightly negative pressure during expiration and rest. Due to the lack of a valve in the Glenn anastomosis in single ventricle patients, respiration affects the motion of blood flow returning through the pulmonary circulation towards the heart. The respiratory amplitude of thoracic cavity vacuum is dependent upon the age. Under resting conditions, it varies from a nominal amplitude of 2 mmHg for an infant to 5 mmHg for an adult [96]. A magnitude ranging from -2 to -6 mmHg is applied in the Stage 2 circulation MCS.

Time-dependent respiration pressure was produced using a programmable proportional pneumatic regulator (ITV1009, SMC Corp, Noblesville, Inc.) and a solenoid valve (Model: 225B-111CAAA, MAC Valve, Dundee, MI, USA) responding to a

computer controlled voltage waveform to control alternating vacuum pressure and atmospheric pressure. The schematic of the system is given in Figure 6.4. The control equation simulated was

$$P_{th} = \begin{cases} A_{th}\left(1-\cos\left(\dfrac{2\pi t}{t_a}\right)\right)+P_{rest} & t < t_a \\ P_{rest} & t_a \le t < t_R \end{cases} \qquad (6-1)$$

Here, A_{th} is the amplitude of −4 mm Hg for the thoracic pressures. The ratio of the activation function period, t_a, to respiration cycle period, t_r, was 0.375 in all tests. Unless otherwise stated, the respiration rate was 30 bpm (t_r = 2.0 s). P_{rest} was set to atmospheric pressure. The control signal of pressure waveform and physical realization within the pulmonary compliance chamber is shown in Figure 6.5.

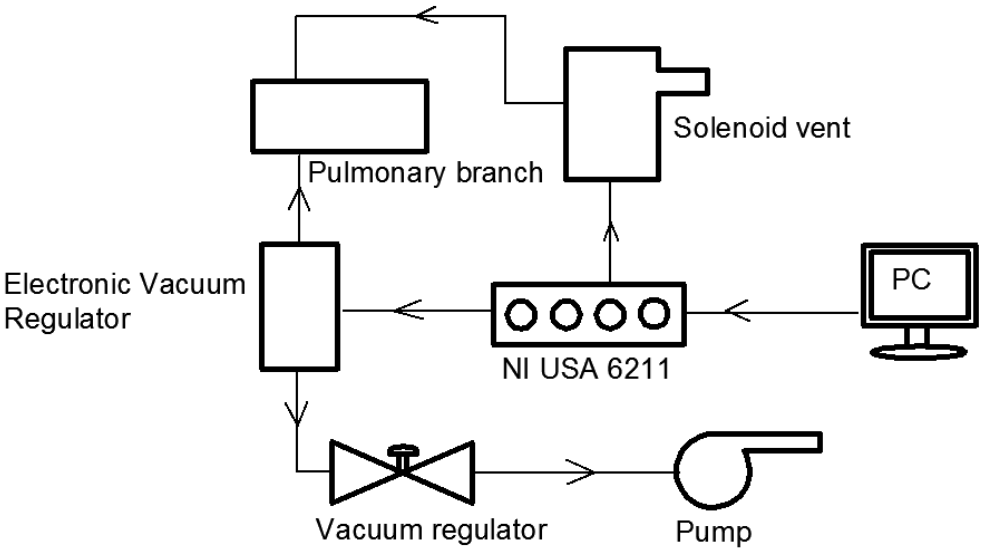

Figure 6.4: Schematic of the respiration system.

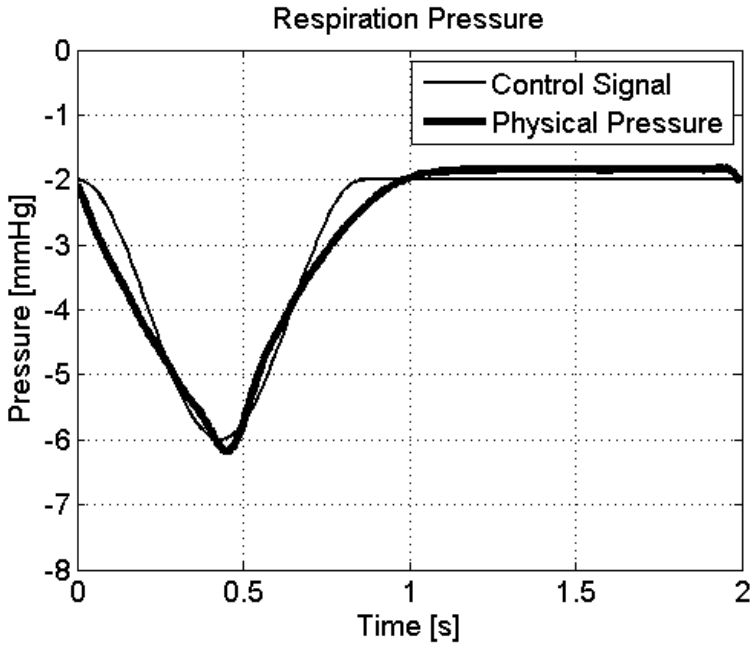

Figure 6.5: Control signal and physical realization of time dependent respiration amplitude.

Patient Selection and LPN Parameters

No previous *in vitro* MCS study has been reported for a Stage 2 Glenn circulation with respiration. In this research, two Stage 2 cases were studied, including two different surgical time points (TP4: time point 4, which corresponds to just after the Stage 2 surgery; TP5: time point 5, which corresponds to just before the Stage 3 Fontan surgery) for the patient designated here as UM2 (UM, University of Michigan), where the acronym refers to the patient's clinical center and the numerical value identifies the patient's record as discussed in Chapter 2. The specific parametric values used are listed in Table 2.2 and Table 6.1.

Table 6.1: LP elemental values for Stage 2 respiration study

Parameters	Unit	UM2_TP4
Pao	mmHg	53
Pat	mmHg	2.5
Rlb	mmHg.s/ml	6.67±0.21
Rubd	mmHg.s/ml	3.24±0.08
Rubp	mmHg.s/ml	0.16±0.01
Cup	ml/mmHg	0.24±0.01
Rrlp	mmHg.s/ml	0.49±0.02
Rrld	mmHg.s/ml	1.21±0.06
Crl	ml/mmHg	0.63±0.04
Rllp	mmHg.s/ml	0.11±0.01
Rlld	mmHg.s/ml	2.80±0.08
Cll	ml/mmHg	0.36±0.04
Cao	ml/mmHg	0.20±0.01
HB	times/min	120
RR	times/min	30

C, Compliance; LB, Lower body; LL, Left lung; LLD, Left lung distal; LLP, Left Lung Proximal; LP, Lumped parameter; LPN, Lumped parameter network; R, Resistance; RL, Right lung; RLD，Right lung distal; RLP, Right lung proximal; RR, Respiration rate; UP, Upper body; UPD, Upper body distal; UPP, Upper body proximal. TP4, Time point 4, just post Glenn surgery;

Results

Case UM2_TP4: Verification of the System

This case presents a verification of the Stage 2 model with respiration by comparing the experimental results with analytical predictions for patient UM2 at time point 4. The respiration frequency was 30 breaths/min and the heart rate was 120 beats/min.

Experimentally measured flow rates, pressures and corresponding analytical results over one respiration period are shown in Figure 6.6 – 6.7. The agreement between experimental and analytical pressure and flow rate is reasonable with satisfactory amplitude and phase matching ($0.60 < R^2 < 0.96$, $p > 0.05$).

The experimental SVC flow rate matched well with the analytical predictions with satisfactory amplitude and phase matching ($R^2 = 0.89$, $p > 0.05$). The calculated σ was 6%, demonstrating the model is a reasonable match with the analytical model.

The measured RPA flow rate matched well with the analytical predictions with satisfactory amplitude and phase matching ($R^2 = 0.64$, $p > 0.05$). The calculated σ was < 5%, demonstrating reasonable agreement.

The LPA flow rate signal showed more pulsatility in response to both heartbeat and respiration, because the left lung was set to a smaller proximal resistance value, matching clinical measurement. The measured LPA flow rate matched well with the analytical predictions, with satisfactory amplitude and phase matching ($R^2 = 0.84$, $p > 0.05$). The calculated σ of 10% shows reasonable agreement, and the rounding of relatively sharp peaks seen in the analytical reference probably resulted from inertance in the MCS.

The experimental lower body flow ranged from 0.40 to 0.58 LPM, which is smaller than the analytical range 0.32 to 0.60 LPM. However, the lower body flow rate was only controlled by a single resistance element, and its time based behavior was not intended to be modeled, just its mean value. So the mismatch between the two models of the time-based lower body flow rate is acceptable.

Three pressures pressure waveforms were investigated: (1) aorta pressure, the input signal to the system; (2) bidirectional cava pulmonary anastomosis (BCPA) pressure; and (3) respiration pressure.

As seen in Figure 6.7, measured pulsatile aortic pressure matched well with the analytical one with satisfactory amplitude and phase matching (R^2 = 0.90, p > 0.05). The calculated σ was < 10%. The measured respiration pressure matched well with the control analytical signal (R^2 = 0.65, p > 0.05). The calculated σ was < 5%.

Mean values of the (BCPA) pressures match well (p > 0.05) between the analytical prediction and experimental measurement. The pulsatility of experimental BCPA pressure is slightly higher than that of the analytical one (R^2 = 0.65, σ = 8%), and there is the visible lag of the peak. This may be caused by a mismatch of the compliance values and/or inertance effects not included in the analytical model.

In summary, the agreement between experimental and analytical pressures and flow rates are quite reasonable with satisfactory amplitude and phase matching (0.78 < R^2 < 0.90, p > 0.05 and σ < 10%). The results show acceptable functionality of the *in vitro* respiration model.

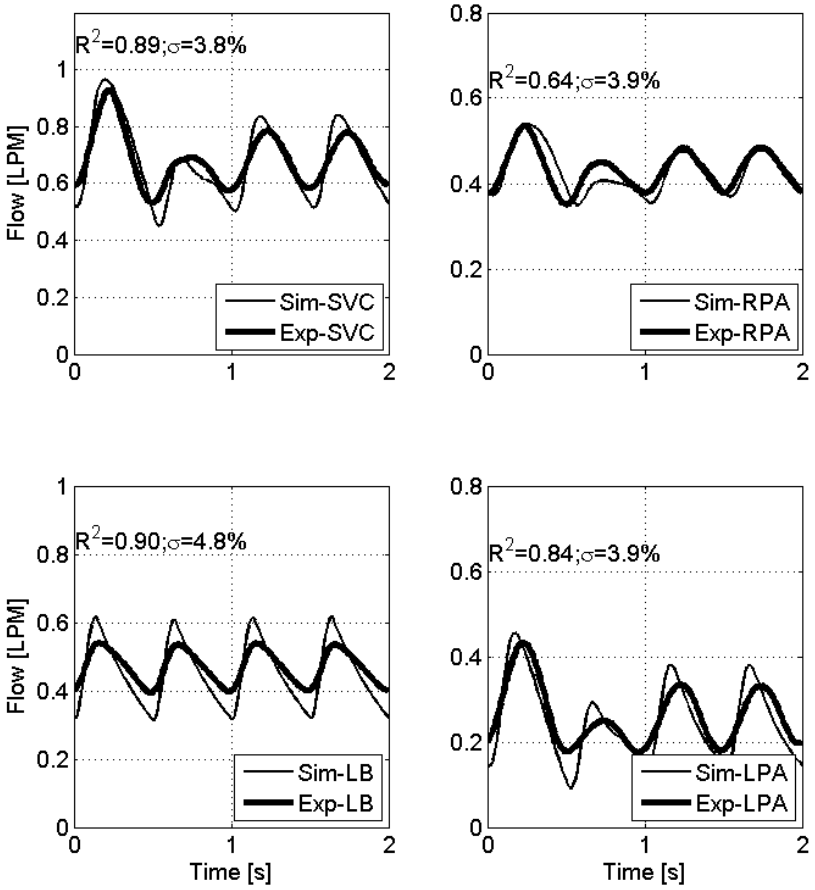

Figure 6.6: Comparison between analytical and experimental flow rate for UM2, time point 4. Exp, experimental; Sim, simulation; LB, lower body; LPA, left pulmonary artery; RPA, right pulmonary artery; SVC, superior vena cava.

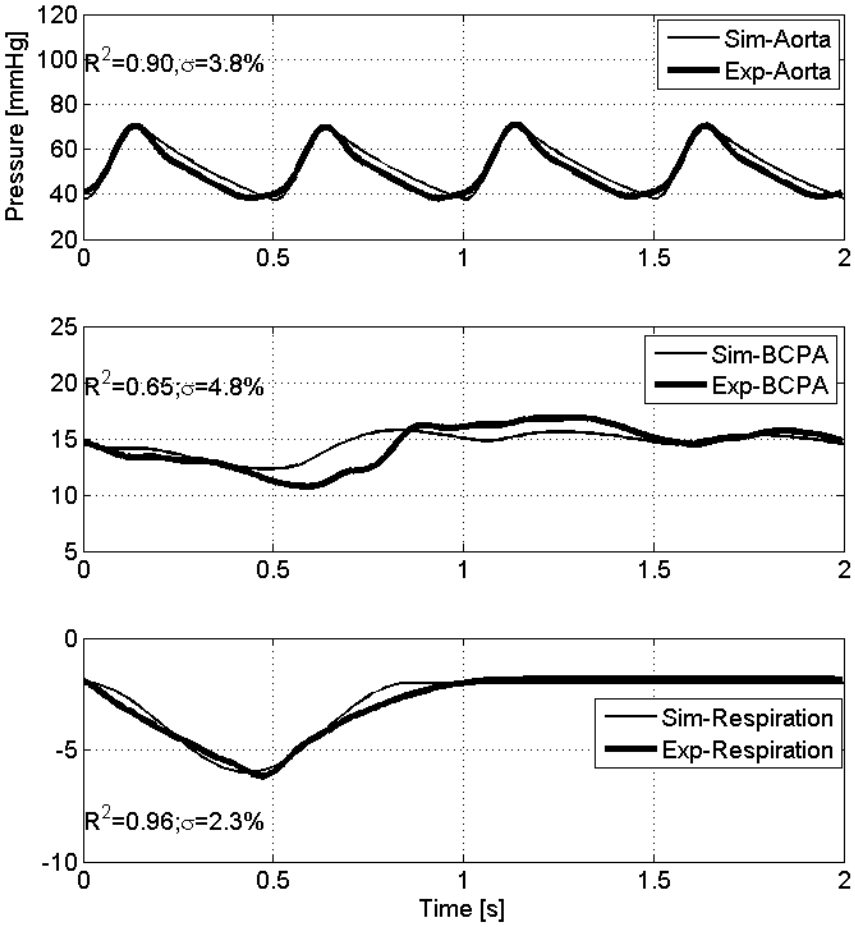

Figure 6.7: Comparison between analytical and experimental pressures for UM2, time point 4. Exp, experimental; Sim, simulation; BCPA, bidirectional cava pulmonary anastomosis.

Case UM2-TP5: Validation of the Respiration System

In most of the literature, clinical data in Stage 2 patients are only measured over one heartbeat, or heartbeat-gated. So, it is difficult to validate a respiration model using clinical data. Here we have two rare sets of clinical pressures (LPA and SVC) of patient UM2 at time point 5, recorded over one full respiration period and used to validate the

MCS. The comparison between the experimental and clinical LPA pressure and SVC pressure over one respiration period are given in Figure 6.8-6.9, respectively.

The experimental LPA pressure matched well with the clinical measurement, with satisfactory amplitude and phase matching (R^2 = 0.62, p > 0.05). The calculated σ was 7.6%. The experimental SVC pressure matched well with the clinical SVC pressure with satisfactory amplitude (p > 0.05) and phase matching (R^2 = 0.68) and σ was < 5%. These two well-reproduced signals demonstrate that the model is able to recapitulate the clinical signals with respiration. The high frequency pulsatility and noise in the clinical signals might be either physiological in nature or measurement noise, there is insufficient information to determine the cause.

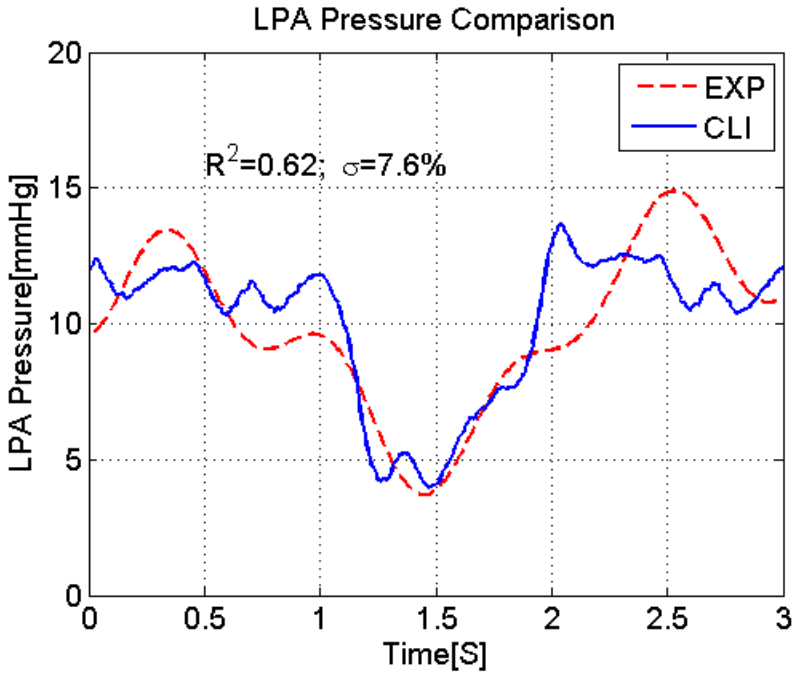

Figure 6.8: Comparison between clinical and experimental LPA pressures for UM2, time point 5. CLI, clinical; EXP, experimental; LPA, left pulmonary artery.

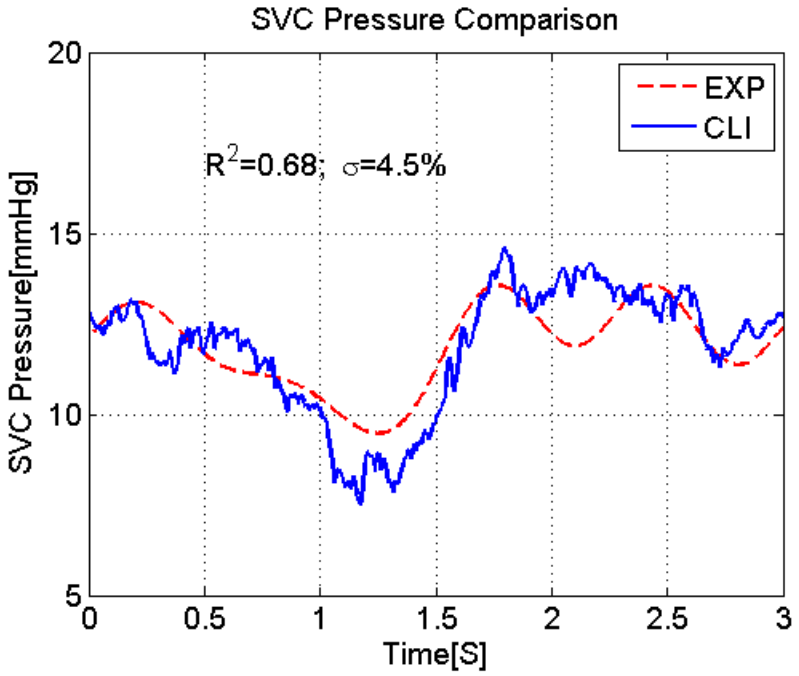

Figure 6.9: Comparison between clinical and experimental SVC pressures for UM2, time point 5. CLI, clinical; EXP, experimental; SVC, superior vena cava.

Discussion

This chapter introduced and verified the Stage 2 circulation with respiration model. Previous studies on Stage 2 circulation have only investigated the hemodynamics over one heartbeat. From the results in this chapter, the signals show a clear interaction between respiration and heartbeat. The impact of this time-based information on local hemodynamics has not been demonstrated previously in a model without respiration.

The pulsatility of flow rate and pressure is known to be beneficial for the growth of pulmonary vasculature [91]. Further, in a clinical Stage 2 study, SVC retrograde blood flow was documented to occur but not fully understood [97].

The Stage 2 MCS with respiration model presented offers a way to study these effects. If respiration effects affect flow pulsatility, then they will influence hemodynamics values, such as wall shear stress, directly. Respiration modeling provides more correct boundary conditions for the test section. Respiration is capacitive coupled, so it does not directly affect mean pressure or flows, but it does increase the RMS value of flow. Increased RMS can in fact increase the mean pressure drop through a nonlinear resistance, such as in the ABG shunt, with subsequent changes throughout the system. Also for three dimensional velocity field reconstruction, ignoring respiration will accumulate error [98].

In summary, the ability to impose respiration into an experimental model of the Stage 2 circulation has been verified by direct comparison to an LPN analytical model with respiration. Then the system was validated against rare clinical signals obtained over one full respiration cycle.

CHPTER SEVEN

SUMMARIES AND CONCLUSIONS

Summaries and Conclusions

An *in vitro* multi-scale model of the Norwood with mBTS and Glenn (BDG) circulations was proposed and built. Generic and patient-specific conditions were achieved and the system was verified and validated by comparing experimental results with numerical or/with clinical data. Resulting parameters measured were: pressure and flow rate at left/right pulmonary artery and superior vena cava (SVC). Systemic oxygen delivery (OD) was calculated. Experimental results of the time based pressures and flows demonstrated the same form as the clinical data or simulation predictions. The statistical analysis and frequency analysis shows good match ($0.62 < R^2 < 0.95$, $p > 0.05$; r.m.s error, $\sigma < 10\%$) between the *in vitro* MCS measurements, clinical data and numerical predictions. The hypothesis that it is possible to model the first and second stage palliation circulations using multi-scale *in vitro* circulation models was validated.

The validated *in vitro* model was used to recapitulate prior numerical simulation results while demonstrating the practical implementation of a novel approach to a first stage palliation of univentricular physiology called the ABG concept. Comparisons of the major experimental and numerical mean flow results were not significantly different ($p > 0.05$) and mean pressure differences were within 1.2 mmHg ($p > 0.05$). The phase also matched well ($0.62 < R^2 < 0.95$, $\sigma < 10\%$), lending confidence in the numerical model. The hypothesis that the *in vitro* model is able to test novel surgical strategies was validated.

The experimental results found that the ABG circulation provides an increase of 30–38% in pulmonary flow with a 2.0~3.7 mmHg increase in SVC pressure compared to the Glenn circulation and a 4~14% higher systemic OD than either the Norwood or the Glenn circulations. While the concept of the ABG circulation and the application remains hypothetical, the ABG circulation would have certain advantages over current palliation strategies. Using the ABG circulation in place of the Norwood circulation (such as the mBTS) as the initial palliation in neonates would reduce the number of surgeries in the Fontan circulation conversion from 3 to 2. While doing so, the ABG circulation could provide a more reliable source of pulmonary blood flow with reduced risk from thrombosis and cyanosis. The increased pulmonary blood flow and systemic oxygen delivery would allow for improved stress tolerance and reduce baseline cyanosis than the Norwood circulation. The ABG adds a component of pulsatility to the pulmonary blood flow, which could potentially improve pulmonary vascular development and exercise tolerance.

A study was conducted to examine the ejector pump effect used in the ABG circulation. Results show that the nozzle placed within the ABG shunt acted not only as a resistance element, but also produced an ejector pump effect. The hypothesis that an ejector pump advantage can be adopted in a superior cavo-pulmonary circulation, where the low-energy pulmonary blood flow can be assisted by an additional source of high energy flow from the systemic circulation was validated. But the eject pump effect was not strong enough to reduce the SVC pressure by more than 2.0 mmHg using the nozzle designs presented in the study.

The parametric study of the nozzle used in the ABG showed that the nozzle diameter to shunt diameter ratio β is the most important parameter when determining the ABG performance. A good choice on β fell between 0.48 and 0.72, which produced the highest systemic oxygen delivery without increasing SVC pressure to dangerous levels. A shunt angle between 30^o and 40^o show a slight improvement on pulmonary blood flow and systemic oxygen delivery over other angles. Nozzle design did not appear to have much influence on the systems-level hemodynamics, at least for the designs tested. However, nozzle placement did. Best results were obtained for a nozzle internal to the shunt as close to the SVC-shunt anastomosis as possible. Placing the nozzle within the SVC showed a blockage effect of higher SVC pressure with no other benefits.

As coarctation is common to initial palliation of single ventricle patients, the *in vitro* MCS was used to study the effects on the performance of the ABG circulation. A coarctation index (CoI) was used as a measure of coarctation severity. CoI variation of 0.3 to 0.9 was used in the study. Results demonstrated severe coarctaiton would decrease lower body flow and increase SVC and shunt flow. While total systemic oxygen delivery was not sensitive to coarctation, severe CoI produced measureable effects on oxygen delivery distribution to the upper body and the lower body. The results suggested that significant hemodynamic changes occurred for CoI < 0.5, suggesting a need for surgical intervention.

A Stage 2 circulation model with respiration effects was built and verified by comparing experimental signals (flow rates and pressures) with clinical data and/or numerical predictions with one respiration period ($0.65 < R^2 < 0.92$, $p > 0.05$, $\sigma < 10\%$).

Comparison between the respiration case and no respiration base case showed that respiration should be included to recapitulate clinical data.

In summary, the ABG could be used as a Stage 1 palliation option for single ventricle heart disease patients. It could provide more stable pulmonary blood flow source and relieve the ventricle load compared with the Norwood circulation. But due to limitations of the current nozzle designs studied, the ejector effect of the nozzle is not strong.

Limitations

Although there is satisfactory matching between the experimental results, LPN analytical results, multi-scale numerical results, and clinical data, there are limitations that should be clear:

(1): The data required for tuning of the circuit sometimes must rely on generic information taken from literature. In the case of the Stage 2, time point 4 validation, the patient data was taken at a time point just prior to the Stage 3 surgery, not after the Stage 2. This presents a problem in model validation as there is usually no post-surgical clinical data to validate the system's functionality for the time point just after the surgery.

(2): The 3D model geometry used in the experimental models has been simplified in some respects. For instance, in the *in vitro* study, the coronary arteries were not modeled and the multi-generational daughter pulmonary artery branches of the lungs were not modeled.

(3): The test section vessel walls were rigid, just as they were in the numerical models used for comparison. However, a lumped aortic compliance was used to accommodate for the rigid aortic walls resulting in the clinically realistic aortic pressure waveforms.

(4): Gravity was not accounted for the models. Tests assumed the patient to be in the supine position under resting conditions. The MCS can be tuned for exercise conditions and adjusted to represent upright stature, but these were not tested here.

(5): The ABG concept was only assessed globally by comparing the pressures and flow rates. Future work should investigate the local parameters to assess the ABG comprehensively. Suggested parameters include wall shear stress (WSS), energy losses and thrombosis risk. Eventually, animal studies are needed to assess the ABG concept for patients.

APPENDICES

Appendix A: Thevenin Theory to Reduce a Full Model

This section describes how to reduce one LPN branch of the circulation into a reduced LPN model. To do this, we apply least-squares matching of the impedance spectrum from Thevenin equivalent circuit analysis. Given an arbitrarily complex network of resistances, compliances, inertances, and pressure sources, the Thevenin theory says that the behavior of the network with respect to a certain outlet can be fully described by one source pressure, and the outlet impedance spectrum. A simple R-C-R block to most-closely approximate the impedance spectrum was designed. It connects its outlet to an inlet to the test section, and will most-accurately reproduce the sensitivity of the full model to both steady and unsteady flow dynamics in the test section.

Here an example of using the method to reduce the SVC branch from the patient-specific model of patient MUSC2 at Time point 4 (post-Glenn surgery examination) was given. Figure A.1 depicts the original full SVC branch. The values of each element are listed in Table A.1. The target reduced branch is shown in Figure A.2. The described method is used to determine the equivalent values for the reduced branch design.

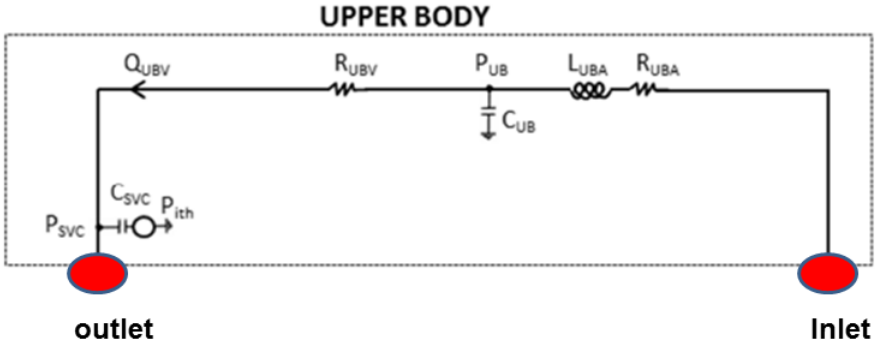

Figure A.1: The full model of the SVC branch, MUSC 2, time point 4 (After Glenn surgery).

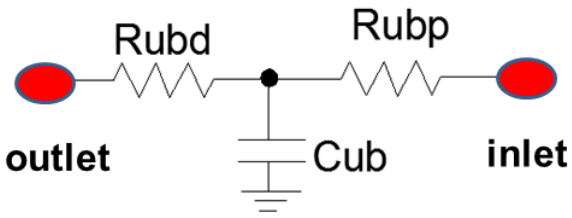

Figure A.2: The targeted reduced R-C-R block from the full SVC branch.

Table A.1: Parameters of the full SVC branch shown in Figure A.1

Parameter	Value
R_{UBA}	2.01 mmHg.s/ml
L_{UBA}	6.26E-04mHg* s^2 / ml^2
C_{UB}	0.57 ml/mmHg
R_{UBV}	5.87 mmHg.s/ml
C_{SVC}	0.26 ml/mmHg
R_{SVC}	0.54 mmHg.s/ml

The ordinary differential equations (ODEs) for the SVC branch shown in Figure A.1 are listed below:

$$P_{UB} - P_{SVC} = R_{UVB} \cdot Q_{UBV} \tag{A-1}$$

$$Q_{UBA} - Q_{UBV} = C_{UB} \frac{dP_{UB}}{dt} \tag{A-2}$$

$$P_{AO} - P_{UB} = R_{UBA} \cdot Q_{UBA} + L_{UBA} \cdot \frac{dQ_{UBA}}{dt} \tag{A-3}$$

where P_{AO} is the aorta pressure.

According to Kirchhoff's circuit law,

$$Q_{UBA} = Q_{UBV} + Q_{C_{UB}} \tag{A-4}$$

$$\frac{P_{AO} - P_{UB}}{R_{UBA} + s \cdot L_{UBA}} = \frac{P_{UB} - P_{SVC}}{R_{UBV}} + \frac{P_{UB}}{1/(s \cdot C_{UB})} \tag{A-5}$$

where $s = 2\pi f$, f is the frequency.

The Thevenin pressure was obtained with the assumption that the SVC circuit is open (no out flow). This assumption is equivalent to the clinical method to measure the wedge pressure, which was measured using catheter tip 'wedged' in the tapering branch. So

$$\frac{P_{UB} - P_{SVC}}{R_{UBV}} = \frac{R_{SVC}}{1/(s \cdot C_{SVC})} \tag{A-6}$$

The Thevenin pressure $P_{SVC-OPEN}$ can be obtained by solving (A-5) and (A-6):

$$\begin{bmatrix} 1/(R_{UBA}+s*L_{UBA})+s*C_{UB}+1/R_{UBV} & -1/R_{UBV} \\ -1/R_{UBV} & 1/R_{UBV}+s*C_{SVC} \end{bmatrix} \cdot \begin{bmatrix} P_{UB} \\ P_{SVC-OPEN} \end{bmatrix} = \begin{bmatrix} P_{AO}/(R_{UBA}+s \cdot L_{UBA}) \\ 0 \end{bmatrix}$$

The Thevenin flow rate was calculated with the assumption that the SVC branch was close or connected to the ground (0mmHg pressure) (also called "short circuit"). The clinical meaning of this is if the vein were severed, so the blood flows out to atmospheric pressure. Then

$$\frac{P_{UB} - P_{SVC}}{R_{UBV}} = \frac{R_{SVC}}{1/(s \cdot C_{SVC})} + \frac{P_{SVC}}{R_{SVC}} \tag{A-7}$$

$P_{SVC\text{-}SC}$ is obtained by solving the following matrix based on (A-5) and (A-7):

$$\begin{bmatrix} 1/(R_{UBA}+s*L_{UBA})+s*C_{UB}+1/R_{UBV} & -1/R_{UBV} \\ -1/R_{UBV} & 1/R_{UBV}+s*C_{SVC}+1/R_{SVC} \end{bmatrix} \cdot \begin{bmatrix} P_{UB} \\ P_{SVC-SC} \end{bmatrix} = \begin{bmatrix} P_{AO}/(R_{UBA}+s \cdot L_{UBA}) \\ 0 \end{bmatrix}$$

then the short-circuit flow of Q_{SVC-SC} equals P_{SVC-SC} / R_{SVC}.

The final impedance of the branch can be calculated as

$$Z_1(s) = P_{SVC-OPEN} / Q_{SVC-SC} \qquad \text{(A-8)}$$

Applying the same method, the outlet impedance of a reduced R-C-R block, as shown in Figure A.2, for a given frequency f can be expressed as a single equation:

$$Z_2(s) = \frac{R_D+R_P+s \cdot R_D \cdot R_P \cdot C}{1+s \cdot R_D \cdot C} \qquad \text{(A-9)}$$

Figure A.3 shows the complex impedance spectrum for the full model (blue line), and the reduced model (red line). At zero frequency (steady flow), the impedance is real-valued, equal to the total resistance, 8.42 mmHg*s/ml. This is one constraint on the design of the reduced model. Two free variables remain, the values of C and R_{ubp}. The system will be driven by the heartbeat, and therefore it is most important to match the impedance at the fundamental frequency of the heartbeat, and its first three harmonics. The complex impedance at those frequencies is marked with circles in Figure A.3. The values of C and R_{ubp} were optimized in an iterative search, minimizing the sum of squares of impedance errors at those chosen frequencies, and finally the value of R_{ubp} was calculated from R_{ubp}. The final reduced design is R_{ubd} =7.86 mmHg*s/ml, C_{ub} = 0.26 ml/mmHg, R_{ubp} =0.56 mmHg*s/ml, and the impedance match is excellent at the four frequencies of interest.

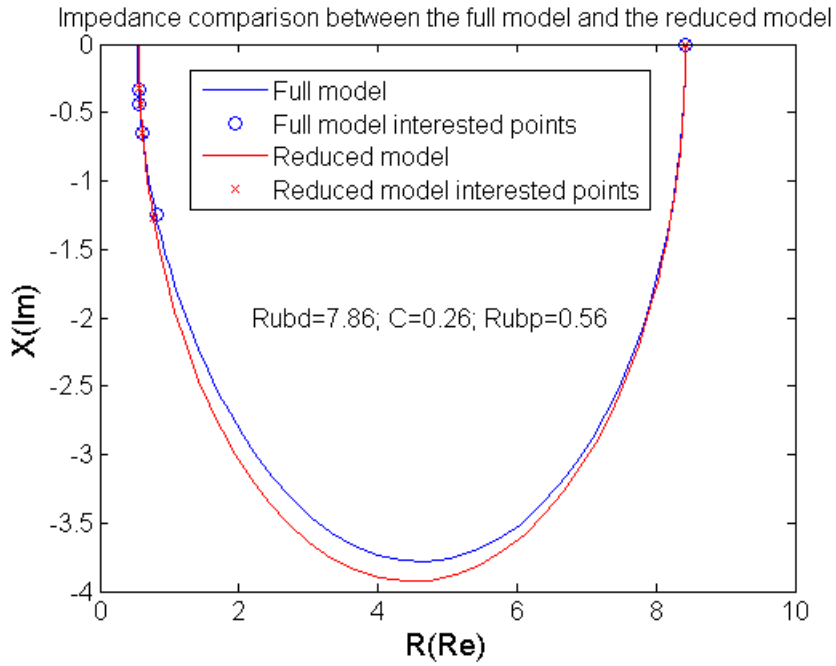

Figure A.3: Impedance spectrum comparison between the two models. For frequencies f > 0 the imaginary component of the spectrum is negative, indicating that pulsatile flow leads pressure as expected for a compliant system.

Appendix B: Resistance Calibration

The calibration system schematic for calibrating resistance element is given in Figure B.1. The height difference of two head tanks was used to drive a flow producing the pressure differential across the resistance element. Resistance was calculated by the measured pressure differential and flow rate. For a ball valve, the resistance is not constant and is a function of flow rate. So it was important to calibrate the resistance under the operational flow rate. Laminar resistors using capillary glass was made following the method introduced by Kung and Taylor [99]. Figure B.1 to Figure B.3 are the schematic of the test table and details of the resistance element construction. Glass capillaries with different outer diameters, inner diameters and lengths (Sutter Instrument;

One Digital Drive, Novato, CA 94949, USA) were used to produce different resistance values. Resistance was preestimated by:

$$R=\frac{8\mu l}{\pi N r^4} \qquad \text{（B-1）}$$

where μ is the dynamic viscosity of fluid, l is the length of the glass capillaries, N is the number of capillaries inserted in the tube and r is the inner radius of the capillary glass. Though outer radius is not shown in the equation, its value and radius of the tube determine N. The relationship between the N, tube diameter and capillary glass outer diameter were established using the application found at: http://hydra.nat.uni-magdeburg.de/packing/cci/cci.html. The predicted values were used as a starting point for a laminar resistance element design. Small adjustments were made by blocking some capillaries using silicone adhesive.

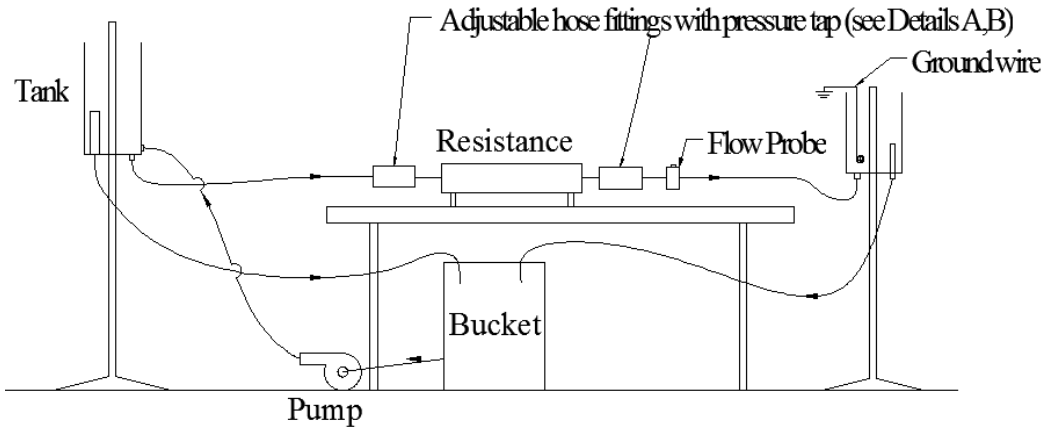

Figure B.1: Schematic of the resistance element calibration system.

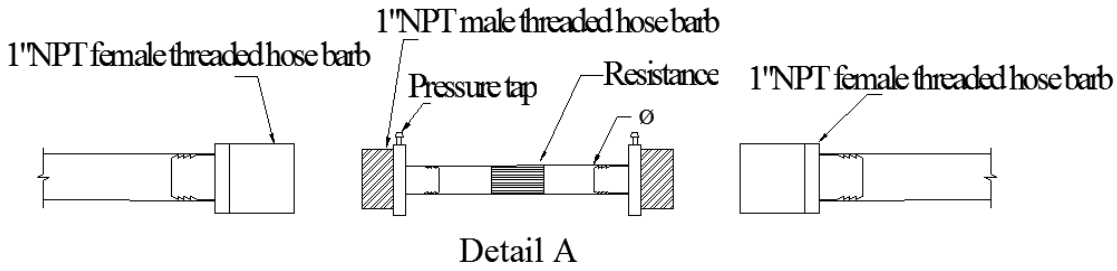

Figure B.2: Detail A about the resistance element component

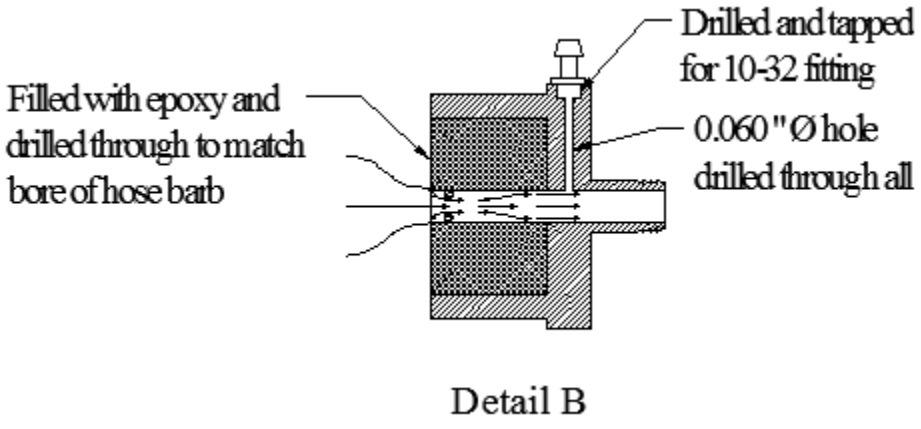

Figure B.3: Detail B for components in resistance element connector.

Appendix C: Compliance Calibration

Compliance values were confirmed by calibration, which measured the volume change associated with an applied pressure change to the compliance element. All the compliances in the system were grounded to atmosphere, except the respiration compliance, which was grounded to the respiration pressure. The compliances grounded to the atmosphere respond to the pressure variation of the connected branch, whereas a compliance grounded to the respiration pressure responds to an applied respiration pressure. The respiration pressure itself was applied to the sealed air chamber so as to act on the exterior surface of the compliance element.

The calibration process for the compliance value involved varying the pressure in the liquid side and measuring the volume change of the liquid. The operable pressure range was selected based on the appropriate pressures the compliance was associated with.

The setup of the compliance value tuning or calibration system was introduced by Chiulli [100] and is shown in Figure C.1. In practice, the air chamber is connected to a tube, which is filled with water. Another end of the tube is left open to air. The tube is lowered down below the air chamber and made into a U-shape

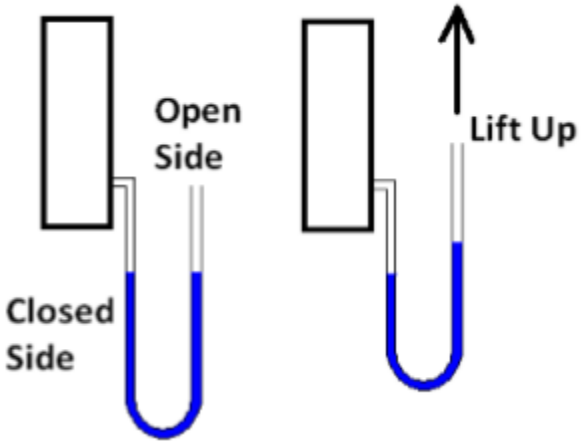

Figure C.1: Compliance tuning system [90]

At the initial state, the fluid heights in both legs of the U-tube (Figure C.1) were equal. The open side tube was next raised to a height. The pressure change applied to the chamber equals to the difference in height between the two water columns. The volume change was estimated by the change in the fluid's height on the closed side. Several pressure and volume data points were obtained by lifting the tube. A pressure change versus volume change (P-V) diagram, whose slope equals to the compliance, was plotted to calculate the compliance.

As an example, Table C.1 gives the measured data for one compliance calibration and Figure C.2 is the corresponding P-V curve constructed from it. Compliance remains nearly linear over a small piecewise range. For this example, the slope of the graph gives C=0.60 ml/mmHg.

Table C.1: Spreadsheet of compliance calibration procedures

Points	z(cm)	Δz(cm)	Δh(cm)	Δp(mmHg) Δp=Δz*10/13.6	Δv(ml) Δv=(Δh-Δz)*A
1	22.50	0.00	0.00	0.00	0.00
2	28.10	5.60	20.00	4.12	2.62
3	31.10	8.60	30.00	6.32	3.89
4	34.10	11.60	40.00	8.53	5.16
5	37.00	14.00	50.00	10.29	6.54
6	40.10	17.60	60.00	12.94	7.71

z, water level reading; Δz , change of water height from starting point; Δh , change of hose height; Δp , pressure change; Δv , volume change.

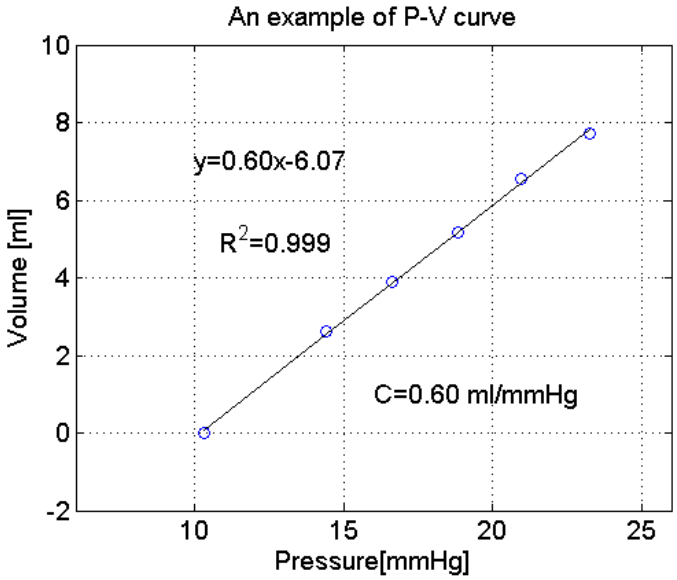

Figure C.2: An example of pressure and volume curve used to calculate compliance value.

Appendix D: Uncertainty Analysis

In this section, the methods used to calculate the uncertainty for the LPN parameters (R, C values), measured results (pressure and flow rates) and calculated parameter (oxygen delivery) presented in this dissertation are discussed.

Errors are divided into two categories: systemic error and random error [101]. The systemic errors shift the sample mean away from the true mean by a fixed but unknown amount, and within a sample of many measurements, the random errors bring about a distribution of measured values about the sample mean. The approach to propagate the uncertainties used in this dissertation is described by Figliola and Beasley [101]. Elemental systemic errors, systemic standard uncertainties are propagated as:

$$b = (\sum_k (\theta b_k))^{\frac{1}{2}} \quad \text{(D-1)}$$

where θ is the sensitivity factor. In a similar manner, random standard uncertainties are propagated as

$$s = (\sum_k (\theta s_k))^{\frac{1}{2}} \quad \text{(D-2)}$$

Uncertainty estimation for pressure and flow rate measurements

Sources of uncertainties in the pressure and flow rate results include instrument error, zero set-point error, data-acquisition error, and the statistical standard error from measurement. Instrument errors are determined by systematic uncertainty according to manufacturer's manual statement of error. The instrument error is specified as 0.5% of the instrument reading for both flow and pressure measurements. Zero set-point error,

which is the difference between the tuned zero point and the real zero point, is 0.10 mmHg and 0.01 LPM for pressure measurement and flow rate measurement, respectively, in our experience with these instruments. Data-acquisition error is defined as the error produced during the measurement process. The value is based on the voltage range of the sensors and number of bits of the DAQ board, the equation utilized is:

$$u_{DAQ} = \frac{(\frac{V_R}{2^n})}{S} \quad \text{(D–3)}$$

where VR is the voltage range of the sensors and n is the number of bits of the DAQ board (16 in the National Instruments USB-6211).

The statistical standard error (or standard error of the mean: SEM), was calculated by:

$$s_{\bar{x}} = \frac{s_x}{\sqrt{N}} \quad \text{(D-4)}$$

where s_x is the sample standard deviation, and N is the number of samples. In this dissertation, a data set of 20 mean values was used to calculate the standard error.

Based on the introduction above on each type of uncertainty distribution, a sample of uncertainty calculation details for one flow and one pressure measurement in the ABG circulation is given in Table D.1.

Table D.1: An example to calculate uncertainty for pressure and flow measurement

Name	Reading	Systemic uncertainty			Random uncertainty	Total Uncertainty	Relative Value
		Instrument Uncertainty	Zero-point uncertainty	Data acquisition uncertainty			
P_{ao} (mmHg)	54.1	0.27	0.10	0.004	0.50	0.58	1.1%
CO (LPM)	1.05	0.005	0.01	0.003	0.02	0.023	2.2%

Uncertainty estimation for resistance and compliance value

Resistance is a function of pressure difference (ΔP) and flow rate (Q) with equation $R=\frac{P_1-P_2}{Q}$. Its uncertainty estimation is calculated by:

$$u_R=\sqrt[2]{\left(\frac{1}{Q}\times u_{P_1}\right)^2+\left(\frac{1}{Q}\times u_{P_2}\right)^2+\left(\frac{P_1-P_2}{Q^2}\times u_Q\right)^2} \quad \text{(D-5)}$$

This treatment assumes that P_1 and P_2 are measured by independent channels, as was often the case, so that there is no correlation of the instrument uncertainty between them.

The compliance of a trapped-air style compliance element (or "windkessel," as in Chapter 2), is a function of the trapped air volume (V) and absolute pressure (P_{abs}), with $C=\frac{V}{P_{abs}}$. The uncertainty estimation for the windkessel compliance is given by:

$$u_C=\sqrt[2]{\left(\frac{\partial C}{\partial P}\times u_P\right)^2+\left(\frac{\partial C}{\partial V}\times u_V\right)^2} \quad \text{(D-6)}$$

An example of uncertainty estimation for R, C value used in the ABG circulation test, high PVR was given in Table D.2 and Table D.3, respectively. For R calculation, Q was set at 0.60 LPM, P_1 and P_2 were set at 54.0 mmHg and 2.0 mmHg, respectively. For C uncertainty calculation, V is 154.1 ml and P_{abs} is 760 mmHg. A relative uncertainty of 1%, namely 1.5ml and 6.7 mmHg, were utilized in the calculations.

Table D.2: An example (ABG, high PVR) to calculate the uncertainty estimation for Resistance

Name	Value	$\frac{\partial R}{\partial Q}$	u_Q	$\frac{\partial R}{\partial P_1}$	u_{P_1}	$\frac{\partial R}{\partial P_2}$	u_{P_2}	Total Uncertainty	Relative Uncertainty
R_{lb}	5.48	0.52	0.28	0.09	0.54	0.09	0.20	0.16	2.9%

Table D.3: An example (ABG, high PVR) to calculate the uncertainty estimation for Compliance

Name	Value	$\frac{\partial C}{\partial V}$	u_V	$\frac{\partial C}{\partial P}$	u_P	Total Uncertainty	Relative Uncertainty
C_{lb}	0.23	0.0015	1.5	0.00034	6.7	0.0032	1.4%

Oxygen delivery Uncertainty calculation

Systemic oxygen delivery (OD) was calculated by measured flow rates and referred clinical values:

$$OD = Q_s C_p - r\frac{Q_s}{Q_p}V_{o_2} \quad \text{(D-7)}$$

where C_p stands for oxygen concentration in pulmonary, V_{o_2} stands for total oxygen consumption and $r = v_{lb.o_2}/v_{o_2}$. The uncertainty estimation for oxygen delivery is given by:

$$u_{OD} = \sqrt{[(C_p - \frac{rV_{o_2}}{Q_p})u_{Q_S}]^2 + (\frac{rQ_sV_{o_2}}{Q_p{}^2}u_{Q_p})^2 + (Q_s u_{Q_{C_P}})^2 + (\frac{rQ_s}{Q_P}u_{V_{O_2}})^2} \quad \text{(D-8)}$$

An example of OD uncertainty estimation is given in Table D.4. The values of C_p and V_{o_2} were set to $0.22\, ml_{o_2}/ml$ and $0.874\, ml_{o_2}/s$ as reported in a previous study[26] and was quite constant, a reasonable uncertainty estimation for these two clinical data were 5% ($0.011\, ml_{o_2}/ml$ for C_P and $0.0437\ ml_{o_2}/s$ for V_{o_2}).

Table D.4: An example (ABG, high PVR) to calculate the uncertainty estimation for OD

Name	Value	$\frac{\partial(OD)}{\partial Q_s}$	u_{Q_s}	$\frac{\partial(OD)}{\partial Q_p}$	u_{Q_p}	$\frac{\partial(OD)}{\partial C_p}$	u_{C_p}	$\frac{\partial(OD)}{\partial V_{O_2}}$	$u_{V_{O_2}}$	u_{OD}	Relative Uncertainty
OD	3.09	0.175	0.47	0.083	0.47	17.7	0.011	0.98	0.0437	0.21	6.8%

Appendix E: Calculation of Coefficient of Determination

In a linear regression model $\hat{y} = \hat{\beta}_0 + \hat{\beta}_1 x$, coefficient of determination (R^2) is defined by [102]:

$$R^2 = \frac{SSR}{SST} = 1 - \frac{SSE}{SST} \quad \text{(E-1)}$$

where SST is the total sum of squares, calculated by

$$SST = \sum_{i=1}^{n} (Y_i - \overline{Y})^2 \qquad \text{(E-2)}$$

where Y_i is the real dependent variable corresponding to the i_{th} independent variable x_i , $\overline{Y}$ is mean of all the dependent variables. The regression sum SSR is given by

$$SSR = \sum_{i=1}^{n} (Y_i - \overline{Y})^2 \qquad \text{(E–3)}$$

where $\overline{Y_i}$ is the estimated dependent variable based on the linear regression model. The error sum of squares SSE is given by

$$SSE = \sum_{i=1}^{n} (Y_i - Y_i)^2 \qquad \text{(E–4)}$$

In this dissertation, experimental results and clinical data or signals from the numerical model were compared point-to-point at corresponding times using linear regression (y = x) from which a coefficient of determination (R^2) was calculated. The closer to unit in R^2, the better linear association between x and y, suggesting the better match between the experimental results and clinical measurements or numerical predictions.

Appendix F: t-test and p value Calculation

In this dissertation, an unpaired Student's t-test was used to compare the mean values between different models, such as experimental results to clinical measurements or experimental results to numerical predictions. A p-value of 0.05 or less ($p < 0.05$) was

considered to indicate a statistically significant difference between the two mean values. Values were determined using Mablab.

The unpaired student's t test tests the null hypothesis that the population means related to two independent, random samples from an approximately normal distribution are equal [103]. If the variances of the two set of data are equal, the test statistic is calculated by:

$$t = \frac{\overline{x_1} - \overline{x_2}}{\sqrt{s^2\left(\frac{1}{n_1} + \frac{1}{n_2}\right)}} \qquad \text{(F-1)}$$

$$s^2 = \frac{\sum_{j=1}^{n_1}(x_j - \overline{x_1})^2 + \sum_{i=1}^{n_2}(x_i - \overline{x_2})^2}{n_1 + n_2 - 2} \qquad \text{(F-2)}$$

where $\overline{x_1}$ and $\overline{x_2}$ are the sample means, s^2 is the sample variance, n_1 and n_2 are the sample sizes and t is the t-value with freedom $n_1 + n_2 - 2$.

Appendix G: RMS-Error Calculation

Root-mean-square (r.m.s) error is the root-sum-square of the deviation between two values observed at the same time point in a time-based signal. The deviations are summed over the full heartbeat. Hence the experimental signal is compared to either the numerical signal or clinical signal. The use of rms error is an excellent general purpose error metric for numerical predictions [104]. Its value is given by:

$$r.m.s \text{ error} = \sqrt{\frac{1}{n}\sum_{i=1}^{n}(y_i - y_i)^2} \qquad \text{(G-1)}$$

where y_i is the observed value (in this research, the observed value is the clinical data) and y_i is the predicted value (in this research, the predicted value is the experimental data). The rms error reported in this document is normalized by the mean values as:

$$\sigma = rms \text{ error}/\bar{y} \quad \text{(G-2)}$$

Appendix H: Oxygen Delivery (OD) Calculation

Oxygen delivery within the MCS was not measured but calculated based on flow rates to the various branches. Let V_{o_2} $V_{lb.o_2}$, $V_{ub.o_2}$ represent total oxygen consumption, lower body oxygen consumption and upper body oxygen consumption, C_P , C_{ao} , C_{ivc} , C_{svc} stands for oxygen concentration in pulmonary, aorta, IVC and SVC , respectively and defines:

$$r = \frac{V_{lb.o_2}}{V_{o_2}} \qquad \text{(H-1)}$$

So:

$$V_{ub.o_2} = (1-r)V_{o_2} \qquad \text{(H-2)}$$

Oxygen delivery (OD) is the product of oxygen concentration in aorta and systemic flow rate by definition:

$$OD = C_{ao} Q_s \qquad \text{(H-3)}$$

Applying the conservation of oxygen equation [29]:

$$\mathrm{V}_{ub.o_2} = Q_{ub}(C_{ao} - C_{svc}) \qquad \text{(H-4)}$$

Subtracting equations H-2 and H-4, the SVC consumption is

$$C_{svc} = C_{ao} - (1-r)\frac{V_{o_2}}{Q_{ub}} \qquad \text{(H-5)}$$

We assume r equals 0.5 for most of the cases. The C_p and V_{o_2} are set to 0.22 mL_{o_2} / mL and 0.874 mL_{o_2} / s on the basis of generic clinic data obtained from catheterization exams and the fact that pulmonary veins has a 98% oxygen saturation [26].

a) For the mBTS circulation:

$$V_{o_2} = Q_p(C_p - C_{ao}) \qquad \text{(H-6)}$$

and combined with equation H-3, we can get:

$$\mathrm{OD} = \mathrm{Q_s}\, C_p - \frac{Q_s}{Q_p} V_{o_2} \qquad \text{(H-7)}$$

b) In the Glenn circulation:

$$V_{o_2} = Q_p(C_p - C_{svc}) \qquad \text{(H-8)}$$

Also, as in the Glenn circulation, the SVC in connected directly to the pulmonary circulation, so $Q_{svc} = Q_p$. From equation H-5 and H-8,

$$C_{ao} = C_p - r\frac{V_{o_2}}{Q_p} \qquad \text{(H-9)}$$

Inserting equation H-9 into equation H-3, the oxygen delivery is

$$\mathrm{OD} = \mathrm{Q}_s\, C_p - r\frac{Q_s}{Q_p}V_{o_2} \qquad \text{(H-10)}$$

c) The ABG circulation is a combination of the Glenn and mBTS circulations. The oxygen consumption is found by

$$V_{o_2} = (Q_p - Q_{ub})(C_p - C_{ao}) + Q_{ub}(C_p - C_{svc}) \qquad \text{(H-11)}$$

Using equation H-5 and H-3, we get the same expression for oxygen delivery as in the Glenn circulation:

$$\mathrm{OD} = \mathrm{Q}_s\, C_p - r\frac{Q_s}{Q_p}V_{o_2} \qquad \text{(H-12)}$$

REFERENCE

1. Lev M. Pathologic anatomy and interrelationship of hypoplasia of the aortic tract complexes. Laboratory investigation; a journal of technical methods and pathology. 1952;1(1):61.

2. Barron DJ, Kilby MD, Davies B, Wright JG, Jones TJ, Brawn WJ. Hypoplastic left heart syndrome. The Lancet. 2009;374(9689):551-64.

3. Connor JA, Thiagarajan R. Hypoplastic left heart syndrome. Orphanet J Rare Dis. 2007;2(23):1-5.

4. Quintessenza JA, Morell VO, Jacobs JP. Achieving a balance in the current approach to the surgical treatment of hypoplastic left heart syndrome. Cardiology in the Young. 2004;14(S1):127-30.

5. Norwood WI, Kirklin JK, Sanders SP. Hypoplastic left heart syndrome: experience with palliative surgery. The American journal of cardiology. 1980;45(1):87-91.

6. Weldner PW, Myers JL, Gleason MM, Cyran SE, Weber HS, White MG et al. The Norwood operation and subsequent Fontan operation in infants with complex congenital heart disease. The Journal of thoracic and cardiovascular surgery. 1995;109(4):654-62.

7. Sano S, Ishino K, Kawada M, Arai S, Kasahara S, Asai T et al. Right ventricle–pulmonary artery shunt in first-stage palliation of hypoplastic left heart syndrome. The journal of thoracic and cardiovascular surgery. 2003;126(2):504-9.

8. Blalock A, Taussig HB. The surgical treatment of malformations of the heart: in which there is pulmonary stenosis or pulmonary atresia. Journal of the American Medical Association. 1945;128(3):189-202.

9. Moulton A, Brenner J, Ringel R, Nordenberg A, Berman M, Ali S et al. Classic versus modified Blalock-Taussig shunts in neonates and infants. Circulation. 1985;72(3 Pt 2):II35.

10. Karpawich P, Bush C, Antillon J, Amato J, Marbey M, Agarwal K. Modified Blalock-Taussig shunt in infants and young children. Clinical and catheterization assessment. The Journal of thoracic and cardiovascular surgery. 1985;89(2):275-9.

11. Azakie A, Merklinger SL, McCrindle BW, Van Arsdell GS, Lee K-J, Benson LN et al. Evolving strategies and improving outcomes of the modified Norwood procedure: a 10-year single-institution experience. The annals of thoracic surgery. 2001;72(4):1349-53.

12. Corsini C. Computational models of the hemodynamics in stage 1 palliations for the treatment of single ventricle diseases. 2013.

13. Migliavacca F, Dubini G, Pennati G, Pietrabissa R, Fumero R, Hsia T-Y et al. Computational model of the fluid dynamics in systemic-to-pulmonary shunts. Journal of biomechanics. 2000;33(5):549-57.

14. Migliavacca F, Balossino R, Pennati G, Dubini G, Hsia T-Y, de Leval MR et al. Multiscale modelling in biofluidynamics: application to reconstructive paediatric cardiac surgery. Journal of biomechanics. 2006;39(6):1010-20.

15. Bove EL, Migliavacca F, de Leval MR, Balossino R, Pennati G, Lloyd TR et al. Use of mathematic modeling to compare and predict hemodynamic effects of the modified Blalock–Taussig and right ventricle–pulmonary artery shunts for hypoplastic left heart syndrome. The Journal of thoracic and cardiovascular surgery. 2008;136(2):312-20. e2.

16. Ohye RG, Sleeper LA, Mahony L, Newburger JW, Pearson GD, Lu M et al. Comparison of shunt types in the Norwood procedure for single-ventricle lesions. New England Journal of Medicine. 2010;362(21):1980-92.

17. Hsia T-Y, Cosentino D, Corsini C, Pennati G, Dubini G, Migliavacca F. Use of mathematical modeling to compare and predict hemodynamic effects between hybrid and surgical Norwood palliations for hypoplastic left heart syndrome. Circulation. 2011;124(11 suppl 1):S204-S10.

18. Corsini C, Cosentino D, Pennati G, Dubini G, Hsia T-Y, Migliavacca F. Multiscale models of the hybrid palliation for hypoplastic left heart syndrome. Journal of Biomechanics. 2011;44(4):767-70. doi:10.1016/j.jbiomech.2010.11.001.

19. Migliavacca F, Yates R, Pennati G, Dubini G, Fumero R, de Leval MR. Calculating blood flow from Doppler measurements in the systemic-to-pulmonary artery shunt after the Norwood operation: a method based on computational fluid dynamics. Ultrasound in medicine & biology. 2000;26(2):209-19.

20. Pennati G, Fiore G, Migliavacca F, Lagana K, Fumero R, Dubini G. In vitro steady-flow analysis of systemic-to-pulmonary shunt haemodynamics. Journal of biomechanics. 2001;34(1):23-30.

21. Tacy TA, Whitehead KK, Cape EG. In vitro Doppler assessment of pressure gradients across modified Blalock-Taussig shunts. The American journal of cardiology. 1998;81(10):1219-23.

22. Song M-H, Sato M, Ueda Y. Three-dimensional simulation of the Blalock-Taussig shunt using computational fluid dynamics. Surgery today. 2001;31(8):688-94.

23. Sant'Anna JRM, Pereira DC, Kalil RA, Prates PR, Horowitz E, Sant'Anna RT et al. Computer dynamics to evaluate blood flow through the modified Blalock-Taussig shunt. Revista Brasileira de Cirurgia Cardiovascular. 2003;18(3):253-60.

24. Malota Z, Nawrat Z, Kostka P, Mizerski J, Nowinski K, Waniewski J. Physical and computer modelling of blood flow in a systemic-to-pulmonary shunt. The International journal of artificial organs. 2004;27(11):990-9.

25. Kitagawa T, Katoh I, Fukumura Y, Yoshizumi M, Masuda Y, Hori T. Achieving optimal pulmonary blood flow in the first-stage of palliation in early infancy for complex cardiac defects with hypoplastic left ventricles. Cardiology in the Young. 1995;5(01):21-7.

26. Migliavacca F, Pennati G, Dubini G, Fumero R, Pietrabissa R, Urcelay G et al. Modeling of the Norwood circulation: effects of shunt size, vascular resistances, and heart rate. American Journal of Physiology-Heart and Circulatory Physiology. 2001;280(5):H2076-H86.

27. Moghadam ME, Migliavacca F, Vignon-Clementel IE, Hsia T-Y, Marsden AL. Optimization of shunt placement for the Norwood surgery using multi-domain modeling. Journal of biomechanical engineering. 2012;134(5).

28. Barnea O, Austin EH, Richman B, Santamore WP. Balancing the circulation: theoretic optimization of pulmonary/systemic flow ratio in hypoplastic left heart syndrome. Journal of the American College of Cardiology. 1994;24(5):1376-81.

29. Barnea O, Santamore WP, Rossi A, Salloum E, Chien S, Austin EH. Estimation of oxygen delivery in newborns with a univentricular circulation. Circulation. 1998;98(14):1407-13.

30. Ashburn DA, McCrindle BW, Tchervenkov CI, Jacobs ML, Lofland GK, Bove EL et al. Outcomes after the Norwood operation in neonates with critical aortic stenosis or aortic valve atresia. The Journal of Thoracic and Cardiovascular Surgery. 2003;125(5):1070-82.

31. Wong M, Sim E, Goh J, Quek S, Wong J, Yip W et al. Bidirectional cavopulmonary anastomosis. Annals of the Academy of Medicine, Singapore. 1999;28(2):237-40.

32. SADE R, FYFE D, GARDNER T, MAVROUDIS C, WATSON D. HEMI-FONTAN OPERATION IN SURGERY FOR SINGLE VENTRICLE: A PRELIMINARY REPORT. DISCUSSION. The Annals of thoracic surgery. 1991;51(6):893-900.

33. Bove EL, de Leval MR, Migliavacca F, Guadagni G, Dubini G. Computational fluid dynamics in the evaluation of hemodynamic performance of cavopulmonary connections after the norwood procedure for hypoplastic left heart syndrome. The Journal of Thoracic and Cardiovascular Surgery. 2003;126(4):1040-7. doi:10.1016/s0022-5223(03)00698-6.

34. Troianowski G, Taylor CA, Feinstein JA, Vignon-Clementel IE. Three-dimensional simulations in Glenn patients: clinically based boundary conditions, hemodynamic results and sensitivity to input data. Journal of biomechanical engineering. 2011;133(11):111006.

35. Kung E, Baretta A, Baker C, Arbia G, Biglino G, Corsini C et al. Predictive modeling of the virtual Hemi-Fontan operation for second stage single ventricle palliation: Two patient-specific cases. Journal of Biomechanics. 2013;46(2):423-9. doi:10.1016/j.jbiomech.2012.10.023.

36. Pekkan K, Dasi LP, de Z ├⌐licourt D, Sundareswaran KS, Fogel MA, Kanter KR et al. Hemodynamic performance of stage-2 univentricular reconstruction: Glenn vs. hemi-Fontan templates. Annals of biomedical engineering. 2009;37(1):50-63.

37. Bridges N, Jonas R, Mayer J, Flanagan M, Keane J, Castaneda A. Bidirectional cavopulmonary anastomosis as interim palliation for high-risk Fontan candidates. Early results. Circulation. 1990;82(5 Suppl):IV170.

38. Pridjian AK, Mendelsohn AM, Lupinetti FM, Beekman III RH, Dick II M, Serwer G et al. Usefulness of the bidirectional Glenn procedure as staged reconstruction for the functional single ventricle. The American journal of cardiology. 1993;71(11):959-62.

39. Glenn W, Browne M, Whittemore R. Circulatory bypass of the right side of the heart: cava-pulmonary artery shunt—indications and results (report of a collected series of 537 cases). The Heart and Circulation in the Newborn and Infant Grune & Stratton, New York. 1966.

40. Glenn WW. Circulatory bypass of the right side of the heart: shunt between superior vena cava and distal right pulmonary artery—report of clinical application. New England Journal of Medicine. 1958;259(3):117-20.

41. Glenn WW, Patiño JF. Circulatory by-pass of the right heart. I. Preliminary observations on the direct delivery of vena caval blood into the pulmonary arterial circulation. Azygos vein-pulmonary artery shunt. The Yale journal of biology and medicine. 1954;27(3):147.

42. NULAND SB, Glenn W, Guilfoil P. Circulatory bypass of the right heart. III. Some observations on long-term survivors. Surgery. 1958;43(2):184.

43. Pennati G, Migliavacca F, Dubini G, Pietrabissa R, de Leval MR. A mathematical model of circulation in the presence of the bidirectional cavopulmonary anastomosis in children with a univentricular heart. Medical engineering & physics. 1997;19(3):223-34.

44. Guadagni G, Bove EL, Migliavacca F, Dubini G. Effects of pulmonary afterload on the hemodynamics after the hemi-Fontan procedure. Medical engineering & physics. 2001;23(5):293-8.

45. Griselli M, McGuirk SP, Stümper O, Clarke AJ, Miller P, Dhillon R et al. Influence of surgical strategies on outcome after the Norwood procedure. The Journal of thoracic and cardiovascular surgery. 2006;131(2):418-26.

46. Ho SY, Anderson RH. Coarctation, tubular hypoplasia, and the ductus arteriosus. Histological study of 35 specimens. British heart journal. 1979;41(3):268-74.

47. Chessa M, Dindar A, Vettukattil JJ, Stumper O, Wright JG, Silove ED et al. Balloon angioplasty in infants with aortic obstruction after the modified stage I Norwood procedure. American heart journal. 2000;140(2):227-31.

48. Tianqi H. IN VITRO MULTI-SCALE PATIENT-SPECIFIC MODELING OF HEMODYNAMICS IN STAGE 1 NORWOOD PALLIATION FOR THE TREATMENT OF SINGLE VENTRICLE HEART DISEASE. 2015;0(0):0.

49. Sheikh N, Adhikary DK. Coarctation of Aorta. Chattagram Maa-O-Shishu Hospital Medical College Journal. 2014;13(1):56-9.

50. Machii M, Becker AE. Nature of coarctation in hypoplastic left heart syndrome. The Annals of thoracic surgery. 1995;59(6):1491-4.

51. Schaffler G, Sorantin E, Groell R, Gamillscheg A, Maier E, Schoellnast H et al. Helical CT angiography with maximum intensity projection in the assessment of aortic coarctation after surgery. American Journal of Roentgenology. 2000;175(4):1041-5.

52. Tanous D, Benson LN, Horlick EM. Coarctation of the aorta: evaluation and management. Current opinion in cardiology. 2009;24(6):509-15.

53. Oshinski JN, Parks WJ, Markou CP, Bergman HL, Larson BE, Ku DN et al. Improved measurement of pressure gradients in aortic coarctation by magnetic resonance imaging. Journal of the American College of Cardiology. 1996;28(7):1818-26.

54. De Mey S, Segers P, Coomans I, Verhaaren H, Verdonck P. Limitations of Doppler echocardiography for the post-operative evaluation of aortic coarctation. Journal of biomechanics. 2001;34(7):951-60.

55. Figliola RS, Giardini A, Conover T, Camp TA, Biglino G, Chiulli J et al. In vitro simulation and validation of the circulation with congenital heart defects. Progress in Pediatric Cardiology. 2010;30(1-2):71-80. doi:10.1016/j.ppedcard.2010.09.009.

56. Giardini A, Tacy TA. Pressure recovery explains Doppler overestimation of invasive pressure gradient across segmental vascular stenosis. Echocardiography. 2010;27(1):21-31.

57. Keshavarz-Motamed Z, Garcia J, Maftoon N, Bedard E, Chetaille P, Kadem L. A new approach for the evaluation of the severity of coarctation of the aorta using Doppler velocity index and effective orifice area: in vitro validation and clinical implications. Journal of biomechanics. 2012;45(7):1239-45.

58. Biglino G, Corsini C, Schievano S, Dubini G, Giardini A, Hsia T-Y et al. Computational models of aortic coarctation in hypoplastic left heart syndrome: Considerations on validation of a detailed 3D model. The International journal of artificial organs. 2014;37(5):371-81.

59. Itu L, Sharma P, Ralovich K, Mihalef V, Ionasec R, Everett A et al. Non-invasive hemodynamic assessment of aortic coarctation: validation with in vivo measurements. Annals of biomedical engineering. 2013;41(4):669-81.

60. Helton J, Aglira B, Chin A, Murphy J, Pigott J, Norwood W. Analysis of potential anatomic or physiologic determinants of outcome of palliative surgery for hypoplastic left heart syndrome. Circulation. 1986;74(3 Pt 2):I70-6.

61. Moore J, Spicer R, Mathewson J, Kirby W. High-risk angioplasty. Coarctation of the aorta after Norwood Stage 1. Texas Heart Institute Journal. 1993;20(1):48.

62. Olivieri LJ, de Zélicourt DA, Haggerty CM, Ratnayaka K, Cross RR, Yoganathan AP. Hemodynamic modeling of surgically repaired coarctation of the aorta. Cardiovascular engineering and technology. 2011;2(4):288-95.

63. Menon A, Wendell DC, Wang H, Eddinger TJ, Toth JM, Dholakia RJ et al. A coupled experimental and computational approach to quantify deleterious hemodynamics, vascular alterations, and mechanisms of long-term morbidity in response to aortic coarctation. Journal of pharmacological and toxicological methods. 2012;65(1):18-28.

64. BECKER AE, BECKER MJ, EDWARDS JE. Anomalies associated with coarctation of aorta particular reference to infancy. Circulation. 1970;41(6):1067-75.

65. de Lezo JS, Pan M, Romero M, Medina A, Segura J, Lafuente M et al. Immediate and follow-up findings after stent treatment for severe coarctation of aorta. The American journal of cardiology. 1999;83(3):400-6.

66. Coogan JS, Chan FP, Taylor CA, Feinstein JA. Computational fluid dynamic simulations of aortic coarctation comparing the effects of surgical ‐ and stent ‐ based treatments on aortic compliance and ventricular workload. Catheterization and Cardiovascular Interventions. 2011;77(5):680-91.

67. Biglino G, Giardini A, Baker C, Figliola RS, Hsia TY, Taylor AM et al. In Vitro Study of the Norwood Palliation: A Patient-Specific Mock Circulatory System. ASAIO Journal. 2012;58(1):25.

68. Arzani A, Dyverfeldt P, Ebbers T, Shadden SC. In vivo validation of numerical prediction for turbulence intensity in an aortic coarctation. Annals of biomedical engineering. 2012;40(4):860-70.

69. LaDisa JF, Figueroa CA, Vignon-Clementel IE, Kim HJ, Xiao N, Ellwein LM et al. Computational simulations for aortic coarctation: representative results from a sampling of patients. Journal of biomechanical engineering. 2011;133(9):091008.

70. LaDisa J, John F, Dholakia RJ, Figueroa CA, Vignon ‐ Clementel IE, Chan FP et al. Computational Simulations Demonstrate Altered Wall Shear Stress in Aortic Coarctation Patients Treated by Resection with End ‐ to ‐ end Anastomosis. Congenital heart disease. 2011;6(5):432-43.

71. Snyder M, Rideout VC, Hillestad R. Computer modeling of the human systemic arterial tree. Journal of Biomechanics. 1968;1(4):341-53.

72. Corsini C, Baretta A, Baker C, Hsia T-Y, Schievano S, Taylor A et al. A PATIENT-SPECIFIC MODELING APPROACH FOR PLANNING SINGLE VENTRICLE SURGICAL PROCEDURES. Journal of Biomechanics. 2012(45):S129.

73. Marija Vukicevic TC, Michael Jaeggli,Jian Zhou,, Giancarlo Pennati T-YH, Richard S. Figliola. Control of respiration-driven retrograde flow in the subdiaphragmatic venous return of the Fontan circulation. 2014.

74. Vukicevic M, Chiulli JA, Conover T, Pennati G, Hsia TY, Figliola RS et al. Mock Circulatory System of the Fontan Circulation to Study Respiration Effects on Venous Flow Behavior. ASAIO Journal. 2013;59(3):253-60.

75. Baretta A, Corsini C, Yang W, Vignon-Clementel IE, Marsden AL, Feinstein JA et al. Virtual surgeries in patients with congenital heart disease: a multi-scale modelling test case. Philosophical Transactions of the Royal Society A: Mathematical, Physical and Engineering Sciences. 2011;369(1954):4316-30. doi:10.1098/rsta.2011.0130.

76. Pennati G, Fumero R. Scaling approach to study the changes through the gestation of human fetal cardiac and circulatory behaviors. Annals of biomedical engineering. 2000;28(4):442-52.

77. Snyder M, Rideout V. Computer simulation studies of the venous circulation. Biomedical Engineering, IEEE Transactions on. 1969(4):325-34.

78. Formaggia L, Gerbeau J-F, Nobile F, Quarteroni A. On the coupling of 3D and 1D Navier–Stokes equations for flow problems in compliant vessels. Computer Methods in Applied Mechanics and Engineering. 2001;191(6):561-82.

79. Vignon-Clementel IE, Alberto Figueroa C, Jansen KE, Taylor CA. Outflow boundary conditions for three-dimensional finite element modeling of blood flow and pressure in arteries. Computer Methods in Applied Mechanics and Engineering. 2006;195(29-32):3776-96. doi:10.1016/j.cma.2005.04.014.

80. Westerhof N, Elzinga G, Sipkema P. An artificial arterial system for pumping hearts. Journal of applied physiology. 1971;31(5):776-81.

81. Vukicevic M, Conover TA, Zhou J, Hsia T-Y, Figliola RS, editors. In Vitro Study of Pulmonary Vascular Resistance in Fontan Circulation With Respiration Effects. ASME 2012 Summer Bioengineering Conference; 2012: American Society of Mechanical Engineers.

82. Vukicevic M, Conover T, Jaeggli M, Zhou J, Pennati G, Hsia T-Y et al. Control of respiration-driven retrograde flow in the subdiaphragmatic venous return of the Fontan circulation. ASAIO Journal. 2014;60(4):391-9.

83. Zhou J, Esmaily-Moghadam M, Conover TA, Hsia T-Y, Marsden AL, Figliola RS et al. In Vitro Assessment of the Assisted Bidirectional Glenn Procedure for Stage One Single Ventricle Repair. Cardiovascular Engineering and Technology. 2015:1-12.

84. Esmaily-Moghadam M, Hsia T-Y, Marsden AL. The assisted bidirectional Glenn: A novel surgical approach for first-stage single-ventricle heart palliation. The Journal of Thoracic and Cardiovascular Surgery. 2014.

85. Hlavac M, Holcik J, editors. Windkessel model analysis in Matlab. Proceedings of 10th conference Student Eeict; 2004.

86. Westerhof N, Lankhaar J-W, Westerhof BE. The arterial windkessel. Medical & biological engineering & computing. 2009;47(2):131-41.

87. De Zelicourt D, Pekkan K, Kitajima H, Frakes D, Yoganathan AP. Single-step stereolithography of complex anatomical models for optical flow measurements. Transactions of the ASME-K-Journal of Biomechanical Engineering. 2005;127(1):204-7.

88. Festa P, Ali LA, Bernabei M, De Marchi D. The role of magnetic resonance imaging in the evaluation of the functionally single ventricle before and after conversion to the Fontan circulation. Cardiology in the Young. 2005;15:51.

89. Dillman JR, Dorfman AL, Attili AK, Agarwal PP, Bell A, Mueller GC et al. Cardiovascular magnetic resonance imaging of hypoplastic left heart syndrome in children. Pediatric Radiology. 2010;40(3):261-74. doi:10.1007/s00247-009-1473-5.

90. Schievano S, Migliavacca F, Coats L, Khambadkone S, Carminati M, Wilson N et al. Percutaneous Pulmonary Valve Implantation Based on Rapid Prototyping of Right Ventricular Outflow Tract and Pulmonary Trunk from MR Data1. Radiology. 2007;242(2):490-7.

91. Frommelt MA, Frommelt PC, Berger S, Pelech AN, Lewis DA, Tweddell JS et al. Does an additional source of pulmonary blood flow alter outcome after a bidirectional cavopulmonary shunt? Circulation. 1995;92(9):240-4.

92. McElhinney DB, Marianeschi SM, Reddy VM. Additional pulmonary blood flow with the bidirectional Glenn anastomosis: does it make a difference? The Annals of thoracic surgery. 1998;66(2):668-72.

93. van de Wal HJ, Ouknine R, Tamisier D, Lévy M, Vouhé PR, Leca F. Bi-directional cavopulmonary shunt: is accessory pulsatile flow, good or bad? European journal of cardio-thoracic surgery. 1999;16(2):104-10.

94. Lemler MS, Zellers TM, Harris KA, Ramaciotti C. Coarctation index: identification of recurrent coarctation in infants with hypoplastic left heart syndrome after the Norwood procedure. The American journal of cardiology. 2000;86(6):697-9.

95. Corsini C, Biglino G, Schievano S, Hsia T-Y, Migliavacca F, Pennati G et al. The Effect of Modified Blalock-Taussig Shunt Size and Coarctation Severity on Coronary Perfusion After the Norwood Operation. The Annals of thoracic surgery. 2014;98(2):648-54.

96. Blom J. Monitoring of respiration and circulation. CRC Press; 2003.

97. Neema PK, Sethuraman M, Krishnamanohar S, Rathod RC. Superior vena cava syndrome after pulsatile bidirectional Glenn shunt procedure: Perioperative implications. Annals of cardiac anaesthesia. 2009;12(1):53.

98. Frakes D, Smith M, de Zélicourt D, Pekkan K, Yoganathan A. Three-dimensional velocity field reconstruction. Journal of biomechanical engineering. 2004;126(6):727-35.

99. Kung EO, Taylor CA. Development of a physical Windkessel module to re-create in vivo vascular flow impedance for in vitro experiments. Cardiovascular Engineering and Technology. 2011;2(1):2-14.

100. Chiulli JA. Multi-scale modeling of the Fontan circulation using a mock circulatory system: CLEMSON UNIVERSITY; 2011.

101. Figliola RS, Beasley DE. Theory and design for mechanical measurements. Measurement Science and Technology. 2001;12(10):1743.

102. Kutner MH, Nachtsheim C, Neter J. Applied linear regression models. McGraw-Hill/Irwin; 2004.

103. Altman DG. Practical statistics for medical research. CRC press; 1990.

104. Armitage P, Berry G, Matthews JN. Statistical methods in medical research. John Wiley & Sons; 2008.